

Special Issue
Metrology with Synchrotron Radiation



Metrology with Synchrotron Radiation

Cover picture

(Top) View of the electron storage ring Metrology Light Source (MLS) of PTB in Berlin-Adlershof.
(Bottom) The buildings of BESSY II and the MLS.

Special Journal for the Economy and Science
Official Information Bulletin of the
Physikalisch-Technische Bundesanstalt Braunschweig and Berlin

Special Issue
Volume 124 (2014), No. 3 and 4

Contents

Metrology with Synchrotron Radiation

- *Mathias Richter, Gerhard Ulm: Metrology with Synchrotron Radiation – a Brief Introduction* 3
- *Roman Klein, Reiner Thornagel, Gerhard Ulm: The Electron Storage Rings MLS and BESSY II as Primary Source Standards* 7
- *Roman Klein, Rolf Fliegau, Simone Kroth, Wolfgang Paustian, Mathias Richter, Reiner Thornagel: Source-based Radiometry with Synchrotron Radiation* 16
- *Alexander Gottwald, Udo Kroth, Michael Krumrey, Peter Müller, Frank Scholze: Detector-based Radiometry with Cryogenic Radiometers and Monochromatized Synchrotron Radiation* 21
- *Mathias Richter, Alexander Gottwald, Michael Krumrey: Metrology for X-ray Lasers* 27
- *Alexander Gottwald, Roman Klein, Michael Krumrey, Peter Müller, Wolfgang Paustian, Thomas Reichel, Frank Scholze, Reiner Thornagel: Radiometric Characterization of Space Instrumentation* 30
- *Michael Krumrey, Levent Cibik, Andreas Fischer, Alexander Gottwald, Udo Kroth, Frank Scholze: Reflectometry with Synchrotron Radiation* 35
- *Frank Scholze, Christian Laubis, Annett Barboutis, Christian Buchholz, Andreas Fischer, Jana Puls, Christian Stadelhoff: Radiometry for EUV Lithography* 43
- *Frank Scholze, Anton Haase, Michael Krumrey, Victor Soltwisch, Jan Wernecke: Investigation of Nanostructured Surfaces by Scattering Procedures* 48
- *Michael Krumrey, Raul Garcia-Diez, Christian Gollwitzer, Stefanie Langner: Size Determination of Nanoparticles with Small-angle X-ray Scattering* 53
- *Matthias Müller, Martin Gerlach, Ina Holfelder, Philipp Hönicke, Janin Lubeck, Andreas Nutsch, Beatrix Pollakowski, Cornelia Streeck, Rainer Unterumsberger, Jan Weser, Burkhard Beckhoff: X-ray Spectrometry with Synchrotron Radiation* 57
- *Peter Hermann, Arne Hoehl, Andrea Hornemann, Bernd Kästner, Ralph Müller, Burkhard Beckhoff, Gerhard Ulm: Micro- and Nanospectroscopy and Detector Characterization in the IR and THz Range at the Metrology Light Source* 64
- *Michael Kolbe, Erik Darlatt, Rolf Fliegau, Hendrik Kaser, Alexander Gottwald, Mathias Richter: Surface Characterization with Vacuum UV Radiation* 69

Metrology with Synchrotron Radiation – a Brief Introduction

Mathias Richter*, Gerhard Ulm

When synchrotron radiation began to be utilized for spectroscopic investigations in the 1950s [1], the characteristics of this electromagnetic radiation emitted by relativistic electrons or positrons in circular accelerators had already been thoroughly described in theory within the scope of classical electrodynamics [2]. Thus, from an early stage, the calculability of synchrotron radiation in connection with the spectrum extended far in the direction of short wavelengths was utilized for source-based radiometry and the calibration of energy-dispersive detectors, spectrometers or radiation-sources [1, 3]. Since the 1960s, the American metrology institute NIST (*National Institute of Standards and Technology*, formerly: *National Bureau of Standards*, NBS) has operated the accelerator facility SURF (I, II, III) for radiometry in the spectral ranges of ultraviolet (UV), vacuum UV (VUV) and extreme UV (EUV) radiation [4–6].

A little later, PTB started to carry out the respective work at a 140 MeV synchrotron in Braunschweig [7] as well as at the *Deutsches Elektronen-Synchrotron* DESY in Hamburg [8]. Due to the decision to integrate a planned storage ring project of its own in the Berlin electron storage ring BESSY I, metrology with synchrotron radiation considerably gained in importance and potential at PTB. In March 1979, a respective basic agreement was signed. At BESSY I, PTB operated a radiometry laboratory from the first electron beam storage in December 1981. This lab was continuously enlarged and increasingly utilized until the end of operation of BESSY I in November 1999 [9–11]. Besides source-based radiometry with the storage ring as a primary radiation source standard for calculable synchrotron radiation [12, 13], the detector-based radiometry with electrically calibrated substitution cryogenic radiometers could also be established there as primary detector standards [14, 15] as well as reflectom-

etry as a relative procedure [16, 17]. Also Great Britain [18], Japan [19, 20] and Russia [21–23] used synchrotron radiation from an early stage.

Although radiometry counts among the first applications of synchrotron radiation, the focus was, and still is, however, on materials research, i.e. the investigation of atoms, molecules, surfaces, layer systems and – in general – of hard and soft matter [24–27]. For this purpose, more than 60 accelerators worldwide are available [28], from the more than 50-year-old SURF facility to the modern X-ray lasers FLASH, LCLS, SACLA or FERMI. Today, metrology with synchrotron radiation is mainly dealt with by NIST and PTB, whereby – during the last 30 years – PTB has taken on a leading position. More than 60 PTB staff members currently use the storage ring BESSY II of the *Helmholtz-Zentrum Berlin* (HZB) [29] in Berlin-Adlershof (especially in the EUV and X-ray

* Prof. Dr. Mathias Richter, Department "Radiometry with Synchrotron Radiation", e-mail: mathias.richter@ptb.de

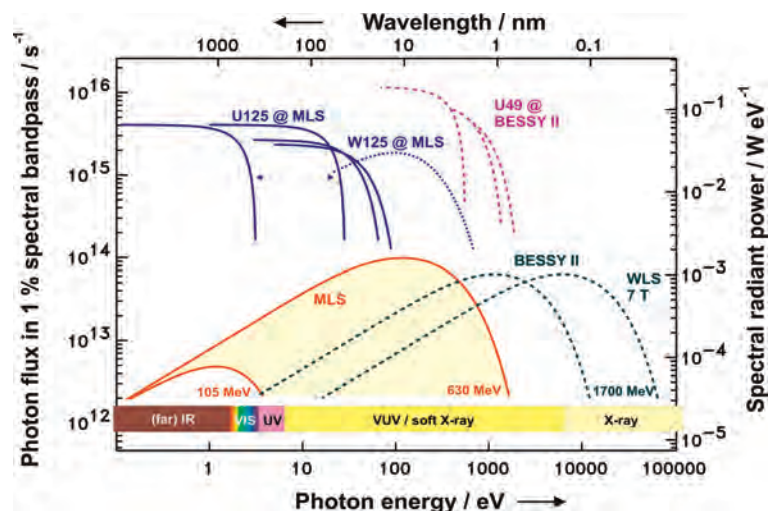


Figure 1: Calculated photon flux or spectral radiant power curves for the Metrology Light Source (MLS) and BESSY II at various energies of the stored electrons. The curves refer both to the bending magnet and to Wiggler (W125) or undulator radiation (U125, U49) in various harmonics.

range) as well as the PTB-owned *Metrology Light Source* (MLS) [30] (which has been developed and is operated by the *Helmholtz-Zentrum Berlin*) for basic radiometry and for metrological applications in research and development [31].

With the change from BESSY I to BESSY II in 1999 and the start of the user operation at the MLS in the year 2008, not only the useable spectral range shown in Figure 1 towards both short and long wavelengths was considerably enlarged but also – based on radiometry – new measurement technology for metrologically well-founded material investigations – such as reference-free X-ray fluorescence analysis – was taken on. This has opened up a broad spectrum of applications for PTB's unique measurement capabilities in the field of metrology with synchrotron radiation, e.g. within the scope of the *European Metrology Research Programme*, EMRP (or EMPIR, respectively).

Figures 2 and 3 as well as Table 1 provide overviews of the laboratories and beamlines used by PTB in Berlin-Adlershof at the MLS and at BESSY II, including the so-called BAMline of the BAM *Federal Institute for Materials Research and Testing* (B5). The calculability of synchrotron radiation requires the precise determination of the storage ring parameters [32] and is used within the scope of source-based radiometry at the white-light beamlines M2a or B3a, as well as at the BAMline B5 for the calibration of energy-dispersive detection systems. At BESSY II, they mainly include energy-dispersive X-ray detectors, e.g. for use in reference-free X-ray spectrometry [33]. At the MLS, e.g. spectrometers and energy-dispersive telescope systems for the extra-terrestrial solar observation are characterized in the spectral range of UV, VUV and EUV radiation [34]. Also at the respective neighboring measuring set-ups M2b and B3b, this refers to spectrometers for UV, VUV and EUV radiation whose calibration will be transferred to secondary radiation source standards, e.g. within the scope of services [35]. The general calibration of radiation detectors, however, is carried

out via detector-based radiometry, with cryogenic radiometers as primary standards. By means of the cryogenic radiometers, the radiant power of monochromatized synchrotron radiation can be measured very precisely [36]. Thereby, the entire spectral range – from the UV up to hard X-rays – can be continuously covered at the monochromator beamlines M3 (*EUV reflectometry*, EUVR) and M4 (*Normal Incidence Monochromator*, NIM) as well as B1, B2a and B5. Optimized for high stability and spectral purity, also reflectometry with very low uncertainties is carried out at the same beamlines as well as at the beamline B2b (*X-ray Pencil Beam Facility*, XPBF) – a relative measurement method which does not require a primary standard [37].

Source- and detector-based radiometry and reflectometry are used – within the scope of services – to calibrate radiation sources and photodetectors and to characterize optical components. However, the measurement capabilities are extensively to work on – partly – very complex measurement tasks within the scope of cooperation projects with external partners from research and industry. Besides the characterization of space instruments [34] or contributions to photon diagnostics of X-ray laser radiation [38], the extensive work on the characterization of optical systems for EUV lithography, which is carried out at the beamlines M3 and B1 especially in cooperation with the *Carl Zeiss SMT GmbH*, is of special importance here [39]. By using scattering methods, also the roughnesses of multilayer mirrors as well as nanostructures, e.g. at EUV lithography masks, can be investigated [40]. Moreover, the beamline B2a (*Four-Crystal Monochromator*, FCM) is used for measurements and experiments on dimensional nanometrology, where the methods of X-ray reflectometry [37] and small-angle X-ray scattering are applied, in addition to layer systems and nanostructured surfaces, to characterize nanoparticles, above all [41]. A large part of this work takes place within the scope of the *European Research Metrology Programme* EMRP (or EMPIR, respectively) as well as the work on X-ray spectrometry [33] which, in turn, concentrates on the beamlines B4b (*Plane-reflection Grating Monochromator*, PGM), B2a and B5 and on the detection of X-ray fluorescence for material analysis. As radiometrically calibrated instrumentation is used for this purpose, the use of reference material can be dispensed with to a large extent, which is of particular importance for the quantification of complex sample systems, e.g. in the fields of microelectronics, photovoltaics or battery research.

Approaches made to quantify material properties on a metrological basis are meanwhile pursued at the MLS also in cooperation with external working groups, especially of the Berlin univer-

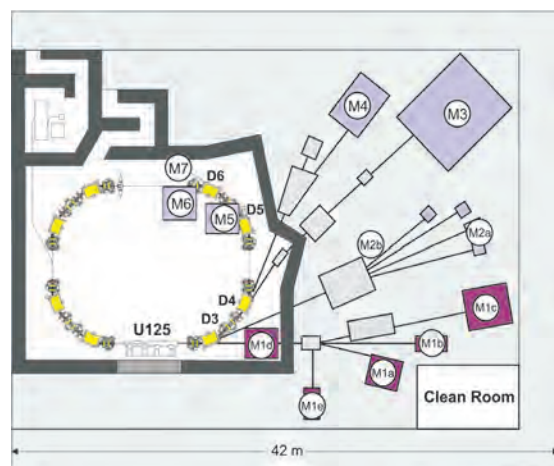


Figure 2: Beamlines and instrumentation at the Metrology Light Source (MLS).

sities. At the beamline M1c (*Insertion Device Beamline, IDB*), the focus is mainly on UV/VUV ellipsometry and electron spectroscopy at surfaces and thin layers [42], and at the IR beamline M6, on micro spectrometry and on scattered-light scanning nearfield optical microscopy (s-SNOM) [43]. MLS has been optimized as the worldwide first storage ring for the generation of particularly intensive coherent synchrotron radiation in the THz range and offers very good possibilities at the dedicated THz beamline M5 for the utilization of radiation in this spectral range [44].

This special edition of *PTB-Mitteilungen* gives a topical survey of the work carried out by PTB

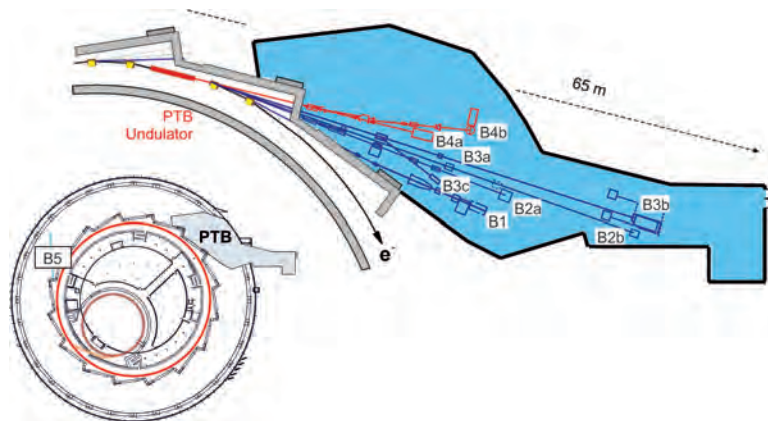


Figure 3: Beamlines and instrumentation in the PTB laboratory at BESSY II.

Table 1: Beamlines and instrumentation at the Metrology Light Source (MLS) and in the PTB laboratory at BESSY II.

Beamline/measuring set-up	Source	Monochromator	Spectral range	Spectral resolving power	Photon flux	Beam size (hor. · vert.)	Divergence (hor. · vert.)	
			Wavelength		/ s ⁻¹	/ mm ²	/ mrad ²	
M1a	VUV irradiation	MLS U125	Reflection filter	≥ 40 nm	Broadband	10 ¹³	3 · 3	≤ 1 · 1
M1b	Direct undulator radiation	MLS U125						
M1c	IDB	MLS U125	NI-GI reflection grating cPGM	4 nm to 400 nm	10 ³	10 ¹²	≤ 2 · 2 (variable)	≤ 0.7 · 1.0
M1d	IR undulator radiation	MLS U125						
M1e	90° undulator radiation	MLS U125		500 nm to 1500 nm	Broadband			
M2a	White-light beamline	MLS Dipole						
M2b	Source calibration	MLS Dipole	Seya/Toroidal grating	7 nm to 400 nm				
M3	EUVR	MLS Dipole	Plane grating	5 nm to 50 nm	10 ³	10 ¹²	≤ 2 · 2 (variable)	≤ 4 · 2 (variable)
M4	NIM	MLS Dipole	Normal incidence	40 nm to 400 nm	10 ²	10 ¹⁰ to 10 ¹²	≤ 3 · 2	≤ 13 · 10
M5	THz	MLS Dipole	FTIR	100 μm to 7 mm	10 ¹ to 10 ³		1 · 1 (focus)	80 · 80 (collimated)
M6	IR	MLS Dipole	FTIR	600 nm to 1000 μm	10 ² to 10 ⁴	up to 10 ¹⁷	1.0 · 0.7 (focus)	50 · 30 (collimated)
			Photon energy					
B1	SX700	B II Dipole	Plane grating	50 eV to 1900 eV	10 ³ to 10 ⁴	10 ¹¹	0.3 · 1.0	2.0 · 0.5
B2a	FCM	B II Dipole	Four crystal	1750 eV to 11 keV	10 ⁴	10 ¹¹	0.5 · 0.2	1.2 · 0.3
B2b	XPBF	B II Dipole	Channel-cut crystal / Multilayer	1.0 keV; 2.8 keV; 7.6 keV	10 ⁴	10 ⁶	0.1 · 0.1	0.005 · 0.005
B3a	White-light beamline	B II Dipole						
B3b	Source calibration	B II Dipole	Normal incidence	3 eV to 30 eV				
B3c	EUV irradiation	B II Dipole	Transmission filter	> 5 nm, broadband		up to 10 ¹⁷	≥ 1 · 1 (variable)	80 · 20
B4a	Direct undulator radiation	B II U49						
B4b	PGM	B II U49	Plane grating	40 eV to 1860 eV	10 ³ to 10 ⁴	10 ⁸ to 10 ¹³	0.14 · (0.015 to 1)	0.6 · 0.4
B5	BAMline	B II WLS	Double crystal / Double multilayer	8 keV to 60 keV	10 ³	10 ⁷	1 · 1	0.03 · 0.03

in Berlin-Adlershof at the electron storage rings MLS and BESSY II. A comparison with the last complete overview [31] has shown that metrology with synchrotron radiation is still a very dynamic field of work at PTB, with an increasing depth of application and ever increasing importance.

References

- [1] D. H. Tomboulion, P. L. Hartman: *Phys. Rev.* **102**, 1423 (1956)
- [2] J. Schwinger: *Phys. Rev.* **75**, 1912 (1949)
- [3] D. Lemke, D. Labs: *Appl. Opt.* **6**, 1043 (1967)
- [4] K. Codling, R. P. Madden: *J. Appl. Phys.* **36**, 380 (1965)
- [5] K. Codling: *Nucl. Instr. and Meth. A* **347**, 1 (1994)
- [6] U. Arp, C. W. Clark, A. P. Farrell, E. Fein, M. L. Furst, E. W. Hagley: *Rev. Sci. Instrum.* **73**, 1674 (2002)
- [7] H. Kaase: *Optik* **46**, 149 (1976)
- [8] D. Einfeld, D. Stuck, B. Wende: *Metrologia* **14**, 111 (1978)
- [9] M. Kühne, F. Riehle, E. Tegeler, B. Wende: *Nucl. Instrum. Methods* **208**, 399 (1983)
- [10] G. Ulm, B. Wende: *Rev. Sci. Instrum.* **66**, 2244 (1995)
- [11] M. Richter, G. Ulm: *J. Electron Spectr. Relat. Phenomena* **101–103**, 1013 (1999)
- [12] F. Riehle, B. Wende: *Opt. Lett.* **10**, 365 (1985)
- [13] F. Riehle, B. Wende: *Metrologia* **22**, 75 (1986)
- [14] A. Lau-Främbis, U. Kroth, H. Rabus, E. Tegeler, G. Ulm, B. Wende: *Metrologia* **32**, 571 (1995)
- [15] H. Rabus, V. Persch, G. Ulm: *Appl. Opt.* **36**, 5421 (1997)
- [16] M. Krumrey, M. Kühne, P. Müller, F. Scholze: *Proc. SPIE* **1547**, 136 (1991)
- [17] D. Fuchs, M. Krumrey, P. Müller, F. Scholze, G. Ulm: *Rev. Sci. Instrum.* **66**, 2248 (1995)
- [18] P. J. Key, T. H. Ward: *Metrologia* **14**, 17 (1978)
- [19] H. Suzuki: *Nucl. Instr. and Meth.* **228**, 201 (1984)
- [20] T. Zama, I. Saito: *Metrologia* **40**, 115 (2003)
- [21] E. S. Gluskin, E. M. Trakhenberg, I. G. Feldman, V. A. Kochubei: *Space Sci. Instrum.* **5**, 129 (1980)
- [22] A. N. Subbotin, V. V. Gaganov, A. V. Kalutsky, V. F. Pindyurin, V. P. Nazmov, A. D. Nikolenko, A. K. Krasnov: *Metrologia* **37**, 497 (2000)
- [23] A. N. Subbotin *et al.*: *Nucl. Instr. and Meth. A* **470**, 452 (2001)
- [24] P. J. Duke: *Synchrotron Radiation: Production and Properties*, Oxford University Press, Oxford (2000)
- [25] H. Wiedemann: *Synchrotron Radiation*, Springer, Berlin (2002)
- [26] A. Hofmann: *The Physics of Synchrotron Radiation*, Cambridge University Press, Cambridge (2004)
- [27] T. Möller, J. Falta (Eds.): *Forschung mit Synchrotronstrahlung*, Vieweg+Teubner, Wiesbaden (2010)
- [28] <http://www.lightsources.org/> (retrieved: 2016-05-13)
- [29] <http://www.helmholtz-berlin.de/> (retrieved: 2016-05-13)
- [30] A. Gottwald, R. Klein, R. Müller, M. Richter, F. Scholze, R. Thornagel, G. Ulm: *Metrologia* **49**, 146 (2012)
- [31] B. Beckhoff, A. Gottwald, R. Klein, M. Krumrey, R. Müller, M. Richter, F. Scholze, R. Thornagel, G. Ulm: *Phys. Status Solidi B* **246**, 1415 (2009)
- [32] R. Klein, R. Thornagel, G. Ulm: in this publication on p. 7
- [33] M. Müller *et al.*: in this publication on p. 57
- [34] A. Gottwald, R. Klein, M. Krumrey, P. Müller, W. Paustian, T. Reichel, F. Scholze, R. Thornagel: in this publication on p. 30
- [35] R. Klein, R. Fliegau, S. Kroth, W. Paustian, M. Richter, R. Thornagel: in this publication on p. 16
- [36] A. Gottwald, U. Kroth, M. Krumrey, P. Müller, F. Scholze: in this publication on p. 21
- [37] M. Krumrey, L. Cibik, A. Fischer, A. Gottwald, U. Kroth, F. Scholze: in this publication on p. 35
- [38] M. Richter, A. Gottwald, M. Krumrey: in this publication on p. 27
- [39] F. Scholze, C. Laubis, A. Barboutis, C. Buchholz, A. Fischer, J. Puls, C. Stadelhoff: in this publication on p. 43
- [40] F. Scholze, A. Haase, M. Krumrey, V. Soltwisch, J. Wernecke: in this publication on p. 48
- [41] M. Krumrey, R. Garcia-Diez, C. Gollwitzer, S. Langner: in this publication on p. 53
- [42] M. Kolbe, E. Darlatt, H. Kaser, A. Gottwald, M. Richter: in this publication on p. 69
- [43] P. Hermann, A. Hoehl, A. Hornemann, B. Kästner, R. Müller, B. Beckhoff, G. Ulm: in this publication on p. 64
- [44] J. Feikes, M. von Hartrott, M. Ries, P. Schmid, G. Wüstefeld, A. Hoehl, R. Klein, R. Müller, G. Ulm: *Phys. Rev. ST Accel. Beams* **14**, 030705 (2011)

The Electron Storage Rings MLS and BESSY II as Primary Source Standards

Roman Klein*, Reiner Thornagel, Gerhard Ulm

Introduction

The spectral and spatial properties of the synchrotron radiation generated at electron storage rings are determined by just a few parameters and can be calculated by classical electrodynamics. In this way, electron storage rings become primary source standards [1].

Whereas the radiometric application of the black-body radiators, which can be calculated by means of Planck's radiation law, is limited to the infrared (IR), the visible, and the near-ultraviolet (UV) light, the radiation generated at electron storage rings can be applied from the THz, via the visible spectral range, to the X-ray range and – thus – opens up a spectral range for radiometric applications which is extended by several decades. PTB has been using the electron storage ring BESSY II as a primary source standard since January 1999, especially in the spectral range from the vacuum ultraviolet (VUV) to the X-ray range [2]. Furthermore – from 1984 until its shutdown in November 1999 – PTB had the electron storage ring BESSY I at its disposal as a primary source standard in the UV and the VUV spectral ranges [3, 4]. With the *Metrology Light Source* (MLS) [5, 6], PTB has, since 2008, been using a primary source standard again which is optimized for this particular spectral range.

Apart from the large spectral range, electron storage rings have another advantage: the intensity of the radiated power can be varied over many orders of magnitude via the selected number of stored electrons and can thus be adapted to the measurement requirements without changing the form of the spectrum [7]. This option of varying the electron current can be used at the MLS and at BESSY II over approx. 12 decades, however, only in special shifts which are reserved for the special operation of the respective storage ring. Furthermore, by adjusting the electron energy, the spectral

shape of the synchrotron radiation emitted can be varied. This option can be used especially at the MLS.

Calculable synchrotron radiation

The radiation of relativistic electrons can be calculated by means of classical electrodynamics [1]. For the case of constant radial acceleration of relativistic electrons – as is given on the orbit in the homogeneous magnetic field of a bending magnet in an electron storage ring and is shown as an example in Figure 1 – the functional relation is described by the so-called "Schwinger theory" [8]. The spectral radiant intensity I_{0E} as a function of the photon energy E is calculated from the

* Dr. Roman Klein,
Working Group
"Synchrotron
Radiation Sources",
e-mail: roman.
klein@ptb.de

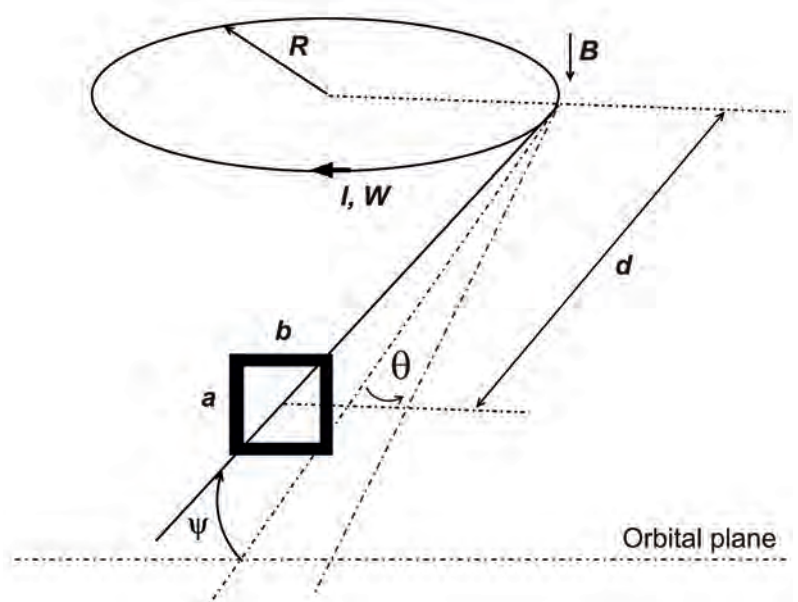


Figure 1: Schematic representation of the parameters and of the geometry to calculate the spectral radiant power of synchrotron radiation.

magnetic induction B , the electron energy W and the electron current I by

$$I_{0E}^{\sigma} = \frac{d}{dE} \frac{d^2}{d\theta d\psi} \phi^{\sigma} = \frac{2eIR^2}{3\epsilon_0\gamma^4} \frac{E^2}{(hc)^3} \left(\left[1 + (\gamma\psi)^2 \right]^2 K_{2/3}^2(\xi) \right) \quad (1)$$

for the fraction with a polarization direction (electric field vector) parallel (σ -component) to the storage ring plane and

$$I_{0E}^{\pi} = \frac{d}{dE} \frac{d^2}{d\theta d\psi} \phi^{\pi} = \frac{2eIR^2}{3\epsilon_0\gamma^4} \frac{E^2}{(hc)^3} \left(\left[1 + (\gamma\psi)^2 \right] (\gamma\psi)^2 K_{1/3}^2(\xi) \right) \quad (2)$$

for the fraction with a component which is vertical to it and whose phase is shifted by 90° (π -component) with

$$\xi = \frac{2\pi RE}{3hc\gamma^3} \left(1 + (\gamma\psi)^2 \right)^{3/2} = \frac{1}{2} \frac{E}{E_c} \left(1 + (\gamma\psi)^2 \right)^{3/2}$$

$$R = \frac{W}{ecB}; \quad \gamma = \frac{W}{m_0c^2} \quad .$$

Hereby, R is the radius of curvature of the electron orbit, and $K_{1/3}$ and $K_{2/3}$ are modified Bessel functions of the second kind which can be calculated numerically [9]. The angular distribution of the synchrotron radiation is homogeneous in the horizontal direction, i.e. in the orbital plane of the electrons, but is narrow in the vertical direction, where the divergence depends on the photon

energy. The σ -component reaches its maximum in the orbital plane, the π -component disappears in the orbital plane.

The spectrum of the synchrotron radiation extends continuously from the far infrared into the X-ray range and is classified by the so-called "characteristic energy" E_c :

$$E_c = \frac{3hc\gamma^3}{4\pi R} \quad . \quad (3)$$

In practical units, E_c can be expressed by:

$$E_c/eV = 665.0 B/T (W/GeV)^2 = 2218 (W/GeV)^3 / (R/m) \quad .$$

Eq. (1) and (2) reflect the ideal case of electrons which move exactly on the orbit. In reality, however, the electrons have a Gaussian spatial distribution around the ideal orbit, with the standard deviations σ_x and σ_y for the horizontal and the vertical directions, and an angular distribution with the standard deviations σ_x' and σ_y' . The distribution in horizontal direction, i.e. in the orbital plane, is of no significance due to the tangential observation. The vertical distributions are summarized as follows to an effective vertical angular divergence $\Sigma_{y'}$ for an observation point located at a distance d :

$$\Sigma_{y'} = \left(\sigma_y'^2 / d^2 + \sigma_y'^2 \right)^{1/2} \quad . \quad (4)$$

The quantity which is of interest for applications – the spectral radiant power Φ_E through an aperture of, e.g., the size $a \cdot b$ at a distance d from the source point of the radiation, can then be calculated as follows:

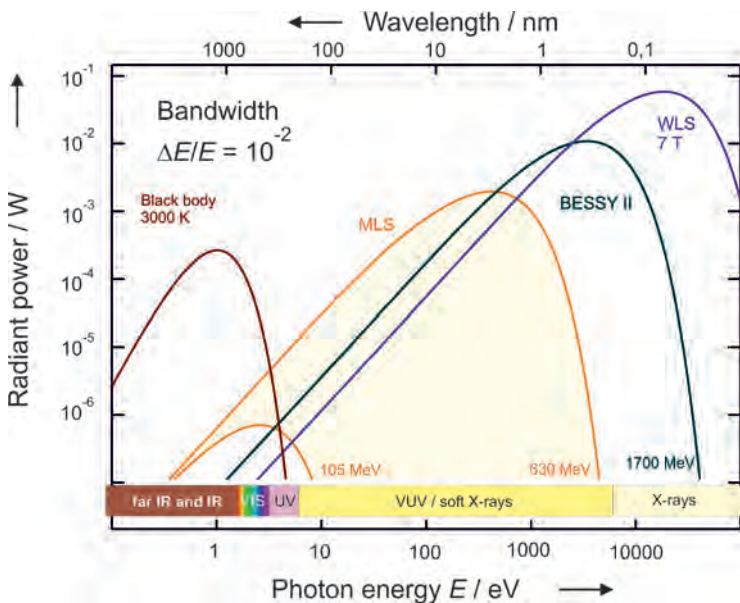
$$\Phi_E = \Phi_E(E; W, B, I, \Sigma_{y'}, \psi, d, a, b)$$

$$= \frac{d\Phi}{dE}(E) = \iint_{\text{aperture}} \left[\int_{-\infty}^{+\infty} \frac{1}{\sqrt{2\pi}\Sigma_{y'}} \left[I_{0E}^{\pi}(\psi'') + I_{0E}^{\sigma}(\psi'') \right] e^{-\frac{(\psi''-\psi')^2}{2\Sigma_{y'}^2}} d\psi'' \right] d\psi' d\theta \quad . \quad (5)$$

The expressions from (1) and (2) are hence convoluted with the effective vertical beam divergence and integrated over the angular range accepted by an aperture. For a rectangular aperture as shown in Figure 1, the integration via the horizontal angle θ contributes only with a factor b/d , and in the vertical direction, the integration extends via ψ' from $(\psi-a/2d)$ to $(\psi+a/2d)$, whereby ψ is the angle of the center of the aperture ($a/d, b/d, \psi \ll 1$). The calculation is carried out numerically. Figure 2 and Figure 3 show the radiant power for different electron energies at the MLS and at BESSY II.

Schwinger's equation describes the special case of a relativistic electron on a circular orbit, i.e. in a homogeneous magnetic field. This condition is fulfilled for the bending magnets in an electron

Figure 2: Calculated radiant power for some of the radiation sources utilized by PTB in comparison to a black-body radiator.



storage ring, which exhibit very good field homogeneity across the range of the radiation's source point. In addition, the radiation of an electron moving on any given trajectory can just as well be calculated by means of the formalism of classical electrodynamics. This allows the radiation of electrons to be calculated which move in magnets with strong field gradients – as is, for example, the case with *wavelength shifters* (WLS) which are operated in storage rings [10]. These WLS have a higher magnetic induction in the radiation's source point than a bending magnet and emit, according to Eq. (3), synchrotron radiation of a higher characteristic energy which can also be used for radiometric purposes. The radiation of electrons in a periodically alternating magnetic field as is given in undulators can be calculated in the same way and can be used for radiometry [11].

All quantities that enter into Eq. (5) must be known, i.e. they usually have to be measured. The relative uncertainty in the respective measured value of the quantity determines the relative uncertainty of the calculation of the spectral radiance according to Eq. (5). This will be described in more detail in the next section.

BESSY II and MLS as primary source standards

In order to be able to operate and utilize an electron storage ring as a primary source standard, the equipment of the storage ring with instruments and the storage ring operating schedule must be optimized as follows:

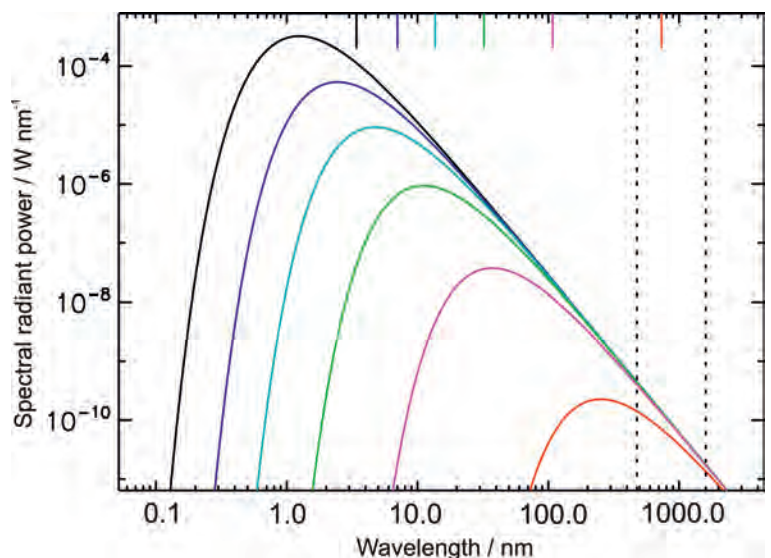
- The storage ring must permit stable and reproducible operation.
- Measuring devices must be installed which allow the parameters entering into eq. (5) to be determined with a sufficiently small relative uncertainty.
- The vacuum system of the storage ring (especially the vacuum chambers of the bending magnets) must be designed in such a way that the direct use of the synchrotron radiation is possible without diffraction losses, in the spectral range being of interest.
- As the spectral radiant intensity emitted by an electron storage ring under normal operating conditions is often too high for radiometric applications, and as the spatial conditions do not permit a very large distance of the calibration facility from the storage ring, the operating schedule must make it possible for the storage ring to be operated in a special operation mode, especially in the case of reduced electron beam currents. For other calibration tasks it is necessary to operate the electron storage ring at reduced electron energy in order to suppress higher monochromator diffraction orders or scattered light.

These conditions are given at BESSY II and at the MLS [1]. In the following, the measurement of the storage ring parameters and of the necessary geometrical quantities will be described in detail. For this purpose, examples from the MLS will, as far as possible, be used, which are also described in detail in [5]. Examples from BESSY II can be found in [12].

Measurement of the electron energy W

At BESSY II, the electron energy can be measured by means of two independent and complementary procedures. These procedures are resonant spin depolarization [13] and the Compton backscatter of laser photons [14, 15]. For the procedure of resonant spin depolarization, a spin-polarized electron beam is required. At BESSY II, this spin polarization builds up after approximately one hour in normal operation at an electron energy of 1.7 GeV. It can be destroyed by irradiation of radio frequency of a certain frequency. From this frequency value, the electron energy can then be calculated very precisely – in our case with a relative uncertainty of better than $5 \cdot 10^{-5}$. The spin polarization can be observed by measuring the loss rate of the stored electrons via detection of the related radiation background or via a modification of the lifetime of the electron beam current as the intrabeam scattering rate of the stored electrons exhibits a spin-dependent term. For a spin-polarized electron beam, the scattering cross section is smaller than for an unpolarized electron beam. The higher the intrabeam scattering rate of the electrons, the higher the loss rate of the stored electrons. This procedure of resonant spin depolarization is established [16]. It can, however, only be applied if the time until reaching polarization – which depends on the electron energy with the inverse of the fifth power – is in the range

Figure 3: Calculated spectral radiant power for some electron energies of the MLS. (The calculation was carried out for the following parameters: $I = 10$ mA, various electron energies: $W = 628$ MeV, 495 MeV, 397 MeV, 299 MeV, 199 MeV and 105 MeV, from left to right, through an aperture diaphragm having a radius of $r = 2.5$ mm, at a distance of $d = 14.8$ m).



of several hours, i.e. at comparably high electron energies, as is the case at BESSY II. Therefore, the procedure of energy measurement by Compton backscattering of laser photons was established especially for the MLS [15]. For this purpose, the beam of a CO₂ laser is superimposed antiparallel to the electron beam. The laser photons scattered at the electrons in the direction of the electron beam, which now exhibit a photon energy which has been shifted by approximately $4\gamma^2$ into the very hard X-ray range, are detected with an energy-dispersive detector. From the maximum energy of the scattered photons, the electron energy can then be calculated (see Figures 4 a, b). The relative

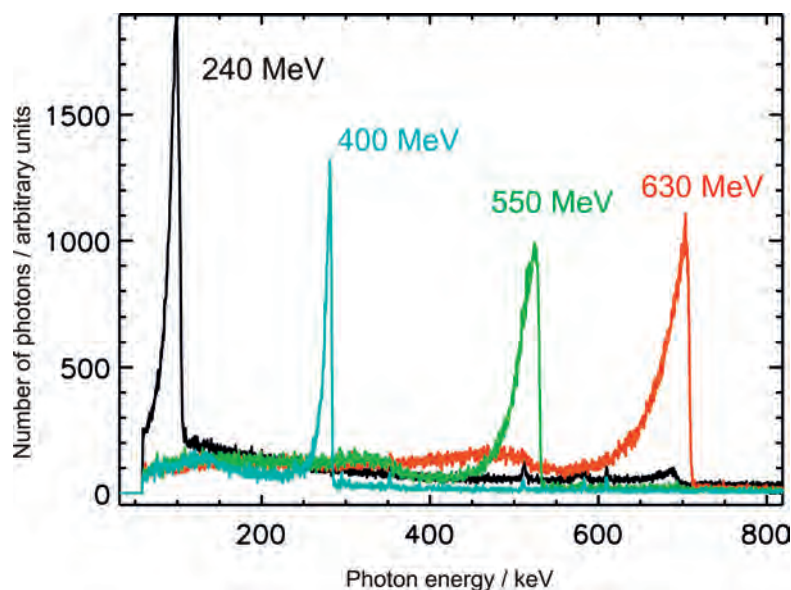


Figure 4 a:
Spectra of backscattered CO₂ laser photons for various electron energies.

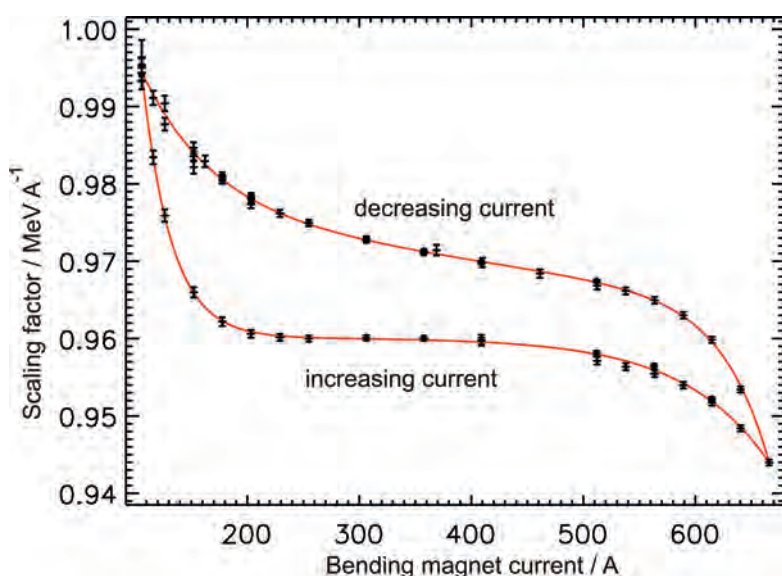


Figure 4 b:
Scaling factors between the current feed of the bending magnets and the electron energy gained by measuring the backscattered laser photons. The hysteresis of the magnets is clearly to be seen.

uncertainty in the determination of the electron energy amounts, with this procedure, to less than 10^{-4} . Both procedures for the determination of the electron energy were applied simultaneously – at BESSY II and at an electron energy of 1700 MeV – and showed very good agreement [15].

Measurement of the magnetic induction B at the source point

One of the bending magnets at the MLS and one of the bending magnets at BESSY II are used as sources of calculable radiation. The magnetic field of these magnets was thoroughly measured prior to the installation in order to make sure that negligibly small magnetic field gradients occur in the region of the source point. The vacuum chambers of these bending magnets are specially designed in such a way that an NMR probe can be brought to the source point of the radiation in a non-magnetic tube which can be inserted by means of a feedthrough in order to measure the magnetic induction B at the source point without a stored electron beam. The relative uncertainty for this is better than 10^{-4} .

Measurement of the electron current I

In normal user operation, the stored electron current is typically in the range of some 100 mA. PTB operates the MLS and BESSY II in special calibration shifts – in the ultimate case with only one stored electron. This corresponds to an electron beam of 1 pA at the MLS, and of 0.2 pA at BESSY II. For that reason, the instrumentation must be available to be able to adjust and measure the electron current over a range of more than 12 decades in a controllable manner. In the range of currents above 2 mA, this is done, at both storage rings, with two *Parametric Current Transformers* (PCTs) each [5].

In the range of the smallest electron currents, i.e. for currents smaller than approx. 1 nA (at the MLS) and several 100 pA (at BESSY II), the electron current is determined by counting the stored electrons and multiplying the result by the rotational frequency of the electrons [5]. For this purpose, the electrons are, after the calibration measurement has been finished, thrown out of the storage ring in a controlled way by approaching a mechanical scraper to the electron beam. At the same time, the stepwise decrease in the intensity of the radiation is observed by means of photodiodes which have been cooled down to LN₂ temperature and are irradiated by the emitted synchrotron radiation (see Figure 5). In the current range lying in between, i.e. from approximately 1 nA to 2 mA, the electron current is also determined by measuring the intensity of the emitted synchrotron radiation by means of photodiodes with a linear

response behavior. Three pairs of photodiodes (one pair without filter, two pairs with filters for attenuation) are used to cover the current range described. The calibration factors which attribute an electron current to the photocurrent are then determined by comparison in the overlapping boundary area by means of the other procedures mentioned above.

Determination of the effective angular divergence Σ_Y

The effective divergence of the electron beam is usually small in comparison to the vertical angular aperture of the synchrotron radiation. Therefore, the convolution of the vertical distribution of the photons with the effective divergence only brings about a small modification in the calculated spectral radiant power behind an aperture, which can be expressed by the quantity ε :

$$\Phi_E = \Phi_E(E; W, B, I, \Sigma_Y, \psi, d, a, b) = \Phi_E^{Schwinger}(E; W, B, I, \psi, d, a, b) \cdot (1 + \varepsilon(E; W, B, \Sigma_Y, \psi, d, a)) \tag{6}$$

whereby $\Phi_E^{Schwinger}$ is the spectral radiant power without taking the effective beam divergence into account. The quantity ε is small for typical calibration geometries and photon energies, as can be seen in Figure 6 with the example of the MLS. At BESSY II, which possesses an even smaller emittance in comparison to the MLS, the value of ε is mostly below 10^{-4} [12]. Usually, it is sufficient to calculate the value of Σ_Y from the machine parameters. These calculations are typically affected by a relative uncertainty of 20 %. Due to this, the influence in the calculation of the spectral radiant power is, however, still lower than several 10^{-4} .

Figure 7 shows measurements as examples carried out with regard to the vertical angle distribution by means of calibrated filter radiometers. For applications where the influence of the effective angle distribution has a greater influence, the effective angle distribution can also be measured by means of suitable instruments, e.g. by means of a Bragg polarimeter [17].

Measurement of the distance d from the source point and of other geometrical quantities

The source point of the synchrotron radiation is located in the vacuum chamber of the bending magnet and, thus, in the ultra-high vacuum. To measure the distance d of the source point from a flux-limiting aperture (Figure 1), an optical projection procedure is used. At a distance d_1 from the source point, a slit aperture, with slits of a well-known distance, can be inserted into the beam

path. The shadow cast by this slit aperture onto a projection plane which is located at a distance d_2 from the slit aperture which has been determined very precisely by means of a laser distance meter, allows the exact determination of the distance of the projected slits and – via the intercept theorem, thus the determination of the sought total distance $d = d_1 + d_2$. By means of this method, an uncertainty of typically 2 mm is obtained.

Usually, measurements are carried out in the orbital plane, so that the vertical emission angle accounts for $\psi = 0^\circ$. This is achieved by adjustment to the symmetry of the detector signal around the

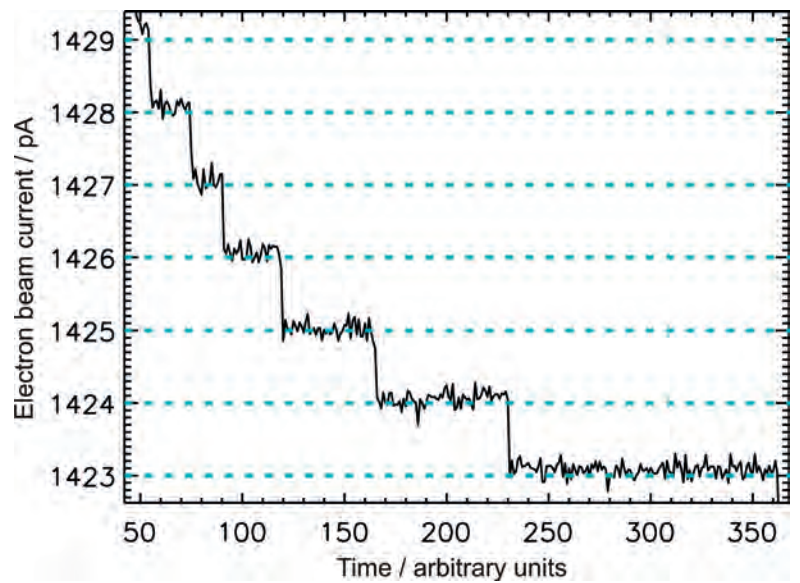


Figure 5a: Measurement of the electron current by means of an unfiltered photodiode. Each step represents the loss of an electron.

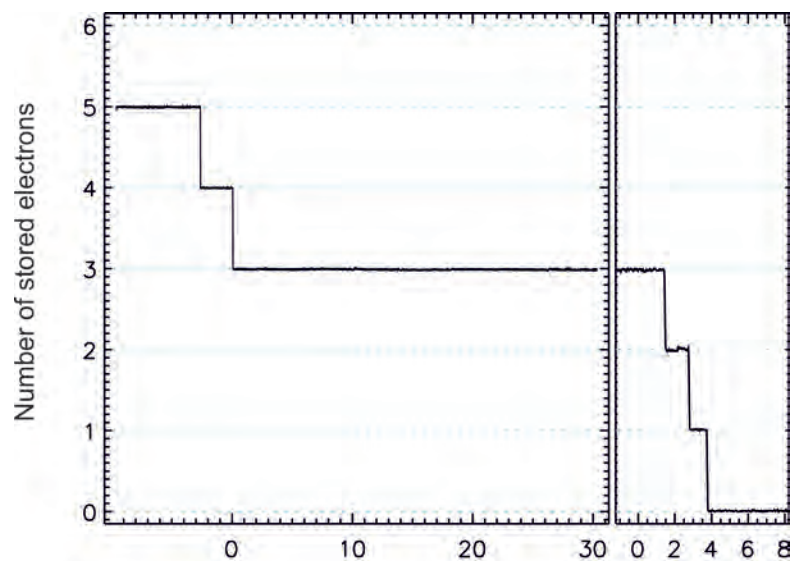


Figure 5b: Few stored electrons with a long lifetime in the MLS (left). After the measurement, the remaining electrons are removed from the storage ring in a controllable way by means of a scraper and thereby counted.

extrema of the vertical distribution, as shown, for example, in Figure 7. A typical adjustment error lies in the range of some μrad .

The quantity $a \cdot b$ of a flux-limiting aperture diaphragm is determined geometrically, e.g. by means of a measuring microscope. As the aperture diaphragm is usually a detector property, the uncertainty in its determination is not attributed to the primary source standard, but to the detector.

Uncertainties and comparison with other standards

In Table 1, the uncertainties in the determination of the input parameters of the Schwinger formula

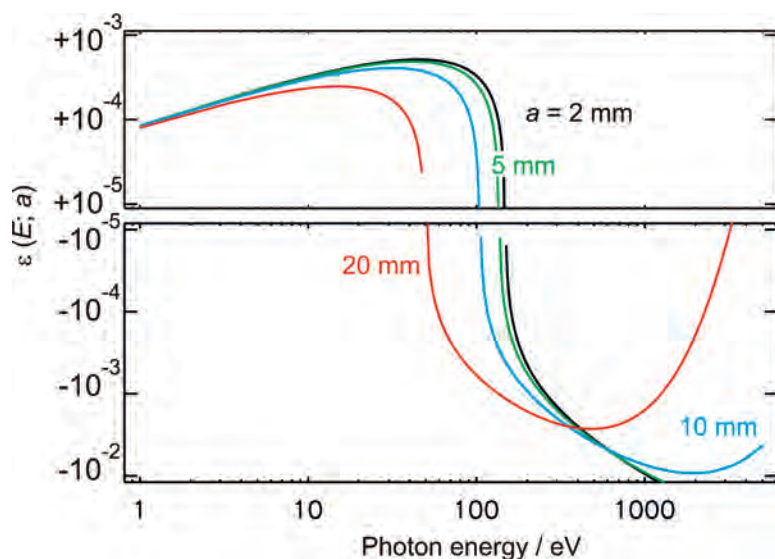


Figure 6: Influence of the quantity ε on the spectral radiant power at the MLS through an aperture at a distance $d = 15$ m for various vertical aperture diaphragms a ($W = 600$ MeV; $B = 1.3$ T; $\Sigma_v' = 50$ μrad , $\psi = 0$ mrad).

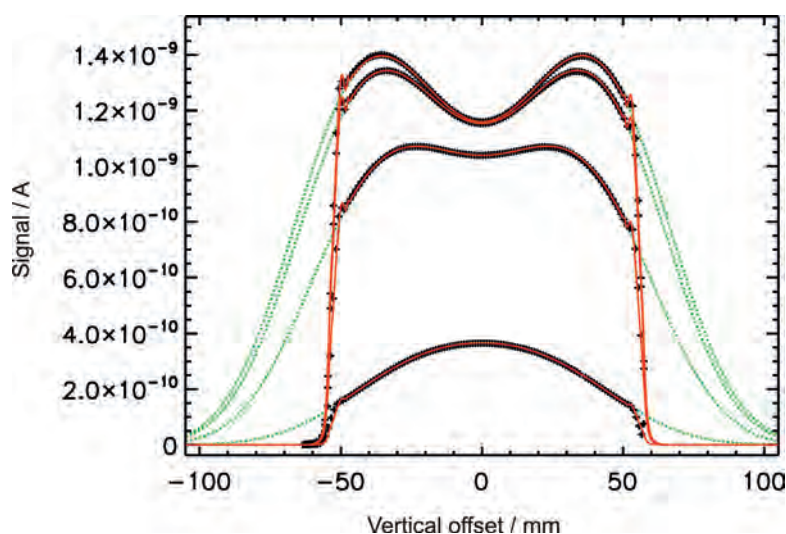


Figure 7: Calculated (red) and measured vertical distribution (+) of the synchrotron radiation at 476 nm for various electron energies of the MLS (from above: 628 MeV, 397 MeV, 199 MeV, 105 MeV).

are summarized for the MLS and for BESSY II. The respective influence of the uncertainty of these parameters on the overall uncertainty of the calculation of the spectral radiant power depends on the photon energy and was calculated by the numerical partial derivative [5]. Up to photon energies of approximately the characteristic energy, the relative uncertainty remains almost constant at small values and is dominated by the distance measurement and by the current measurement. For higher photon energies, it then increases strongly and is mainly dominated by the uncertainty in the determination of the magnetic induction in the source point and of the electron energy. The smallest relative uncertainties can thus be realized for photon energies below the characteristic energy, so that it may be of advantage for measurements at high photon energies to use a source with a higher characteristic energy – such as, e.g., a superconducting wavelength shifter [10]. If you compare, however, the uncertainty in the calculation at certain photon energies with the radiant power available at these photon energies, especially compared to the overall radiated power, it becomes clear that, in the case of certain calibration procedures, limitations arise in the utilizable spectral range. This applies, e.g., in the case of the source-based calibration of radiation sources [18, 33], i.e. in the direct comparison of the radiation properties of an unknown source with those of the primary source standard by means of wavelength-dispersive monochromator detector systems. Here, higher diffraction orders of the monochromator cause high uncertainties in the calibration if the measurements are carried out at low photon energies and – thus – low available radiant power, in comparison with the higher energetic fraction of the spectrum. Here, an operation – e.g. of the MLS – at reduced electron energy then becomes necessary.

Since using synchrotron radiation for radiometric purposes began, the spectral radiant intensity of electron storage rings which are operated as primary source standards has been compared with other established source standards or detector standards. These comparisons serve to verify the realized radiometric scales and to validate the uncertainty budget.

For example, the primary standards “electron storage ring” and “black-body radiator” were compared by several working groups by means of transfer radiators (tungsten filament lamps) or filter radiometers in the range of the spectral overlap between synchrotron radiation and black-body radiation, i.e. in the spectral range of the IR and of the VIS [3, 19, 20, 21]. The primary source standard BESSY I was compared to a cryogenic radiometer as the primary detector standard, both spectrally, by means of filter radiometers [21, 22, 23], and

MLS		$\Delta\Phi(E) / \Phi(E) \cdot 10^{-3} (k=1)$ at $E =$		
Parameters	Value	1 eV	100 eV	1000 eV
Electron energy W	600.00(6) MeV	0.07	0.12	0.67
Magnetic induction B	1.30000(13) T	0.07	0.04	0.27
Electron current I	100.00(2) mA	0.20	0.20	0.20
Eff. vert. divergence Σ_Y	44(9) μ rad	0.04	0.18	1.5
Vert. emission angle ψ	0(5) μ rad	0.0007	0.003	0.03
Distance d	15000(2) mm	0.27	0.26	0.17
Total		0.35	0.40	1.7
BESSY II		$\Delta\Phi(E) / \Phi(E) \cdot 10^{-3} (k=1)$ at $E =$		
Parameters	Value	1 eV	100 eV	1000 eV
Electron energy W	1718.60(6) MeV	0.1	0.3	1.4
Magnetic induction B	1.29932(12) T	0.06	0.3	1.8
Electron current I	10.000(2) mA	0.2	0.2	0.2
Eff. vert. divergence Σ_Y	3.5(7) μ rad	0.06	0.2	0.4
Vert. emission angle ψ	0(2) μ rad	0.04	0.2	0.3
Distance d	30 000(2) mm	0.1	0.1	0.1
Total		0.3	0.6	2.3

Tab. 1: Sample parameter set for the calculation of the spectral radiant power of the MLS and of BESSY II according to Schwinger, including uncertainties in the determination of the parameters.

by measuring the emitted overall radiant power by means of the detector standard [24]. The two primary standards BESSY I and BESSY II were compared in the range of the UV and VUV by means of deuterium lamps as transfer radiators [25], and in the X-ray range by means of a Si(Li) detector as a transfer detector [26]. Furthermore, the primary source standard BESSY I was compared with radioactive standards [27] in the X-ray range at 6.4 keV and 8.0 keV by means of a Si(Li) detector. By means of deuterium lamps as transfer standards, a comparison between BESSY II and the SURF-III electron storage ring of NIST took place [28]. At the MLS, a comparison at different electron energies was carried out with filter radiometers which were calibrated traceably to a cryogenic radiometer as the primary detector standard (Figures 7, 8) [29]. Furthermore, the emitted overall radiant power was measured by means of a cryogenic radiometer at the MLS for a large set of parameters with various electron energies and electron beam currents (Figure 9) [30].

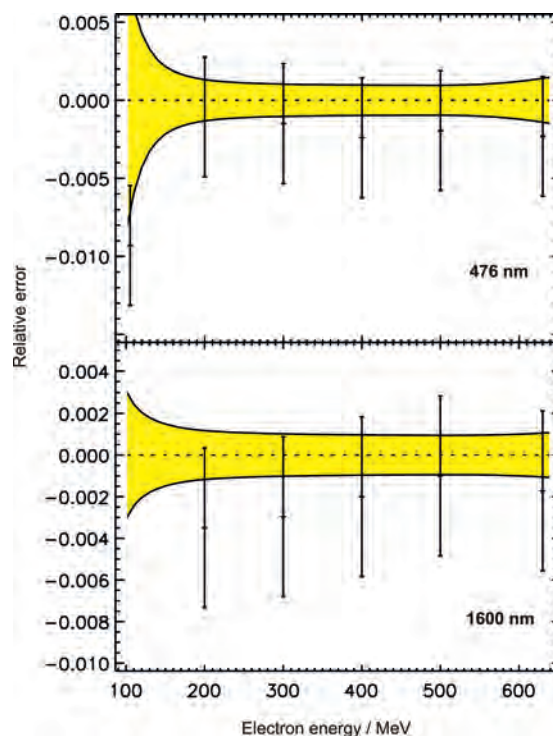


Figure 8: Comparison of the calculated radiant intensity of the MLS with the radiant intensity measured by means of calibrated filter radiometers at 476 nm and 1600 nm for various electron energies.

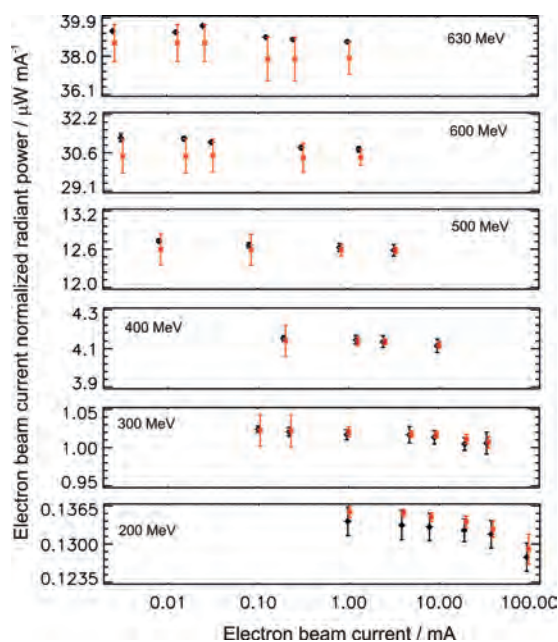


Figure 9: Comparison of the radiant power calculated from the storage ring parameters (red) with the radiant power measured by means of a cryogenic radiometer (black) for various electron energies and electron currents of the MLS.

For all these comparisons in the IR, VIS, UV, VUV, EUV and X-ray ranges, a good agreement became evident whose uncertainty was not determined by the realization of the unit by means of the source standard, but by the comparison procedure or by the transfer standards used.

Summary and applications

The electron storage rings MLS and BESSY II are established as national primary source standards in the spectral range of the visible up to the X-ray ranges. The relative uncertainty of the realization of the spectral radiant power amounts, in the major part of the covered spectral range, to less than 0.1 %. The undispersed radiation can be used for the direct calibration of energy-dispersive detectors such as *high-purity germanium* (HPGe), Si(Li) or SSD detectors, or for the calibration of wavelength-dispersive spectrographs – as is envisaged, for example, for the calibration of the SPICE spectrograph [31] of the Solar Orbiter Mission [32]. Furthermore, radiation sources can be traceably calibrated to the respective primary source standard [33] by means of a wavelength-dispersive transfer system. At the MLS, a new measuring set-up has been put into operation for this purpose which covers the spectral range from 7 nm to 400 nm [34, 35].

The high dynamics in the radiant intensity, and the possibility of exact determination, also allow the building of a radiation-metrological bridge from conventional radiometry to single-photon radiometry. In this connection, a single-photon detector was, for example, traceably calibrated to a cryogenic radiometer at the MLS [36].

References

- [1] J. Hollandt, J. Seidel, R. Klein, G. Ulm, A. Migdall, M. Ware: in *Optical Radiometry*, A. C. Parr, R. U. Datla, J. L. Gardner (Eds.), 213–290, Elsevier, Amsterdam (2005)
- [2] R. Thornagel, R. Klein, G. Ulm: *Metrologia* **38**, 385 (2001)
- [3] F. Riehle, B. Wende: *Opt. Lett.* **10**, 365 (1985)
- [4] F. Riehle, B. Wende: *Metrologia* **22**, 75 (1986)
- [5] R. Klein et al.: *Phys. Rev. ST Accel. Beams* **11**, 110701 (2008)
- [6] R. Klein, G. Brandt, R. Fliegau, A. Hoehl, R. Müller, R. Thornagel, G. Ulm: *Metrologia* **46**, S266 (2009)
- [7] R. Klein, R. Thornagel, G. Ulm: *Metrologia* **47**, R33 (2010)
- [8] J. Schwinger: *Phys. Rev.* **75**, 1912 (1949)
- [9] V. O. Kostroun: *Nucl. Instr. and Meth.* **172**, 371 (1980)
- [10] R. Klein, G. Brandt, L. Cibik, M. Gerlach, M. Krumrey, P. Müller, G. Ulm, M. Scheer: *Nucl. Instr. and Meth.* **580**, 1536 (2007)
- [11] K. Molter, G. Ulm: *Rev. Sci. Instrum.* **63**, 1296 (1992)
- [12] R. Klein, R. Thornagel, G. Ulm: *PTB-Mitteilungen* **115**, No. 3, 8 (2005)
- [13] P. Kuske, R. Goergen, R. Klein, R. Thornagel, G. Ulm: *Proc. EPAC 2000*, 1771 (2000)
- [14] R. Klein, T. Mayer, P. Kuske, R. Thornagel, G. Ulm: *Nucl. Instr. and Meth. A* **384**, 293 (1997)
- [15] R. Klein, P. Kuske, R. Thornagel, G. Brandt, R. Görgen, G. Ulm: *Nucl. Instr. and Meth. A* **486**, 541 (2002)
- [16] A. Lysenko, I. Koop, A. Polunin, E. Pozdeev, V. Ptitsin, Yu. Shatunov: *Nucl. Instr. and Meth. A* **359**, 419 (1995)
- [17] R. Klein, G. Brandt, R. Thornagel, J. Feikes, M. Ries, G. Wüstefeld: *Proc. IPAC 2011*, 1165 (2011)
- [18] M. Richter, J. Hollandt, U. Kroth, W. Paustian, H. Rabus, R. Thornagel, G. Ulm: *Metrologia* **40**, S107 (2003)
- [19] A. R. Schaefer, R. D. Saunders, L. R. Hughey: *Opt. Eng.* **25**, 892 (1986)
- [20] H. J. Kostkowski, J. L. Lean, R. D. Saunders, L. R. Hughey: *Appl. Opt.* **25**, 3297 (1986)
- [21] M. Stock, J. Fischer, R. Friedrich, H. J. Jung, R. Thornagel, G. Ulm, B. Wende: *Metrologia* **30**, 439 (1993)
- [22] N. P. Fox, P. J. Key, F. Riehle, B. Wende: *Appl. Opt.* **25**, 2409 (1986)
- [23] R. Thornagel, J. Fischer, R. Friedrich, M. Stock, G. Ulm, B. Wende: *Metrologia* **32**, 459 (1995/96)
- [24] H. Rabus, R. Klein, F. Scholze, R. Thornagel, G. Ulm: *Metrologia* **39**, 381 (2002)
- [25] M. Richter, J. Hollandt, U. Kroth, W. Paustian, H. Rabus, R. Thornagel, G. Ulm: *Metrologia* **40**, 107 (2003)

- [26] *F. Scholze, R. Thornagel, G. Ulm: Metrologia* **38**, 391 (2001)
- [27] *D. Arnold, G. Ulm: Nucl. Instr. and Meth. A* **339**, 43 (1994)
- [28] *U. Arp, R. Klein, Z. Li, W. Paustian, M. Richter, P.-S. Shaw, R. Thornagel: Metrologia* **48**, 261 (2011)
- [29] *R. Klein, D. Taubert, R. Thornagel, J. Hollandt, G. Ulm: Metrologia* **46**, 359 (2009)
- [30] *R. Klein, A. Gottwald, G. Brandt, R. Fliegauf, A. Hoehl, U. Kroth, H. Kaser, M. Richter, R. Thornagel, G. Ulm: Metrologia* **48**, 219 (2011)
- [31] *A. Fludra et al.: Proc. SPIE* **8862**, 88620F (2013)
- [32] *A. Gottwald, R. Klein, M. Krumrey, P. Müller, W. Paustian, T. Reichel, F. Scholze, R. Thornagel: in this publication on p. 30*
- [33] *R. Klein, R. Fliegauf, S. Kroth, W. Paustian, M. Richter, R. Thornagel; in this publication on p. 16*
- [34] *R. Thornagel, R. Klein, S. Kroth, W. Paustian, M. Richter: Metrologia* **51**, 528 (2014)
- [35] *R. Thornagel, R. Fliegauf, R. Klein, S. Kroth, W. Paustian, M. Richter: Rev. Sci. Instr.* **86**, 013106 (2015)
- [36] *I. Müller, R. M. Klein, J. Hollandt, G. Ulm, L. Werner: Metrologia* **49**, S152 (2012)

Source-based Radiometry with Synchrotron Radiation

Roman Klein*, Rolf Fliegau, Simone Kroth, Wolfgang Paustian, Mathias Richter, Reiner Thornagel

* Dr. Roman Klein,
Working Group
"Synchrotron
Radiation Sources", e-mail:
roman.m.klein@ptb.de

Introduction

Source-based radiometry relates to the metrological concept by which radiometric quantities are traced back to standardized light sources or radiation sources. As early as in the initial phase of the *Physikalisch-Technische Reichsanstalt* (Imperial Physical Technical Institute – PTR) at the end of the 19th century, work had been focused on the development of reliable light-source standards. In 1900, the derivation of the radiation law for temperature radiators by Max Planck led – with the black-body cavity radiator – to the realization of the first primary source standard at PTR.

Even at high temperatures of up to 3000 K, black-body radiation covers, however, only the optical range, i.e. the range of infrared (IR), of visible (VIS) and of ultraviolet (UV) radiation. In the adjacent vacuum UV (VUV) and in the X-ray region, PTB has therefore – since 1982 – used the radiation of electron storage rings [1–3] for

source-based radiometry, whose spectral radiance can be calculated within the scope of classical electrodynamics with the so-called Schwinger equation [4]. Currently, PTB uses the electron storage rings BESSY II and MLS as calculable, primary, national standards. At both storage rings, set-ups are operated which allow radiation sources to be traceably calibrated against the respective national standard in the units "spectral radiance" and "spectral radiant intensity".

Calibration of radiation sources

One main field of work of source-based radiometry in the PTB laboratories at BESSY II and at the MLS is the calibration of other radiation sources. This is done by comparison with the respective primary standard. As the spectral distribution of the sources to be compared is not monochromatic, wavelength-dispersive transfer systems must be used as radiation comparators.

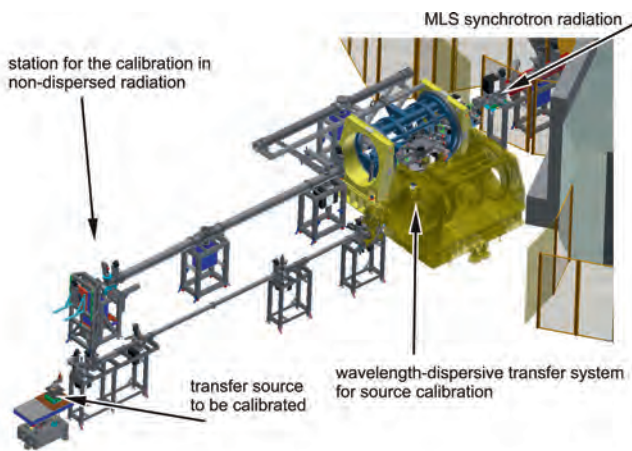


Figure 1.

Set-up for source calibration at the MLS. Schematic drawing on the left: The set-up can be directed either to the MLS or to the source to be calibrated. On the right: Photo with the set-up, directed to the source to be calibrated (deuterium lamp) which is visible at the bottom left of the picture.

As an example, Figure 1 shows the set-up for source calibration in the PTB laboratory at the MLS, which can be used in the wavelength range $400 \text{ nm} > \lambda > 7 \text{ nm}$ [5-7]. Six gratings (three in normal incidence (NI) geometry and three in grazing incidence (GI) geometry) are available to cover this large spectral range. Different optical configurations for spectral sub-ranges (i.e. different materials for the coating of mirrors and gratings) as well as different optical filters ensure the maximum possible spectral purity for monochromatization. This set-up can be displaced on air cushions in such a way that it can face either the calculable radiation of the MLS or the radiation of a radiation source to be calibrated. In both set-up positions, the radiation source is located at the same distance of approx. 10 m.

When the transfer system is calibrated with synchrotron radiation (SR), the source point (extension approx. 1 mm) is demagnified and imaged by means of an ellipsoidal pre-mirror at a ratio of 10:1 into the plane of the entrance aperture of the monochromator. An aperture in front of the pre-mirror defines the acceptable solid angle $\Delta\Omega_{\text{SR}}$, so that the sensitivity of the transfer system $s(\lambda)$ results as follows from the signal current $i_{\text{SR}}(\lambda)$ of the detector and the spectral radiance $I_{\lambda}^{\text{SR}}(\lambda)$ of the synchrotron radiation which can be calculated with the aid of the Schwinger equation:

$$s(\lambda) = \frac{i_{\text{SR}}(\lambda)}{I_{\lambda}^{\text{SR}}(\lambda) \Delta\Omega_{\text{SR}}} . \quad (1)$$

The intensity of the synchrotron radiation is, thereby, adapted to the level of the radiation sources to be calibrated via the stored electron beam current in special operation of the storage ring. For the correction of polarization effects, the measurements are, in addition, performed in two orientations (orthogonal to each other) of the plane of the transfer system to the plane of the storage ring. After that, the sensitivity of the transfer system, which has been determined in this way with calculable synchrotron radiation in a fixed optical configuration, is stable over months and can be used for the calibration of transfer source standards.

By using an entrance aperture which is so large that it completely encompasses the image of the transfer source (TS) to be calibrated, calibrations with regard to the spectral radiant intensity $I_{\lambda}^{\text{TS}}(\lambda)$ can be performed via:

$$I_{\lambda}^{\text{TS}}(\lambda) = \frac{i_{\text{TS}}(\lambda)}{s(\lambda) \Delta\Omega_{\text{TS}}} . \quad (2)$$

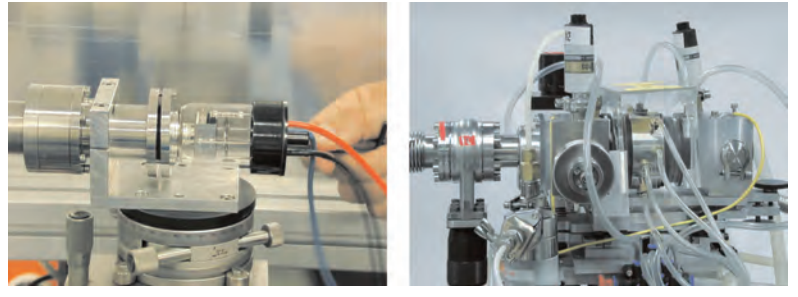


Figure 2: Deuterium lamp (left) and hollow cathode discharge source (right) as transfer radiator standards for UV and VUV radiation.

As the transfer source and the SR source are located at the same distance at the MLS transfer system, $\Delta\Omega_{\text{TS}} = \Delta\Omega_{\text{SR}}$ is valid. Thereby, both the storage ring and the transfer source are assumed to be point sources. This is justified in view of the measurement geometries used. Under the same assumption, also the amount of the spectral irradiance – which is important for many technical applications – can be calculated from the measured spectral radiant intensity at a defined distance r from the source point:

$$E_{\lambda}^{\text{TS}}(\lambda) = \frac{I_{\lambda}^{\text{TS}}(\lambda)}{r^2} . \quad (3)$$

If, in contrast, only a partial range of the source spot, with the area ΔA , is observed due to the selection of a small monochromator entrance aperture, calibrations of the spectral radiance, averaged over this partial range, can be realized (a quantity of rather fundamental and source-specific importance):

$$L_{\lambda}^{\text{TS}}(\lambda) = \frac{i_{\text{TS}}(\lambda)}{s(\lambda) \Delta\Omega_{\text{TS}} \Delta A} . \quad (4)$$

For the spectral range of UV radiation and the directly adjacent VUV range, deuterium lamps have established themselves as suitable transfer source standards in industry and research (Figure 2). With radiation exit windows made of quartz or MgF_2 , these encapsulated gas discharge lamps emit radiation with wavelengths down to approx. 160 nm or 120 nm. Figure 3 shows the measured spectral radiant intensity of a deuterium lamp compared to the calculated spectral radiant intensity of the MLS. As a matter of routine, these lamps are currently still calibrated within the scope of services on the set-up at BESSY II [5, 8] which covers the spectral range from 40 nm to 400 nm. Table 1 summarizes the corresponding uncertainty budget.

The fact that the spectral distribution of synchrotron radiation and deuterium lamps is, in the UV, similar with respect to the increase towards

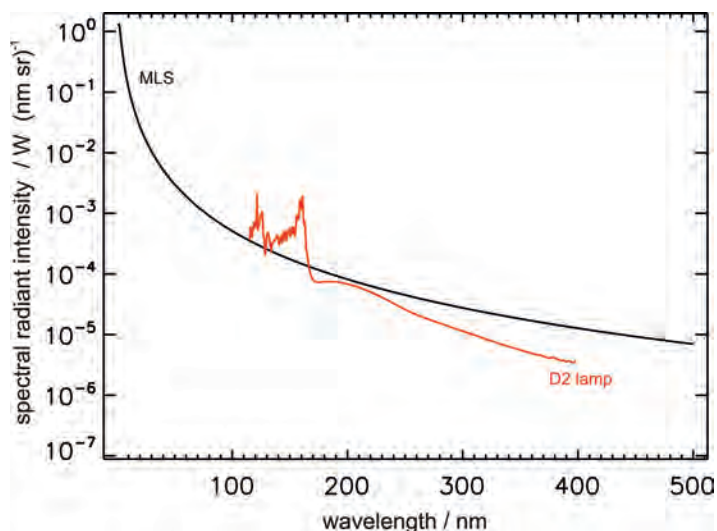


Figure 3: Radiant intensity of the MLS (black) and of a deuterium lamp (red). The MLS was operated at an electron beam current of 15 μ A to provide a radiant intensity similar to that of the deuterium lamp.

short wavelengths facilitates the calibration, because problems caused by a non-linear behavior during beam detection are minimized. This is not the case if deuterium lamps are calibrated against calculable black-body radiation whose radiant power strongly decreases in the UV towards smaller wavelengths.

As demonstrated in Figure 4, the different source-based UV scales within PTB agree very well. The internal comparisons which have been performed at PTB for this purpose in the past few years [9] not only relate to different primary standards (BESSY I, BESSY II, black-body radiator), but also to different transfer standards (deuterium lamps, tungsten strip lamps) and even to different radiometric measurands (radiant intensity, radiance, irradiance). A bilateral comparison with NIST, where the electron storage ring SURF III is used as the primary source standard, showed good agreement of the scales [10]. Figure 5 shows the comparison of a deuterium lamp calibration at the

Table 1: Uncertainty budgets for the calibration of deuterium lamps in the PTB laboratory at BESSY II.

Wavelength range	Spectral bandwidth	Relative standard measurement uncertainty ($k = 1$)	
		Spectral radiance	Spectral radiant intensity
115.0 nm to 120.4 nm	0.8 nm	5 %	5 %
120.5 nm to 122.5 nm	0.8 nm	18 %	18 %
122.6 nm to 165 nm	0.8 nm	5 %	5 %
165 nm to 175 nm	1.6 nm	3.5 %	3.5 %
176 nm to 400 nm	1.6 nm	2.5 %	2 %

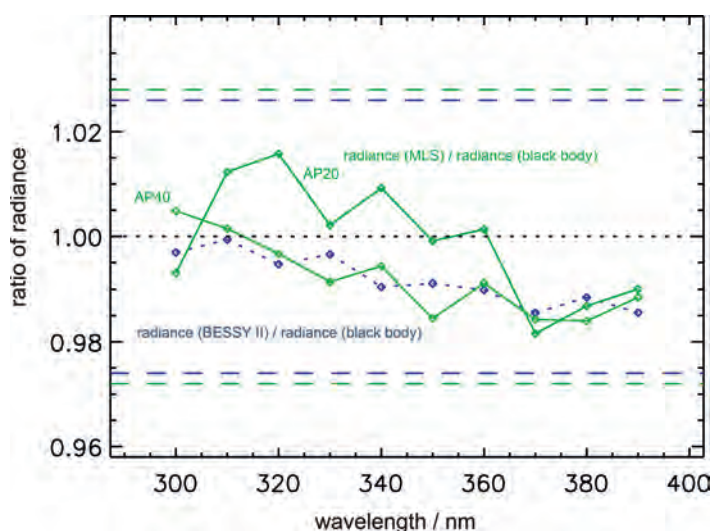


Figure 4: Radiance comparison of a tungsten strip lamp. Plotted are the calibration results obtained at the electron storage rings BESSY II and MLS, in relation to that of a black-body radiator. The horizontal lines illustrate the combined relative standard measurement uncertainty of the respective comparison. At the MLS, the radiance was measured with two different entrance apertures (AP20 and AP40).

set-up B3b at BESSY II and the new set-up M2b at the MLS [5, 6]. With the strongly extended spectral range of this new set-up and traceability to the MLS as the national standard, the high competence of PTB in the field of the calibration of radiation sources in the UV and VUV is further expanded. The high flexibility in the selection of the operation parameters of the MLS allows measurement conditions optimized for the respective calibration task. The free selection of the electron energy at the MLS between 105 MeV and 630 MeV allows the synchrotron radiation spectrum to be adapted to the respective measurement task so that radiation sources can – also below 40 nm – be calibrated free from fractions of higher monochromator orders and stray light.

For the spectral range with wavelengths shorter than those covered by deuterium lamps, mainly transfer sources, which are based on noble gas emission lines of an open hollow cathode discharge source (Figure 2) and which are used, in particular, within the scope of scientific cooperation projects for the calibration of solar telescopes [11–16], are

available. In addition, also novel types of sources are calibrated. Figure 6 shows, for example, the radiant intensity of a gas jet source which has been measured within the scope of a scientific cooperation project with the *Deutsches Zentrum für Luft- und Raumfahrt* (DLR, German Aerospace Center) [17]. In the case of this source, a jet of noble gas is excited by electron impact. It is used in a VUV solar simulator which allows the Earth-based testing of space instruments.

Calibration with direct, non-dispersed radiation

Wavelength-dispersive spectrometers – but also energy-dispersive X-ray detectors such as, e.g., lithium-drifted semiconductor detectors (Si(Li) detectors) or *high-purity germanium* (HPGe) detectors – allow synchrotron radiation to be detected in a spectrally resolved way. This is why they can be calibrated in the direct beam of calculable synchrotron radiation, in analogy to the source calibration set-ups described above. The relative uncertainty in the calculation of the spectral radiant intensity lies, thereby, in the range of a few 10^{-3} or below [1].

By using BESSY II and MLS as calculable sources over a broad spectral range, PTB has – with its measurement capabilities in the field of the calibration of wavelength-dispersive systems or energy-dispersive X-ray detectors – a worldwide leading position and provides calibrations of the highest precision to international customers [18].

Figure 7 shows the characterization of a *silicon drift detector* (SDD) at the MLS which has been

operated at different electron beam currents. In addition to the determination of the detection sensitivity, important properties such as, for example, the pile-up behavior, can be investigated here by variation of the incident photon flux. Examples of the calibration of further X-ray detectors at BESSY II are given in [19].

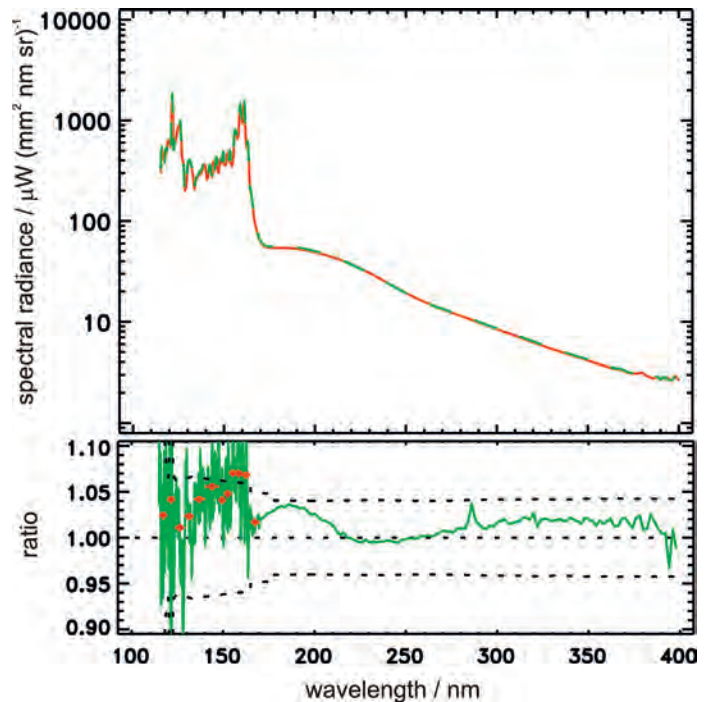


Figure 5: Spectral radiance of a deuterium lamp, measured at the source calibration set-up at BESSY II (red) and at the MLS (green). Bottom: Ratio of the two calibration data sets. The dotted line illustrates the combined relative standard measurement uncertainty. The red points are values which have been averaged over line groups.

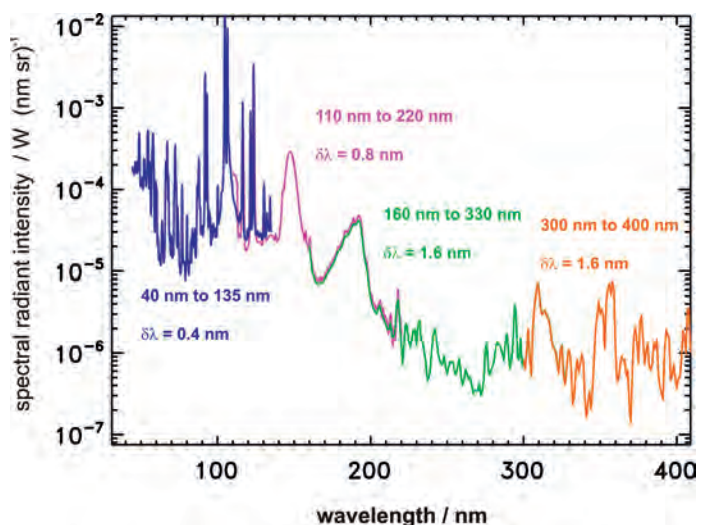
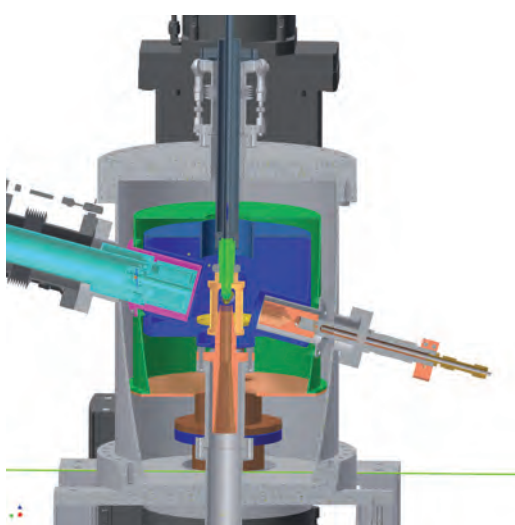


Figure 6: On the left: Gas-jet VUV-source in which a noble gas jet (from top to bottom) is excited by electron impact (from left to right). On the right: Radiant intensity of the gas-jet VUV-source, measured at the source calibration set-up at BESSY II. The different colors illustrate the different configurations of the set-up for the respective wavelength range and the spectral resolution ($\delta\lambda$) [17].

In the spectral range of higher photon energies, measurements can, in addition, be performed at the wavelength shifter (WLS) of the BAMline B5 [5, 20] which is used jointly with the *Bundesanstalt für Materialforschung und -prüfung* (BAM, Federal Institute for Materials Research and Testing). Here, the spectrum is clearly harder and one obtains correspondingly higher count rates at high photon energy. The energy-dispersive detectors calibrated in this way are used, for example, in the reference-free X-ray fluorescence analysis [21].

Due to the commissioning of a large vacuum tank, also large spectrographs can be characterized directly at the MLS with calculable synchrotron radiation. This is, for example, done within the scope of cooperation projects for space missions (as described in [16]). As described above, flexibility in the selection of the electron energy is very important for the suppression or estimation of the influence of higher diffraction orders. In addition, the great dynamics in the variation of the radiant intensity allows the linearity of the detection systems to be investigated. Spectrographs for solar missions often measure emission lines of highly charged ions which have very different intensities. The intensity behavior, in turn, allows conclusions on solar-physical properties to be drawn. The SPICE spectrograph of the Solar Orbiter Mission will be calibrated in this way with the direct, calculable radiation of the MLS [22].

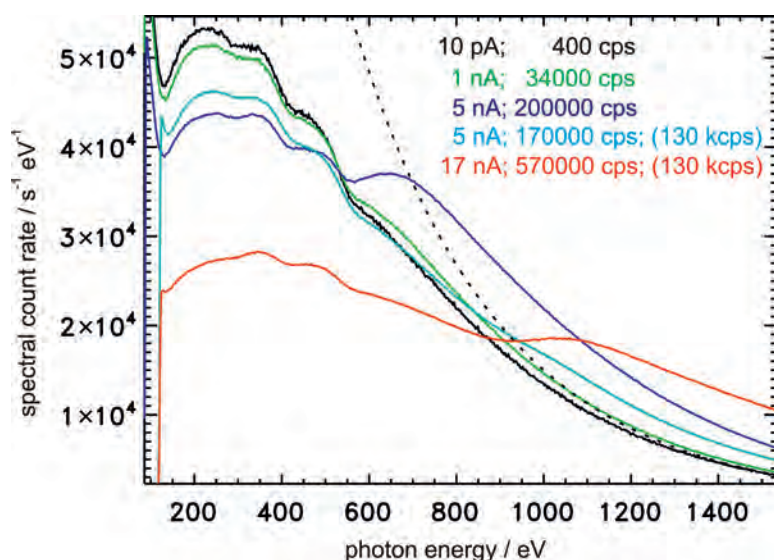


Figure 7:

Characterization of a silicon drift detector at the MLS: The dotted line shows the calculated, incident photon flux of the primary source MLS, the colored curves show the spectra measured at different incident photon rates which can be varied by means of the stored electron current as indicated within the figure. All spectra have been scaled relating to the electron current of $1\mu\text{A}$. The light-blue curve and the red curve have been measured with a modified adjustment of the detector electronics (130 kcps) which has been optimized for high count rates. Saturation and pile-up effects are visible by the relative signal decrease at high photon rates at lower photon energies and the relative signal increase at low photon rates at higher photon energies, respectively.

References

- [1] R. Klein, R. Thornagel, G. Ulm: in this publication on p. 7
- [2] R. Thornagel, R. Klein, G. Ulm: *Metrologia* **38**, 385 (2001)
- [3] R. Klein *et al.*: *Phys. Rev. ST Accel. Beams* **11**, 110701 (2008)
- [4] J. Schwinger: *Phys. Rev.* **75**, 1912 (1949)
- [5] M. Richter, G. Ulm: in this publication on p. 3
- [6] R. Thornagel, R. Klein, S. Kroth, W. Paustian, M. Richter: *Metrologia* **51**, 528 (2014)
- [7] R. Thornagel, R. Fliegau, R. Klein, S. Kroth, W. Paustian, M. Richter: *Rev. Sci. Instr.* **86**, 013106 (2015)
- [8] M. Richter, J. Hollandt, U. Kroth, W. Paustian, H. Rabus, R. Thornagel, G. Ulm: *Nucl. Instr. and Meth.* **467–468**, 605 (2001)
- [9] M. Richter, J. Hollandt, U. Kroth, W. Paustian, H. Rabus, R. Thornagel, G. Ulm: *Metrologia* **40**, 107 (2003)
- [10] U. Arp *et al.*: *Metrologia* **48**, 261 (2011)
- [11] K. Danzmann, M. Günther, J. Fischer, M. Kock, M. Kühne: *Appl. Opt.* **27**, 4947 (1988)
- [12] J. Hollandt, M. C. E. Huber, M. Kühne: *Metrologia* **30**, 381 (1993)
- [13] J. Hollandt, M. Kühne, B. Wende: *Appl. Opt.* **33**, 68 (1994)
- [14] M. Richter, A. Gottwald, F. Scholze, R. Thornagel, G. Ulm: *Advances in Space Research* **37**, 265 (2006)
- [15] M. Richter, A. Gottwald, M. Krumrey, W. Paustian, F. Scholze, R. Thornagel, G. Ulm: *PTB-Mitteilungen* **115**, 218 (2005)
- [16] A. Gottwald, R. Klein, M. Krumrey, P. Müller, W. Paustian, T. Reichel, F. Scholze, R. Thornagel: in this publication on p. 30
- [17] M. Sznajder, T. Renger, A. Witzke, U. Geppert, R. Thornagel: *Advances in Space Research* **52**, 1993 (2013)
- [18] M. Krumrey, F. Scholze, G. Ulm: *Proc. SPIE* **5501**, 277 (2004)
- [19] W. Paustian, M. Richter, F. Scholze, R. Thornagel, G. Ulm: *PTB-Mitteilungen* **115**, 181 (2005)
- [20] R. Klein, G. Brandt, L. Cibik, M. Gerlach, M. Krumrey, P. Müller, G. Ulm, M. Scheer: *Nucl. Instr. Meth.* **A580**, 1536 (2007)
- [21] M. Müller *et al.*: in this publication on p. 57
- [22] A. Fludra *et al.*: *Proc. SPIE* **8862**, 88620F (2013)

Detector-based Radiometry with Cryogenic Radiometers and Monochromatized Synchrotron Radiation

Alexander Gottwald*, Udo Kroth, Michael Krumrey, Peter Müller, Frank Scholze

Introduction

Detector-based radiometry is based on the use of primary detector standards for the measurement of absolute radiant power. For this purpose, electrically calibrated substitution radiometers have – since their introduction more than 100 years ago – been established for optical radiometry [1]. These radiometers are thermal detectors which are based on the equivalence of electrical heating and the radiation heating of an absorber. In the 1980s, the measurement uncertainty was clearly reduced by an operation at the temperature of liquid helium and in connection with lasers [2–7]. Cryogenic electrical substitution radiometers today are used by many national metrology institutes for the realization of the scale of the spectral responsivity of photodetectors from the infrared to the ultraviolet spectral range, whereby the smallest relative uncertainties can be achieved in the range of 10^{-4} when the detectors are used in combination with intensity-stabilized lasers as radiation sources [8].

In the spectral ranges of the vacuum-ultraviolet (VUV), the extreme ultraviolet (EUV) and X-ray radiation, where no lasers exist, monochromatized synchrotron radiation from storage rings offers very good preconditions for detector-based radiometry, in particular due to the broadband radiation and the resulting continuous tunability of the wavelength (in combination with suitable monochromators). In contrast to laser radiation, in the case of which radiant powers of a few milliwatts can typically be used, the power of the monochromatized radiation, which is available at the bending-magnet beamlines, amounts, however, to not more than $50 \mu\text{W}$ (partly to even less than $1 \mu\text{W}$). The stability of the synchrotron radiation is not limited by stochastic variations, but by the continuous, nearly exponential decay of the electron current in the storage ring with

typical time constants in the range of a few hours. In contrast to this so-called decay mode, many storage rings (also at BESSY II) allow operation today in the top-up mode, in the case of which the electron current is kept almost (better than 1 %) constant. To achieve small uncertainties in radiation measurements in the decay mode, the measurements must be performed within a few minutes. Due to the – compared to lasers – relatively low power of synchrotron radiation, ionization chambers have been used for a long time as primary detector standards here [9]. These allow, however, measurements of the radiant power to be performed only with relative uncertainties of a few percent [10].

Conventional cryogenic electrical substitution radiometers are suitable for measurements with synchrotron radiation only after considerable adaptations. In its laboratory – first at the storage ring BESSY I [11], since 1999 at BESSY II [12], and since 2008 also at the *Metrology Light Source* (MLS) [13] – PTB has continuously developed and improved detector-based radiometry with synchrotron radiation on the basis of specially adapted cryogenic radiometers. By now, this technique can be regarded as established and is meanwhile also used by other national institutes, such as NIST and NMIJ [14, 15]. Based on the use of cryogenic electrical substitution radiometers as primary detector standards, and by using monochromatized synchrotron radiation, PTB has established a scale of the spectral responsivity which extends from the UV range to the X-ray range [16–19]. The scale is disseminated by semiconductor photodiodes which have been calibrated against the primary standard, using – as a function of the spectral range – different photodiode types as secondary detector standards.

* Dr. Alexander Gottwald, Working Group "UV and VUV Radiometry", e-mail: alexander.gottwald@ptb.de

PTB's cryogenic radiometers for synchrotron radiation

PTB has two cryogenic radiometers at its disposal which have been especially developed for use with monochromatic synchrotron radiation [20–22]. These thermal detectors, which are called SYRES I and II (SYnchrotron Radiation Electrical Substitution Radiometer) and are based on cavity absorbers, are operated at temperatures slightly above the boiling point of liquid helium. Both systems are windowless and, thus, directly connected to the beamlines for synchrotron radiation [23, 24] under ultra-high-vacuum conditions. Use of a metallic cavity absorber guarantees high absorptance – compared to other absorber types (e.g. disk absorbers) – to be achieved while sec-

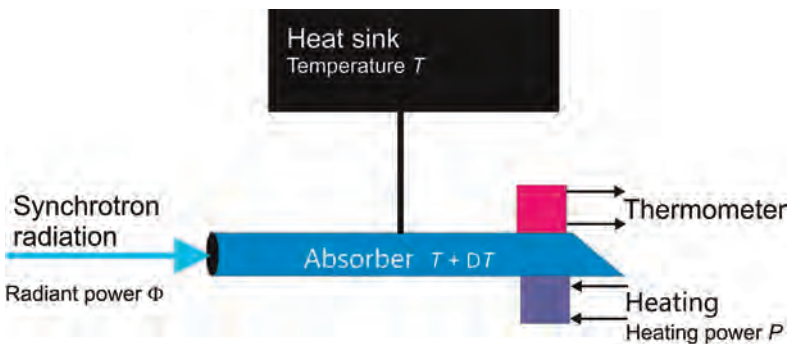


Figure 1: Schematic representation of a cryogenic electrical substitution radiometer with the cavity absorber module.

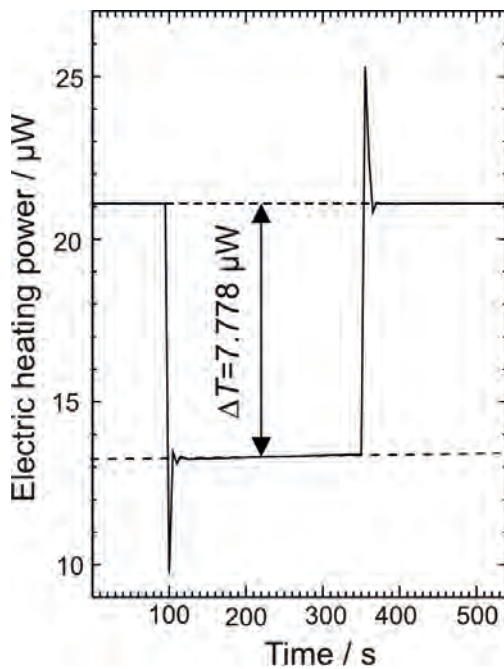


Figure 2: Example of a radiant power measurement with the cryogenic radiometer SYRES II in the substitution mode: 100 s after the measurement has been started, the radiant power to be measured falls for 240 s on the absorber, by which the originally applied electric heating power of the control electronics is reduced by the amount of the absorbed radiant power (here: 7.778 μW).

ondary effects such as photoemission or fluorescence are, at the same time, effectively suppressed. Although the metallic absorbers have – due to the contribution of the conducting electrons – a higher thermal capacity than insulators, they prevent non-thermal energy losses such as, for example, the formation of color centers in insulating absorbers, like sapphire.

Figure 1 shows the essential components of the cryogenic electrical substitution radiometer: A cavity absorber of the thermal capacity C is coupled via a thermal resistance R to a heat sink of the temperature T which is kept constant by means of an electronic control. The heat sink is in thermal contact with a helium-bath cryostat. When irradiated with the radiant power Φ , the temperature of the absorber increases by ΔT compared to the original temperature. The time constant $\tau = R \times C$ of the temperature change is given by $R = \Delta T / \Phi$.

The same temperature increase can be achieved by electrical heating, i.e. the radiant power Φ can be substituted by the electric heating power P . This substitution is based on the assumption that electrical heating and radiation heating are equivalent. Generally, the radiometers are operated in the so-called dynamic substitution mode: Already before the irradiation, the temperature of the absorber is regulated to a constant value ($T + \Delta T$) by electric heating using a resistance heating element. If the radiant power to be determined now is absorbed, the electric heating power must be reduced by exactly the amount to keep the temperature constant (Figure 2). The measurement of the radiant power is, thus, traced to a difference measurement of the electric heating power and to the electrical quantities associated with it.

To adapt the conditions to the special use of synchrotron radiation, some essential modifications are required compared to conventional cryogenic radiometers with cavity absorbers, in particular in view of the sensitivity and the suppression of the thermal radiation background. Due to the low radiation power available, the thermal resistance R must be large to achieve sufficient sensitivity in the range of some ten $\text{mK}/\mu\text{W}$. In addition, the thermal capacity must be small to achieve a justifiably small time constant τ in the range of less than one minute in order to keep the change of the beam intensity due to the monotonously decreasing ring current in the storage ring smaller than the measurement uncertainty aimed at. To implement these requirements, the cavity absorbers of the cryogenic radiometers are made of electrolytically formed copper with a wall thickness of approx. 100 μm . To achieve a high value for the thermal resistance in the coupling to the heat sink, the absorbers are suspended on thin nylon threads. The defined thermal coupling

is realized by a wire, respectively, made of copper or constantan which allows the thermal resistance to be varied to a certain extent by an adaptation of the length.

The uncertainty which can be achieved in the determination of the radiant power is limited by the capacity of the absorber to completely absorb the radiation incident on it (i.e. to have an emissivity close to unity), and to convert it (without losses) into heat. Whereas in the UV and VUV spectral ranges, it is the reflection of the radiation on the surface of the absorber which represents the essential loss factor which must be taken into account, it is the transmission losses (due to insufficient wall thickness) as well as fluorescence and scattering processes which come to the fore in the X-ray range. To allow measurements at photon energies of up to 60 keV to be performed, the cylindrical cavity absorber (40 mm in length) whose wall consists of copper (90 μm in thickness) with a gold layer (approx. 1 μm in thickness) was closed with a solid gold plate (730 μm in thickness) as back wall which is inclined by 30° to the perpendicular (Figure 3a) [23]. This absorber is used in the SYRES-I instrument and enables the radiometric traceability of detector-based calibrations in the photon energy range between 30 eV and 60 keV. The SYRES-II radiometer has, however, been developed for dedicated use in the photon energy range between 3 eV and 30 eV (corresponding to wavelengths of 400 nm to 40 nm). Here, back plate and cylindrical walls of the cavity absorber have almost the same wall thickness; the copper has also been covered with a gold layer (approx. 1 μm in thickness). This layer is to generate as high a directed (specular) reflection as possible. With a length of 80 mm, the cavity absorber is twice as long as the absorber used in the X-ray range. In addition, a so-called retro-reflector, which consists of two truncated cones set with the basis against each other (slope: 30°, length: 9 mm), is installed at the entrance (Figure 3b) [16]. By means of this geometry, a beam, which is completely directed at the back wall of the absorber, is again reflected into the cavity. Leaving of the cavity is possible only after more than 15 reflections on the surface. For an assumed reflectivity of 0.4, the reflection losses are, thus, smaller than 10^{-6} . In the case of the two absorbers used, the electrical heater and a germanium resistance thermometer are applied to the outside of the beveled back wall. To guarantee the equivalence of electrical heating and heating by radiation as well as possible, uncontrolled heat flows must be suppressed. The radiation absorber (cavity absorber) is located in the high vacuum to rule out heat derivation by convection. In these temperature ranges, thermal radiation, too, plays no role in the heat transport. The current leads

for heater and resistance thermometer consist of superconducting materials, so that hardly any Joule's heat is generated in the range of the working temperatures. In addition, an inhomogeneous temperature distribution is minimized by the high thermal conductivity of the absorber material at these low temperatures.

As the beamlines are at ambient temperature, an infrared radiation power of a few milliwatts falls from the semi-infinite space onto the absorber. The whole absorber module must, therefore, be surrounded by a cooled cryocollimator to reduce the solid angle for the incident infrared radiation approximately to that of the synchrotron radiation. In the case of SYRES II, the absorber module can, in addition, be vertically lifted under vacuum from the beam path, together with the associated cryostat, to carry out measurements with the absorber and the detector to be calibrated at exactly the same beam position. In doing so, it is ensured that also exactly the same amount of radiant power falls on the primary detector standard and on the detector to be calibrated, independent of the divergence and of the stray light halo of the beam.

Calibration of transfer detector standards

In the laboratories of PTB at BESSY II and at the MLS, the cryogenic radiometers described in the preceding section are used as primary detector standards to measure the spectral responsivity of transfer detector standards [16–19, 25–32]. The calibration is performed by comparing the measured photocurrent of the transfer detector with the incident radiant power which is measured with the cryogenic radiometer. By the use of monochromatized synchrotron radiation, PTB realizes a scale of the spectral responsivity from the ultraviolet spectral range up to the X-ray

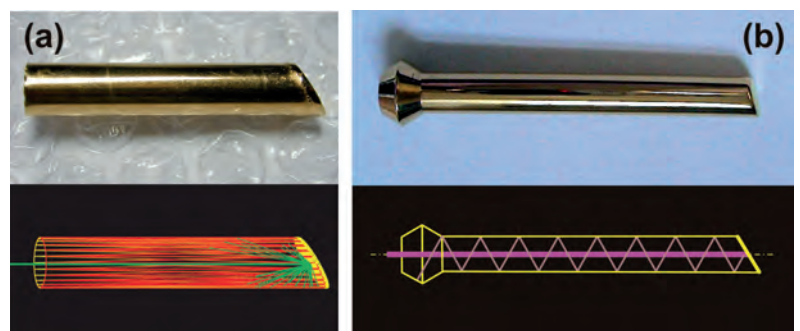


Figure 3:

Cavity absorber of the two SYRES cryogenic radiometers.

(a) SYRES-I absorber, length $l = 40$ mm, diameter $d = 8$ mm; top: photo, bottom: simulated X-ray scattering and fluorescence [23].

(b) SYRES-II absorber $l = 80$ mm, $d = 8$ mm; top: photo, bottom: geometric beam path for direct (specular) reflection of the incident beam [16].

range (Figure 4, top). It is applied to different detector types (semiconductor photodiodes) depending on the respective spectral range. The following detectors are used here: windowless semiconductor photodiodes of the Schottky type (PtSi-nSi-photodiodes) [31], detectors of the nSi-pSi type or *Passivated Implanted Planar Silicon* detectors [23]. Decisive for the selection of the detectors is aspects such as irradiation stability, linearity and homogeneity across the detector surface [30, 31]. Depending on the detector type and even more on the wavelength range and the corresponding instrumentation, different uncertainties are obtained for the scale and for the calibration of transfer detector standards (Table 1). In the UV, VUV and soft X-ray ranges, the largest contribution to the total uncertainty comes from scattered light and higher grating diffraction orders of the monochromatized synchrotron radiation. These contributions differ considerably, depending on the optical configuration of the beamlines in the spectral sub-ranges (filter, grating, etc.) so that the achievable measurement uncertainty is different and shows an abrupt change at the respective range limits (Figure 4, bottom, and Table 1).

The scale of the spectral responsivity represented in this way has been validated by internal and external comparisons. As primary detector standard, SYRES II has, for example, been directly compared against the storage ring MLS as primary source standard [33, 34], whereas for SYRES I in the soft X-ray range, an energy-dispersive Si(Li) detector was used as transfer standard [35]. Further detector-based comparisons were performed against an open-air ionization chamber as another primary detector standard [23] and, with semiconductor photodiodes, against the radiometric scales of other national institutes [36–38].

In the dissemination of the scale, also the properties of the detectors, in particular the homo-

geneity of the responsivity across the detector surface, contribute essentially to the uncertainty budget. The irradiation stability and the general aging of the transfer detectors are, as a matter of principle, a problem in the dissemination of the scale and do not only depend on the detector type, but also on the wavelength and on the power of the incident radiation. Thereby, the aging of a detector relates to both the homogeneity and also to the spectral responsivity [39, 40]. Particularly relevant here is the aging of semiconductor photodiodes in the wavelength range of the VUV, especially for wavelengths between approx. 50 nm and 150 nm [41, 42]. The cause of it lies in the high radiation absorption of all materials in this wavelength range so that the penetration depth of the radiation amounts to only a few nanometers. The whole energy of the incident photons is, thus, absorbed in the thin top layer of the detector. This means, on the one hand, that the quality of the top layer (uniformity, lack of structure errors) essentially determines the properties of the detector and, on the other hand, that this top layer is subject to strong aging processes by radiation damage. A distinction must be made between aging processes and changes in the spectral responsivity by contamination of the detector surfaces. Secondary electrons are emitted from the detector surface – in particular at a sufficiently high energy of the photons (larger than approx. 10 eV, corresponding to wavelengths smaller than 120 nm) – whose kinetic energies are sufficient to chemically break surface-absorbed hydrocarbons and, thus, to generate a constantly increasing, strongly absorbing carbon layer.

Silicon photodiodes are widely used as radiometric secondary standards. Due to the advanced manufacturing techniques, the spectral responsivity of these photodiodes can reach the theoretical maximum value. A natural oxide growth is – in the case of silicon – however, unavoidable, so that

Table 1: Summary of essential uncertainty contributions for the determination of the spectral responsivity of a photodiode against a cryogenic radiometer at four selected photon energies at the respective beamlines [24]. Indicated is the standard measurement uncertainty.

Quantity	Relative standard measurement uncertainty of spectral responsivity ($k = 1$) / %			
	4 eV (NIM)	95 eV (SX700)	5 keV (FCM)	15 keV (BAMline)
Radiant power	0.14	0.11	0.13	0.13
Measurement signal (photocurrent)	0.10	0.10	0.10	0.20
Calibration factor of the electrometer	0.03	0.06	0.01	0.01
Wavelengths	0.02	0.01	0.01	0.02
Spectral bandwidth	0.008	0.001	0.001	0.001
Scattered light, higher diffraction orders	0.15	0.2	<0.001	<0.001
Spectral responsivity	0.25	0.26	0.17	0.25

a technically generated (possibly nitrided) oxide is – as a matter of principle – applied as top layer for passivation. Photodiodes for the visible and near UV spectral ranges can, thereby, even have thick (some 10 nm to 100 nm) oxide layers with antireflection properties. However, for the ranges with even shorter wavelengths, only diode types with ultra-thin (a few nm) passivation layers are suited to produce enough electron-hole pairs in the depletion zone which then lead to a measurable signal. The oxide passivation layer itself is not electrically conductive. Due to the (external) photoeffect, the radiation leads to an electrical (positive) charging of the top layer in the range of the irradiation by which the sensitivity of the photodiode is changed. The use of a metallic silicide top layer instead of the oxide for passivation can remedy the problem [43]. However, it reduces the spectral responsivity in the relevant spectral range by almost one order of magnitude due to the higher absorption in the top layer. Although Schottky photodiodes (with platinum silicide as metallic contact) [31] prove to be very insensitive to irradiation, they are – due to their electrical properties (low internal resistance) – suited for the measurement of small photocurrents only to a limited extent. Photodiodes with different implant ions (e.g. phosphor, arsenic or boron) and implant profiles have, in principle, been known for a long time already [44], however, conventional implantation techniques do not generate sufficiently small depletion zones. Only for some years has it been possible to control corresponding techniques in semiconductor laboratories so that photodiodes for the VUV spectral range with high sensitivity and, at the same time, high resistance to radiation [45] have become available.

In addition to the semiconductor photodiodes which are also used internally as transfer standards, also other radiation detector types are calibrated (for example: vacuum photocathodes, photomultipliers and bolometers) [46]. Spatially resolved calibrations of imaging detectors such as, for example, *Charged Coupled Devices* (CCD) [47] or sensors with individually readable pixels (*Active Pixel Sensors*, APS) [48] are possible.

For the measurement of highly intensive, pulsed radiation of free-electron lasers, especially developed detectors, based on the atomic photoionization of (noble) gases, have been calibrated traceably to a cryogenic radiometer [49, 50].

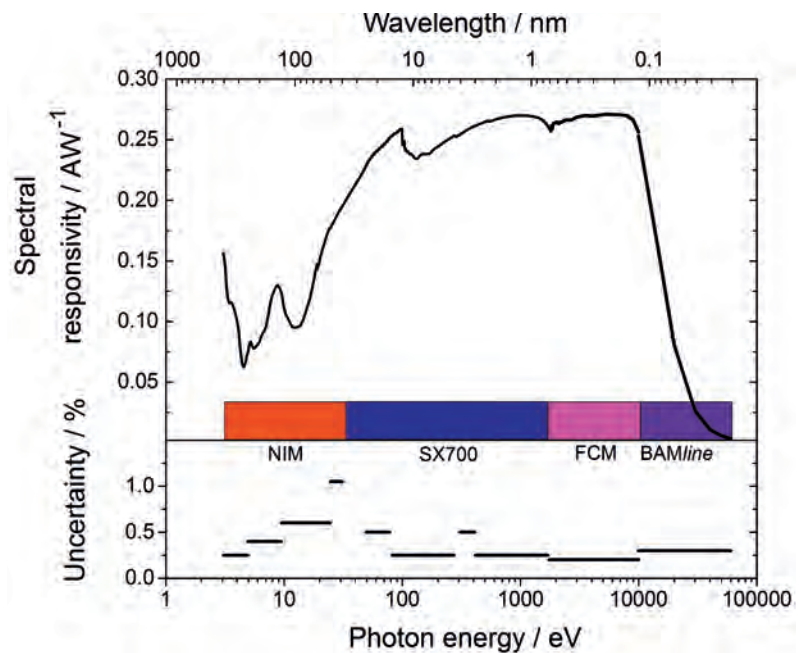


Figure 4:

The PTB scale of spectral responsivity as it is realized by the use of monochromatized synchrotron radiation and cryogenic electrical substitution radiometers and applied – depending on the photon energy range – to different (here not separately identified) silicon semiconductor photodiodes (top), as well as the associated relative standard uncertainties in the dissemination (calibration of transfer standards). The abbreviations relate to the spectral ranges of the different beamlines used [24], see Table 1.

References

- [1] F. Kurlbaum: *Ann. Phys.* **287**, 591 (1894)
- [2] T. J. Quinn, J. E. Martin: *Philos. Trans. R. Soc. London Ser. A* **316**, 85 (1985)
- [3] J. E. Martin, N. P. Fox, P. G. Key: *Metrologia* **21**, 147 (1985)
- [4] N. P. Fox: *Metrologia* **32**, 535 (1995–1996)
- [5] T. J. Quinn, J. E. Martin: *Metrologia* **28**, 155 (1991)
- [6] T. R. Gentile, J. M. Houston, J. E. Hardis, C. L. Cromer, A. C. Parr: *Appl. Opt.* **35**, 1056 (1996)
- [7] N. P. Fox, J. E. Martin: *Appl. Opt.* **29**, 4686 (1990)
- [8] I. Müller *et al.*: *Metrologia* **50**, 395 (2013)
- [9] J. A. R. Samson: *J. Opt. Soc. Am.* **54**, 6 (1964)
- [10] L. R. Canfield, N. Swanson: *J. Res. NBS* **92**, 97 (1987)
- [11] G. Ulm, B. Wende: *Rev. Sci. Instrum.* **66**, 2244 (1995)
- [12] R. Klein, M. Krumrey, M. Richter, F. Scholze, R. Thornagel, G. Ulm: *Synchrotron Radiation News* **15**, No.1, 23 (2002)
- [13] A. Gottwald, R. Klein, R. Müller, M. Richter, F. Scholze, R. Thornagel, G. Ulm: *Metrologia* **49**, S146 (2012)
- [14] P. S. Shaw, K. R. Lykke, R. Gupta, T. R. O'Brian, U. Arp, H. H. White, T. B. Lucatorto, J. L. Dehmer, A. C. Parr: *Appl. Opt.* **38**, 18 (1999)
- [15] Y. Morishita, N. Saito, I. H. Suzuki: *J. Electr. Spectr. Rel. Phen.* **144–147**, 1071 (2005)
- [16] A. Gottwald, U. Kroth, M. Krumrey, M. Richter, F. Scholze, G. Ulm: *Metrologia* **43**, S125 (2006)
- [17] A. Gottwald, U. Kroth, M. Richter, H. Schöppe, G. Ulm: *Meas. Sci. Technol.* **21**, 125101 (2010)
- [18] F. Scholze, J. Tümmeler, G. Ulm: *Metrologia* **40**, 224 (2003)
- [19] M. Krumrey, G. Ulm: *Nucl. Instr. and Meth. A* **467–468**, 1175 (2001)
- [20] A. Lau-Främbis, U. Kroth, H. Rabus, E. Tegeler, G. Ulm: *Rev. Sci. Instrum.* **66**, 2324 (1995)
- [21] A. Lau-Främbis, U. Kroth, H. Rabus, E. Tegeler, G. Ulm, B. Wende: *Metrologia* **32**, 571 (1995/96)
- [22] H. Rabus, V. Persch, G. Ulm: *Appl. Opt.* **36**, 5421 (1997)
- [23] M. Gerlach, M. Krumrey, L. Cibik, P. Müller, H. Rabus, G. Ulm: *Metrologia* **45**, 577 (2008)
- [24] M. Richter, G. Ulm: in this publication on p. 3
- [25] H. Rabus, E. Tegeler, G. Ulm, B. Wende: *PTB-Mitteilungen* **104**, 343 (1994)
- [26] H. Rabus, F. Scholze, R. Thornagel, G. Ulm: *Nucl. Instr. and Meth. A* **377**, 209 (1996)
- [27] F. Scholze, H. Henneken, P. Kuschnerus, H. Rabus, M. Richter, G. Ulm: *J. Synchrotron Rad.* **5**, 866 (1998)
- [28] H. Rabus, R. Klein, F. Scholze, R. Thornagel, G. Ulm: *Metrologia* **39**, 381(2002)
- [29] B. Beckhoff, R. Klein, M. Krumrey, F. Scholze, R. Thornagel, G. Ulm: *Nucl. Instr. and Meth. A* **444**, 480 (2000)
- [30] M. Richter, J. Hollandt, U. Kroth, W. Paustian, H. Rabus, R. Thornagel, G. Ulm: *Metrologia* **40**, 107 (2003)
- [31] K. Solt, H. Melchior, U. Kroth, P. Kuschnerus, V. Persch, H. Rabus, M. Richter, G. Ulm: *Appl. Phys. Lett.* **69**, 3662 (1996)
- [32] P. Kuschnerus, H. Rabus, M. Richter, F. Scholze, L. Werner, G. Ulm: *Metrologia* **35**, 355 (1998)
- [33] R. Klein, A. Gottwald, G. Brandt, R. Fliegau, A. Hoehl, U. Kroth, H. Kaser, M. Richter, R. Thornagel, G. Ulm: *Metrologia* **48**, 219 (2011)
- [34] R. Klein, R. Thornagel, G. Ulm: in this publication on p. 7
- [35] F. Scholze: *M. Procop, X-Ray Spectrom.* **30**, 69 (2001)
- [36] F. Scholze, R. Vest, T. Saito: *Metrologia* **47**, 02001 (2010)
- [37] A. Gottwald, M. Richter, P.-S. Shaw, Z. Li, U. Arp: *Metrologia* **48**, 02001 (2011)
- [38] T. Tanaka, M. Kato, T. Kurosawa, Y. Morishita, N. Saito, I. H. Suzuki, M. Krumrey, F. Scholze: *Metrologia* **49**, 501 (2012)
- [39] F. Scholze, R. Klein, R. Müller: *Proc. SPIE* **5374**, 926 (2004)
- [40] F. Scholze, R. Klein, T. Bock: *Appl. Opt.* **42**, 5621 (2003)
- [41] M. Richter, U. Kroth, A. Gottwald, Ch. Gerth, K. Tiedtke, T. Saito, I. Tassy, K. Vogler: *Appl. Opt.* **41**, 7167 (2002)
- [42] L. Shi, S. Nihitianov, S. Xia, L. K. Nanver, A. Gottwald, F. Scholze: *IEEE Trans. Instrum. Meas.* **61**, 1268 (2012)
- [43] R. Korde, C. Prince, D. Cunningham, R. Vest, E. Gullikson: *Metrologia*, **40**, S145 (2003)
- [44] R. Korde, J. Geist: *Solid State Electron.* **30**, 89 (1987)
- [45] P. N. Aruev, Yu M. Kolokolnikov, N. V. Kovalenko, A. A. Legkodymov, V. V. Lyakh, A. D. Nikolenko, V. F. Pindyurin, V. L. Sukhanov, V. V. Zabrodsky: *Nucl. Instrum. Meth. A* **603**, 58 (2009)
- [46] H. Meister, M. Willmeroth, D. Zhang, A. Gottwald, M. Krumrey, F. Scholze: *Rev. Sci. Instrum.* **84**, 123501 (2013)
- [47] S. Granato, R. Andritschke, J. Elbs, N. Meidinger, L. Strüder, G. Weidenspointner, M. Krumrey, F. Scholze: *IEEE Trans. Nucl. Sci.* **60**, 3150 (2013)
- [48] A. BenMoussa *et al.*: *IEEE Trans. Nucl. Sci.* **60**, 3907 (2013)
- [49] K. Tiedtke *et al.*: *J. Appl. Phys.* **103**, 094511 (2008)
- [50] M. Richter, A. Gottwald, M. Krumrey: in this publication on p. 27

Metrology for X-ray Lasers

Mathias Richter*, Alexander Gottwald, Michael Krumrey

Since the early days of research with synchrotron radiation [1], the respective accelerator-based radiation sources have constantly been further developed [2]. In the so-called *third generation*, the operation of insertion devices in the straight sections of storage rings has been optimized since the 1990s, especially the operation of undulators which emit highly brilliant radiation of variable polarization [3–6]. The latest developments are aimed at generating radiation pulses of less than 1 ps duration by means of optimized accelerator structures, e.g. with free-electron lasers (FELs) for time-resolved experiments on very rapid chemical processes. Among the FEL facilities which are currently in operation – FLASH in Hamburg [7], FERMI in Trieste [8], LCLS in Stanford [9] as well as SCSS [10] and SACLA [11] in Japan – all, except FERMI, are based on the principle of *Self-Amplified Stimulated Emission* (SASE). Thereby, very short electron bunches with relativistic energies are generated in a linear accelerator where a clearly better electron bunch focusing and compression, compared to ring accelerators, is possible. Due to this, the undulator radiation generated in a downstream undulator is so brilliant that there is a significant electromagnetic feedback with the electrons. This leads to microstructuring of the electron bunches with the period of the radiation wavelength, and to a coherent emission of FEL radiation which is amplified by many magnitudes. Meanwhile, photon energies between 20 eV and 20 keV are attained for pulse energies up to several mJ. Pulse durations between 10 fs and 500 fs thus lead to a radiation power of more than 10 GW in a single pulse.

As in an FEL pulse of a duration of less than 1 ps, approximately as many X-ray photons are available as in the case of synchrotron radiation in one second, FEL experiments can be carried out in a pulse-resolved mode. However, the SASE principle implies strong pulse-to-

pulse variations – especially of intensity or pulse energy – which calls for real-time photon diagnostics. PTB has accompanied the development and the characterization of the respective detection systems from the very beginning [12]. For the worldwide first SASE-FEL with a user operation – FLASH in Hamburg – so-called *gas monitor detectors* (GMDs) were designed in cooperation with the *Deutsches Elektronen-Synchrotron* (DESY) in Hamburg and the *Ioffe Institute* in St. Petersburg and installed at the laser output in front of the experimental area [13]. These are based on the photoionization of gases and the detection of the generated photoions and photoelectrons. In Figure 1, such a system is shown. At typical gas pressures in the range between 10^{-2} Pa and 10^{-3} Pa, the detector transmission of FEL radiation for

* Prof. Dr. Mathias Richter, Department "Radiometry with Synchrotron Radiation", e-mail: mathias.richter@ptb.de

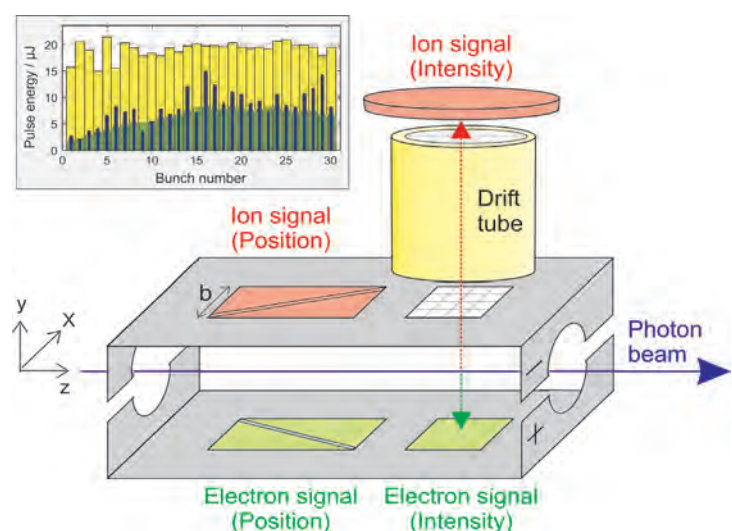


Figure 1: Scheme of a gas monitor detector (GMD) at FLASH for the real-time measurement of FEL intensity and beam position. Top left, the display in the FLASH control system for pulse energies measured by means of a GMD is represented (blue: values for the current pulse train; yellow: maximum value of the pulse trains as of display start; green: mean values of the pulse trains as of display start) [13].

the experiments is beyond 99 %. Prior to their installation, the detectors were calibrated traceably in PTB's laboratory at BESSY II [14] – against calibrated photodiodes – to a cryogenic radiometer as a primary detector standard [15]. Therefore, they are continuously providing absolute information on pulse energies with relative uncertainties in the range of $\pm 15\%$. In addition, the FEL beam position can be measured by means of split electrodes [13].

Improved versions of GMD are also suited for mobile use, e.g. in order to quantitatively detect the radiation of *High Harmonic Generation* (HHG) [16], or for measurements carried out at other FELs [17–19]. For the harder X-ray region up to photon energies in the range of 20 keV, an option of signal amplification by the use of open multipliers was developed in order to compensate for the photoionization cross sections which are lower by orders of magnitude there.

An important aspect during measurements with DESY-PTB-GMDs on – meanwhile – all FELs in operation was the validation of the measure-

ment and calibration procedure. Both at lower photon energies in the range between 20 eV and 25 eV [17] and in the X-ray range between 4 keV and 14 keV [18], radiometric comparisons took place at the Japanese FEL facilities SCSS and SACLA by means of a cryogenic radiometer of the Japanese metrology institute AIST/NMIJ. In these comparisons, a good agreement was achieved within the scope of the combined measurement uncertainties. Especially non-linear processes, such as multiphoton ionization, can influence the GMD measurements on an FEL essentially, compared to the calibration with synchrotron radiation, where the number of photons of a single FEL pulse was distributed to 10^8 to 10^9 pulses. Therefore, the non-linear influences on the photoionization were also systematically and quantitatively investigated at FLASH by means of focused FEL radiation [20–22]; however, these influences have proved to be negligible outside of focal regimes with irradiances below 10^{12} W/cm².

Figure 2 shows the experimental set-up of such a photoionization experiment, in which a spherical EUV multilayer mirror [23] in back reflection geometry generates a micro-focus. In the interaction zone of an ion time-of-flight spectrometer, irradiances of up to 10^{16} W/cm² could be generated at a photon energy of 93 eV, whereby the incident unfocused radiation was blocked for the experiment. Mirror and focus could be displaced along the beam axis; the beam cross section and the irradiance were thus varied for the experiment in a defined way. Figure 3 shows a series of ion time-of-flight spectra for xenon [22], from which the respective distribution of the charge states generated during the photoionization can be read. Whereas the spectrum recorded at $2.5 \cdot 10^{12}$ W/m², having the charge states Xe¹⁺, Xe²⁺ and Xe³⁺, corresponds largely to the single photoionization of xenon from the 5*p*- or 4*d*-shell with subsequent Auger decay, the higher charge states at higher irradiances are the result of non-linear multiphoton processes. In the past few years, a controversial debate has been triggered on the ionization mechanisms, especially for the very high charges up to Xe⁺²¹ [22, 24–29], and the xenon work became the starting point for numerous further studies, also PTB's own studies in cooperation with various partners. The latter refer to comparisons between different noble gases [25, 30] with electron spectroscopy [31] as well as to measurements at different FEL pulse durations [29, 32].

Non-linear processes on the photoionization of gases were also used for additional FEL photon diagnostics. To obtain information, e.g., on the size of micro-foci, the effect that an individual FEL pulse can depopulate a significant part of the targets in the focal zone by means of photoion-

Figure 2: Scheme of a gas-phase photoionization experiment at FLASH with an ion time-of-flight (TOF) spectrometer in the focus of a spherical multilayer mirror.

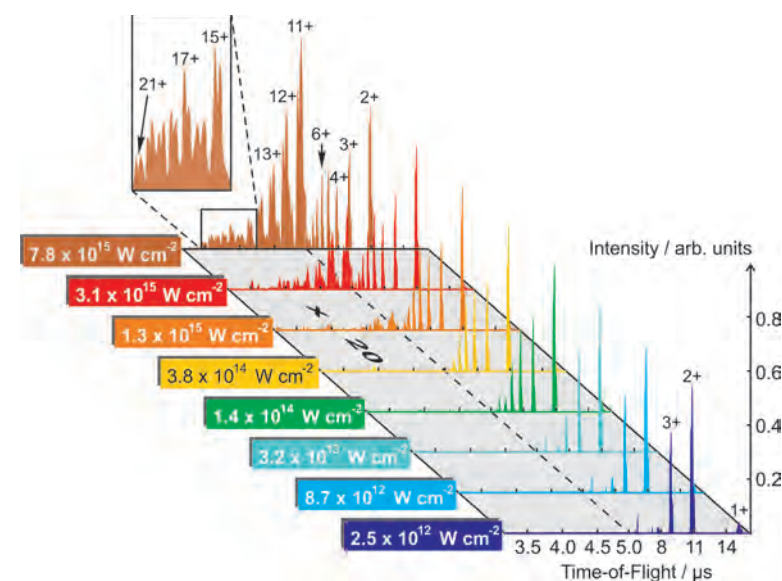
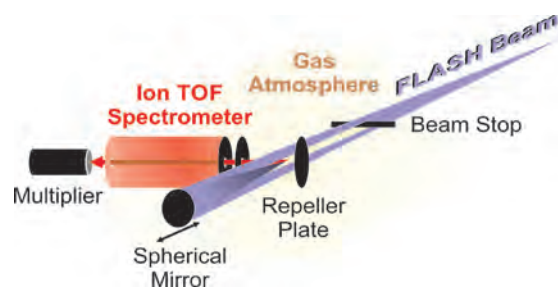


Figure 3: Ion time-of-flight spectra of xenon, recorded at a photon energy of 93 eV and various irradiances [22].

ization, was exploited. In this way, even for single photon processes, the ionization signal does not increase linearly to the pulse intensity any longer, but reaches saturation, from which the FEL beam cross section can be evaluated [33]. However, the two-photon double ionization of helium is – per se – a non-linear process which quadratically increases along with the irradiance [21, 26], from which the FEL pulse duration can be determined [34, 35].

References

- [1] D. H. Tomboulion, P. L. Hartman: Phys. Rev. **102**, 1423 (1956)
- [2] <http://www.lightsources.org/> (retrieved: 2015-04-23)
- [3] P. J. Duke: Synchrotron Radiation: Production and Properties, Oxford University Press, Oxford (2000)
- [4] H. Wiedemann: Synchrotron Radiation, Springer, Berlin (2002)
- [5] A. Hofmann: The Physics of Synchrotron Radiation, Cambridge University Press, Cambridge (2004)
- [6] T. Möller, J. Falta (Eds.): Forschung mit Synchrotronstrahlung, Vieweg+Teubner, Wiesbaden (2010)
- [7] W. Ackermann et al.: Nat. Photonics **1**, 336 (2007)
- [8] S. Di Mitri et al.: Proc. IPAC **2011**, 918 (2011)
- [9] P. Emma et al.: Nat. Photonics **4**, 641 (2010)
- [10] T. Shintake et al.: Nat. Photonics **2**, 555 (2008)
- [11] P. David et al.: Nat. Photonics **5**, 456 (2011)
- [12] M. Richter et al.: Appl. Phys. Lett. **83**, 2970 (2003)
- [13] K. Tiedtke et al.: J. Appl. Phys. **103**, 094511 (2008)
- [14] M. Richter, G. Ulm: in this publication on p. 3
- [15] A. Gottwald, U. Kroth, M. Krumrey, P. Müller, F. Scholze: in this publication on p. 21
- [16] T. Leitner, A. A. Sorokin, J. Gaudin, H. Kaser, U. Kroth, K. Tiedtke, M. Richter, Ph. Wernet: New J. Phys. **13**, 093003 (2011)
- [17] N. Saito et al.: Metrologia **47**, 21 (2010)
- [18] M. Kato et al.: Appl. Phys. Lett. **101**, 023503 (2012)
- [19] K. Tiedtke et al.: Opt. Express **22**, 21214 (2014)
- [20] A. A. Sorokin, S. V. Bobashev, K. Tiedtke, M. Richter: J. Phys. B: At. Mol. Opt. Phys. **39**, L299 (2006)
- [21] A. A. Sorokin, S. V. Bobashev, K. Tiedtke, M. Wellhöfer, M. Richter: Phys. Rev. A **75**, 051402(R) (2007)
- [22] A. A. Sorokin, S. V. Bobashev, T. Feigl, K. Tiedtke, H. Wabnitz, M. Richter: Phys. Rev. Lett. **99**, 213002 (2007)
- [23] F. Scholze, C. Laubis, A. Barboutis, C. Buchholtz, A. Fischer, J. Puls, C. Stadelhoff: in this publication on p. 43
- [24] M. G. Makris, P. Lambropoulos, A. Mihelič: Phys. Rev. Lett. **102**, 033002 (2009)
- [25] M. Richter, M. Ya. Amusia, S. V. Bobashev, T. Feigl, P. Juranic, M. Martins, A. A. Sorokin, K. Tiedtke: Phys. Rev. Lett. **102**, 163002 (2009)
- [26] M. Richter, S. V. Bobashev, A. A. Sorokin, K. Tiedtke: J. Phys. B: At. Mol. Opt. Phys. **43**, 194005 (2010)
- [27] M. Richter: J. Phys. B: At. Mol. Opt. Phys. **44**, 075601 (2011)
- [28] P. Lambropoulos, K. G. Papamihail, P. Decleva: J. Phys. B: At. Mol. Opt. Phys. **44**, 175402 (2011)
- [29] M. Richter, A. A. Sorokin, K. Tiedtke: Proc. SPIE **8778**, 877808 (2013)
- [30] R. Guichard, M. Richter, J.-M. Rost, U. Saalmann, A. A. Sorokin, K. Tiedtke: J. Phys. B **46**, 164025 (2013)
- [31] V. Richardson et al.: Phys. Rev. Lett. **105**, 013001 (2010)
- [32] N. Gerken, S. Klumpp, A. A. Sorokin, K. Tiedtke, M. Richter, V. Bürk, K. Mertens, P. Juranic, M. Martins: Phys. Rev. Lett. **112**, 213002 (2014)
- [33] A. A. Sorokin et al.: Appl. Phys. Lett. **89**, 221114 (2006)
- [34] R. Mitzner et al.: Phys. Rev. A **80**, 025402 (2009)
- [35] S. Düsterer et al.: Phys. Rev. STAB **17**, 120702 (2014)

Radiometric Characterization of Space Instrumentation

Alexander Gottwald*, Roman Klein, Michael Krumrey, Peter Müller, Wolfgang Paustian, Thomas Reichel, Frank Scholze, Reiner Thornagel

* Dr. Alexander Gottwald, Working Group "UV and VUV Radiometry", e-mail: alexander.gottwald@ptb.de

Year of Calibration	Wavelength Range/ nm	Instrument	Mission
1994	50 to 160	SUMER <i>Solar Ultraviolet Measurements of Emitted Radiation</i>	SOHO <i>Solar and Heliospheric Observatory</i>
1994	15 to 80	CDS <i>Coronal Diagnostic Spectrograph</i>	
1996	15 to 80	SERTS <i>Solar EUV Rocket Telescope and Spectrograph</i>	
1997	0.1 to 10	Chandra	
1998	0.1 to 10	EPIC <i>European Photon Imaging Camera</i>	XMM Newton X-ray Multi Mirror
1998	1 to 20	SEE XPS <i>Solar EUV Experiment XUV Photometer System</i>	TIMED <i>Thermosphere Ionosphere Mesosphere Energetics and Dynamics</i>
1998	1 to 20	XPS <i>XUV Photometer System</i>	SORCE <i>Solar Radiation and Climate Experiment</i>
2004	115 to 135	TWINS <i>Two Wide-Angle Imaging Neutral-Atom Spectrometers</i>	
2004	15 to 80	EIS <i>EUUV Imaging Spectrometer</i>	SOLAR-B
2005	15 to 80	MOSES <i>Multi-Order Solar EUV Spectrograph</i>	
2005	0.02 to 0.1	GBM <i>Gamma ray Burst Monitor</i>	Fermi <i>Gamma-Ray Space Telescope</i>
2007	17 to 37	EUNIS <i>Extreme Ultraviolet Normal Incidence Spectrometer</i>	
2005 2006 2007	1 to 240	LYRA <i>Lyman-alpha Radiometer</i> SWAP <i>Sun Watching using APS</i>	PROBA II <i>Project for On Board Autonomy</i>
2004 2006	10 to 240	SOL-ACES <i>Solar Auto-Calibrating EUV/UV Spectrophotometers</i>	SOLAR <i>Solar Monitoring Observatory / ISS</i>
2002 2007	10 to 240	SOL-SPEC <i>Solar Spectral Irradiance Measurement</i>	
2008	0.1 to 2.4	SphinX <i>Solar Photometer in X-Rays</i>	CORONAS
2009	0.1 to 12	eROSITA <i>extended Roentgen Survey with an Imaging Telescope Array</i>	Spektrum Röntgen Gamma
2011	0.1 to 2.5	MIXS <i>Mercury Imaging X-ray Spectrometer</i>	BepiColombo
2010 to 2016	10 to 240	EUI <i>Extreme Ultraviolet Imager</i>	SoI <i>Solar Orbiter</i>
2012 to 2015	70 to 105	SPICE <i>SPectral Imaging of the Coronal Environment</i>	

Figure 1: Overview of the calibrations of space instruments at PTB using synchrotron radiation. Source-based calibrations [1] are highlighted in yellow, whereas detector-based calibrations [2] are highlighted in blue.

Introduction

The Earth's atmosphere absorbs the short-wave fraction of the electromagnetic spectrum, starting with the ultraviolet (UV) spectral range up to the range of X-rays. This may be an important protection mechanism for life on the surface of the Earth, but it makes the exploration of space more difficult: measurements of the emission of stellar objects in this spectral range can only be carried out outside the Earth's atmosphere. Hereby, this fraction of the spectrum is of primary importance, not only for the observation and understanding of the astrophysical and solar processes, but also due to the intensive interaction with the Earth's outer atmosphere and the corresponding climatological and chemical significance of the atmosphere.

To ensure reliable and comparable measurements of space-based instruments, these have to be carefully characterized and traced to radiometric standards. For more than 20 years now, PTB has, within the scope of numerous joint research projects with external partners, established itself as the world leader in characterizing space instrumentation by means of synchrotron radiation in the spectral ranges from UV radiation to X-rays. Various technologies were used for the radiometric support of a series of missions – most of them dedicated to solar radiometry. Another important point is, especially in the X-ray range, the characterization of imaging X-ray-optical elements; for this task, the European Space Agency (ESA) ordered its own beamline section. Figure 1 shows a selection of instruments that were characterized or calibrated by PTB using synchrotron radiation. The different colors serve to differentiate instruments where the method is source-based (yellow) [1] from those where it is detector-based (blue) [2]. Starting with the supply and calibration of transfer standards for the *Solar and Heliospheric Observatory* (SOHO) in 1994 [3], methods and

instrumentation have constantly been developed. Since 2013, a dedicated vacuum tank for the calibration of flight instrumentation of up to 1.20 m in length and a mass of up to 100 kg has been available at the *Metrology Light Source* (MLS) (see Fig. 2). It was used for the first time to calibrate the spectrometers for the *Solar Orbiter* (SolO) mission starting in 2018 – which is the direct successor of the SOHO mission.

Source-based calibration of spectrographs for solar radiometry

The source-based calibration of spectrographs can be carried out either directly with the calculable primary radiation of the electron storage ring, or with the aid of transfer radiation sources whose calibration is, in turn, traced to the electron storage ring as a primary source standard. Calibration using the first method must be categorically carried out at the electron storage ring, so that the required infrastructure (e.g. an adequate vacuum chamber, cleanroom environment, etc.) must therefore be available. With its flexible operation modes, the MLS is an ideal source for this task. It allows variation of the spectral radiant intensity over a wide range by adapting the electron current correspondingly. This allows, for example, the linearity and the saturation behavior in the responsivity of the spectrometer to be investigated. The spectral slope of the radiation can be changed by adapting the electron energy. At the MLS, the electron energy can be reduced from the nominal value of 630 MeV down to 105 MeV, so that shorter wavelengths, which could possibly lead to higher diffraction orders in the spectrographs under calibration, are considerably suppressed. One of the advantages of direct calibration is that transfer sources can be dispensed with, thus allowing smaller uncertainties. Also, calibration is possible at all wavelengths, since synchrotron radiation supplies a continuous “white” spectrum. Last but not least, large inlet apertures of the instruments can be illuminated as a whole. Attention must, however, be paid to the fact that synchrotron radiation is highly polarized, which may require two calibrations to be carried out at two orientations differing from each other by 90°, vertically from the incident radiation. Due to the white spectrum caused by the use of grating spectrographs, higher diffraction orders may occur; they must be suppressed by appropriate means. An example of this is the calibration of the SPICE (*SPECTral Imaging of Coronal Environment*) [4] spectrograph for the Solar Orbiter Mission. This spectrograph operates in diverse wavelength sections in the spectral range from approx. 45 nm to 110 nm. Using synchrotron radiation, it is possible to illuminate the whole inlet aperture of

43.5 mm x 43.5 mm – which would not be the case with the transfer sources available. For the calibration of the wavelength section around 100 nm, calibration can be carried out at a reduced electron energy of approx. 150 MeV. This allows the intensity ratio of 50 nm photons to 100 nm photons to be reduced by approximately two orders of magnitude compared with the MLS operated at nominal energy, so that the intensity of any possible higher diffraction orders is considerably reduced.

The calibrations of the spectrographs *Coronal Diagnostic Spectrometer* (CDS)[5] and SUMER (*Solar Ultraviolet Measurement of Emitted Radiation*) [6] of the SOHO mission are excellent examples of calibrations carried out using transfer sources provided by PTB. These spectrographs were calibrated at the respective institute of the instruments’ developers (at the *Max Planck Institute for Solar System Research* (MPS) for SUMER and at the *Rutherford Appleton Laboratory* (RAL) for CDS). The calibration of the SOHO spectrographs was later validated several times by means of NASA’s sounding rocket SERTS (*Solar EUV Rocket Telescope and Spectrograph*) whose calibration, in turn, took place at RAL, in cooperation with PTB, through the use of the CDS source. Numerous other examples of source-based calibration of spectrometers are shown in Figure 1. Hereby, the SUMER source, the CDS source or calibrated deuterium lamps were used as transfer radiators.

The above-mentioned SUMER and CDS transfer sources are based on a hollow-cathode discharge. Maintenance of the hollow cathode must take place after approximately 10 hours in operation, i.e. the cathode is replaced and the anode is

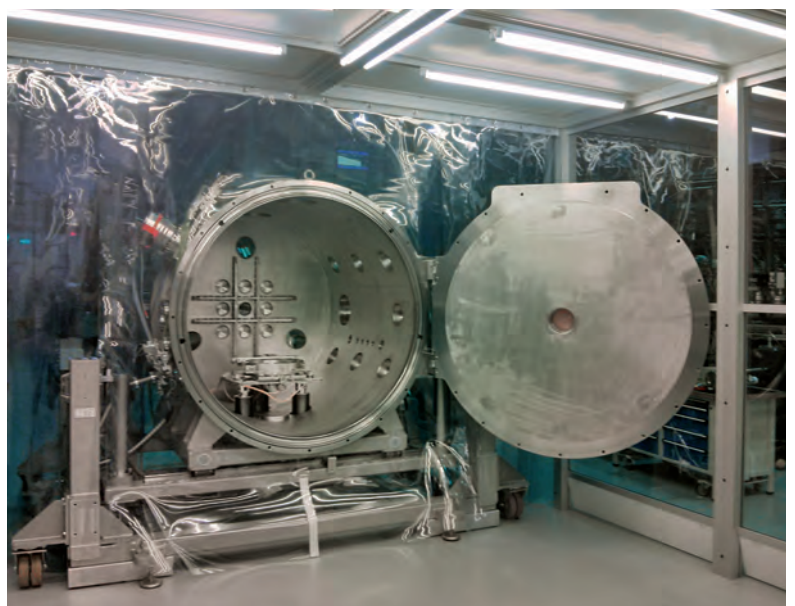


Figure 2: Large vacuum tank for the calibration of space instrumentation at the MLS. For loading and unloading, the tank is located in a cleanroom environment.



Figure 3:
View into the area of the MLS measuring hall that is used for the source-based calibration of space instruments. In the background (top right), one can see the large tank (Figure 2). The tank is flanged at the end of the beamline to utilize the direct, calculable radiation of the MLS. As an alternative, another source such as the SUMER transfer source (bottom right) can be positioned in the beam path. This source can be calibrated at the neighboring measuring station (top left) and traced to the MLS [1].

cleaned. Calibration by means of transfer sources taking place at PTB's lab instead of the home lab of the instruments' developer offers the possibility of re-calibrating the transfer source soon after maintenance, so that the calibration uncertainties which can be achieved with transfer sources are substantially improved. Figure 3 provides an overview of the laboratory area at the MLS which is used for source-based radiometry, with the beamlines and the measuring stations M2a and M2b [7].

Detector-based radiometric characterization of space instrumentation

Besides source-based radiometry [1], for which the electron storage ring is used as a calculable primary source standard, also detector-based radiometry with synchrotron radiation [2] is used to characterize and calibrate instruments with components for outer-space missions at the diverse corresponding beamlines at BESSY II and at the MLS [7]. Radiometric quantities are hereby traced to electrically calibrated cryogenic radiometers as primary detector standards for the measurement of absolute radiation power of monochromatized synchrotron radiation. Similar to the optical spectral range, semiconductor photodiodes have meanwhile established themselves as the respective transfer detector standards also in the range of UV and VUV radiation as well as for X-rays. Existing commercially available semiconductor photodiodes, however, do not live up to all the requirements of the actual detection systems in these short-waved spectral ranges. In general, high

requirements are placed on the spectral sensitivity of radiation detectors, especially with regard to radiation resistance. When used for space instrumentation, this not only includes resistance to the intensity of the radiation to be detected, but especially to particle radiation (e.g. protons) which they are exposed to in their operational environment [8]. In addition, particular requirements result from the fact that the detectors must be "solar blind", i.e. insensitive to visible and infrared radiation [9]. For this purpose, semiconducting wide-band-gap materials (such as aluminum gallium nitride) are used instead of silicon, so that the energy of the photons in the visible spectral range is not sufficient to generate a photocurrent. For spectrographs and imaging telescope systems, imaging detectors are developed which require spatially resolved characterization. Besides line-based detectors (*Charged Coupled Device, CCD*), components in which each pixel can be read out separately via a downstream on-chip electronic unit (*Active Pixel Sensor, APS*) [10] are increasingly being used.

Besides characterizing and calibrating radiation detectors, PTB also characterizes individual optical components (mirrors, filters, diffraction gratings) for space instruments with regard to their spectral reflection, transmission or diffraction efficiency, using the reflectometers available at PTB's laboratories [11]. Similarly to radiation detectors, hardness to all kinds of radiation is an important aspect for use also for optical components. Since it is possible to measure spectral properties with small relative uncertainties (1 % or better), the radiation hardness of different reflecting coatings or thin-film filters can be investigated by carrying out measurements before and after irradiation.

Complete spectrometer systems can also be calibrated by means of detector-based radiometry (Figure 1) by using monochromatized radiation. Whether an instrument is more suitable for source-based or for detector-based calibration cannot be answered categorically; in each individual case, it depends on the properties of the respective spectrometer (e.g. inlet aperture, angular acceptance, wavelength range, etc.).

X-ray astronomy

In the universe, usual matter is, for the major part, available in the form of hot gas. At temperatures of more than 10^7 K, the gas emissions are particularly intensive in the X-ray range. Since this type of radiation cannot penetrate the Earth's atmosphere, such investigations must be carried out in space using an X-ray observatory with high sensitivity, good spectral resolution and a large field of view. Observing the emission lines of different chemical elements provides information about the creation

and the development of black holes and of faraway galaxies under the influence of dark matter and dark energy.

At its former lab at BESSY I, PTB had already contributed to the calibration of the instruments for the two existing X-ray satellites XMM-Newton of ESA and Chandra of NASA [12, 13]. At PTB's lab at BESSY II, components for future X-ray missions of ESA are currently being investigated. One of the next large-scale missions, which will probably start in 2028, is dedicated to "The hot and energetic universe". For this purpose, the *Advanced Telescope for High-Energy Astrophysics* (ATHENA) has already been developed as the concept of the mission [14]; it is based on the concepts of the missions IXO (*International X-ray Observatory*) and XEUS (*X-ray Evolving Universe Spectroscopy*) which were, however, never implemented. The envisaged effective mirror surface of approx. 2 m² corresponds, at grazing incidence for, e.g., 1 keV radiation, to a real mirror surface of 600 m² which must be realized with small form errors and high rigidity whilst keeping it as lightweighted as possible. The solution consists in stacking many small mirror surfaces. With Si wafers with ribs on their reverse side, *silicon pore optics* (SPO) with a large number of mirror channels can be realized; their inlet aperture is typically 1 mm², and their length 70 mm (Figure 4, top) [15].

The quality of each of the mirror channels can only be investigated with a pencil beam at grazing incidence onto the reflecting surface. For this purpose, the *X-ray Pencil Beam Facility* (XPBF) has been set up at PTB's lab at BESSY II [7, 15]. Since 2005, the lab has been equipped with a collimated X-ray beam (diameter: 100 μm, divergence: < 5 μrad) with a fixed photon energy of 2.8 keV. For special investigations, it is, however, possible to set the energy to 1 keV or 7.6 keV. The mirror element to be investigated can be positioned with reproducibilities of 2 μm and < 5 μrad with the aid of a hexapod which is under vacuum (Figure 4, bottom) and whose displacement is checked by two optical autocollimators. An X-ray-sensitive CCD camera is located at a distance of 5 m from the optics; it can detect both the direct and the reflected beam. From the position and the shape of the reflected beam, statements concerning the local quality of the reflecting surface can be made, especially with regard to form errors.

Since a focal length of 20 m was planned for the IXO Mission, another positioning possibility of the CCD camera at exactly this distance was realized in 2010. For mirror systems that are designed as a Wolter telescope and contain two reflections, this distance presupposes, at an angle of incidence of up to 1.4°, a vertical translation of the camera of 2 m at a simultaneous inclination of approx. 5.6°.

Even though it was shown from the measurements carried out at a short distance of 5 m that it is possible, under certain conditions, to extrapolate to larger distances [16], a further beamline with a camera distance of approx. 13 m is planned for the ATHENA Mission.

Besides these measurements at the XPBF, mirrors as well as mirror coatings are also investigated in the X-ray range [17]. On the other hand, also detectors (such as DEPFET detectors for the Mercury Mission MIXS [18], pnCCDs for eROSITA [19] or scintillation detectors for the Fermi Gamma telescope [20]) are calibrated.

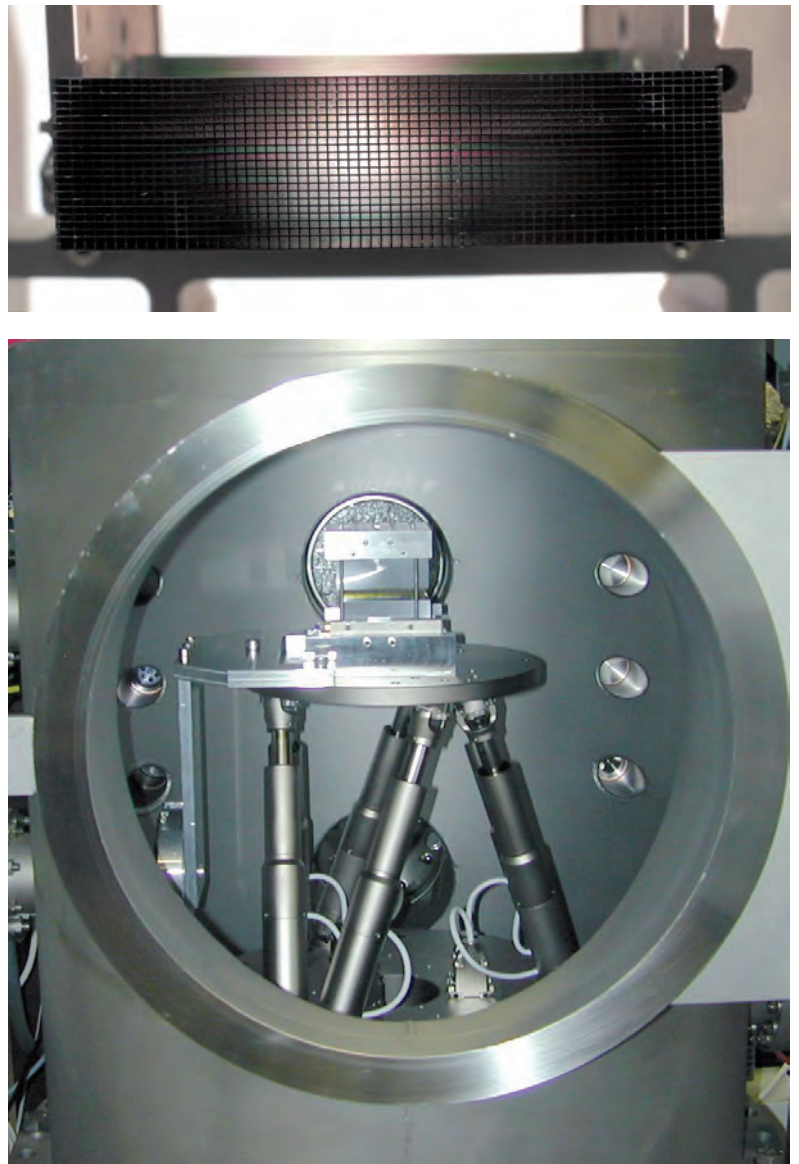


Figure 4.

Top: Silicon pore optics (SPO) consisting of stacked wafers with ribs on their reverse side.

Bottom: SPO on the hexapod of the *X-ray Pencil Beam Facility* (XPBF).

References

- [1] R. Klein, R. Fliegau, S. Kroth, W. Paustian, M. Richter, R. Thornagel: in this publication on p. 16
- [2] A. Gottwald, U. Kroth, M. Krumrey, P. Müller, F. Scholze: in this publication on p. 21
- [3] J. Hollandt, U. Schühle, W. Paustian, W. Curdt, M. Kühne, B. Wende, K. Wilhelm: Appl. Opt. **35**, 5125 (1996)
- [4] A. Fludra et al.: Proc. SPIE **8862**, 88620F (2013)
- [5] J. Hollandt, M. C. E. Huber, M. Kühne: Metrologia **30**, 381 (1993)
- [6] K. Wilhelm, P. Lemaire, U. Feldmann, J. Hollandt, U. Schühle, W. Curdt: Appl. Opt. **36**, 6416 (1997)
- [7] M. Richter, G. Ulm: in this publication on p. 3
- [8] A. BenMoussa et al.: IEEE Trans. Nucl. Sci. **60**, 3907 (2013)
- [9] A. BenMoussa et al.: Diamond & Related Materials **18**, 860 (2009)
- [10] A. BenMoussa et al.: IEEE Trans. Electron Devices **60**, 1701 (2013)
- [11] M. Krumrey, L. Cibik, A. Fischer, A. Gottwald, U. Kroth, F. Scholze: in this publication on p. 35
- [12] S. Serej, E. Kellogg, R. Edgar, F. Scholze, G. Ulm: Proc. SPIE **3765**, 777 (1999)
- [13] L. Strüder et al.: A&A **365**, L18 (2001)
- [14] D. D. M. Ferreira, A. C. Jakobsen, F. E. Christensen, B. Shortt, M. Krumrey, J. Garneaes, R. B. Simons: Proc. SPIE **8443**, 84435E (2012)
- [15] M. Krumrey, L. Cibik, P. Müller, M. Bavdaz, E. Wille, M. Ackermann, M. J. Collon: Proc. SPIE **7732**, 77324O (2010)
- [16] G. Vacanti, M. Ackermann, M. Vervest, M. Collon, R. Gunther, C. Kelly, E. Wille, L. Cibik, M. Krumrey, P. Müller: Proc. SPIE **8861**, 88611K (2013)
- [17] D. H. Lumb, F. E. Christensen, C. P. Jensen, M. Krumrey: Opt. Commun. **279**, 101 (2007)
- [18] P. Majewski et al.: Exp. Astron. **37**, 525 (2014)
- [19] S. Granato, R. Andritschke, J. Elbs, N. Meidinger, L. Strüder, G. Weidenspointner, M. Krumrey, F. Scholze: IEEE Trans. Nucl. Sci. **60**, 3150 (2013)
- [20] E. Bissaldi et al.: Exp. Astron. **24**, 47 (2009)

Reflectometry with Synchrotron Radiation

Michael Krumrey*, Levent Cibik, Andreas Fischer, Alexander Gottwald, Udo Kroth, Frank Scholze

Introduction

High-quality reflection measurements for the characterization of optical components, for layer thickness determination, or for the determination of optical constants of solids and thin layers, are performed for a variety of applications. The objects to be measured may be mirrors or other reflecting objects such as diffraction gratings or crystals, but also (foil) filters whose transmittance often varies with the wavelength by many orders of magnitude. At PTB, reflectometry with synchrotron radiation has a long tradition: the first measurements were already carried out in 1986 at BESSY I [1]. Currently, four reflectometers are operated at the beamlines at PTB's laboratory at BESSY II and at the MLS. This article provides a survey of these devices and of their properties, of the measurement procedures and the achievable measurement uncertainties, and of the different applications of reflectometry in the X-ray, EUV and VUV ranges.

Measuring stations for reflectometry

Reflectometry can be performed on all beamlines for detector calibration [2, 3]. These measuring set-ups provide radiation of high spectral purity which is spatially well defined, without a stray light halo, and with a high temporal stability. In addition, the monochromators have a very good reproducibility of the energy or wavelength setting. As the characterization of optical components often also requires the measurement of position- and angle-dependent properties, the beam size and the beam divergence may become vitally important. For applications in the X-ray region under grazing incidence, a good angular resolution is, therefore, often more important than a particularly good spatial resolution on the samples. This has been especially taken into account for the optical design of the beamlines.

For the characterization of optical components, four reflectometers are available by which the sample to be investigated can be positioned in all degrees of freedom. The essential properties are compiled in Table 1.

* Dr. Michael Krumrey, Working Group "X-ray Radiometry", e-mail: michael.krumrey@ptb.de

Table 1:
Summary of some of the essential properties of PTB's reflectometers.

Instrument	Beamline	Polarization	Max. sample size and mass	Others
VUV reflectometer [6]	NIM MLS	optional	(155 mm) ² 5 kg	Load lock
EUV reflectometer [4]	EUVR MLS	S	550 mm \emptyset 50 kg	Firmly installed at the EUVR beamline
EUV ellipso-scatterometer	SX700 BESSY II	optional	(190 mm) ² 5 kg	Load lock, polarization analyzer
X-ray reflectometer [5]	FCM (PGM) BESSY II	S	(150 mm) ² 5 kg	Load lock, X-ray detector for single-photon counting

Due to its size, the EUV reflectometer [4] is firmly installed on the EUVR beamline at the MLS. The X-ray reflectometer [5] is used on the FCM beamline and at the PGM monochromator of PTB's undulator at BESSY II. The VUV reflectometer [6] can be rotated around the optical axis and allows measurements to be performed with any polarization orientation. It is used at the NIM beamline of the MLS. The new EUV ellipso-scatterometer, which is used on the SX700 beamline, also allows any linear direction of polarization to be selected.

Measurement procedures and uncertainties

In contrast to source calibration or detector calibration, no standards are required for reflectometry, as these measurements are relative measurements of the intensity of the reflected (or, in the case of filters or partially reflecting samples: of the transmitted) beam compared to the intensity of the incident beam, measured with the same photodetector, respectively. But also here, diverse influence quantities must be taken into account in order to achieve lower measurement uncertainties. These are, in the case of incident radiation, the beam divergence and the spectral bandwidth – in addition to the stability and spectral purity, which are also important for detector calibration. For reflectometers, the homogeneity and linearity of the detectors used (mostly semiconductor photodiodes) and the linearity of the associated amperemeters are essential in addition to the accuracy of the angle adjustment. Table 2 provides an overview of the measurement uncertainties which can be achieved at the different beamlines.

Applications

X-ray range

In the X-ray range, the reflectance of mirrors is investigated for applications in astrophysics [7] or plasma diagnosis [8]. In addition, optical components are examined with regard to their use at other synchrotron radiation sources [9]. Currently, reflectometry in the X-ray region is, however, mainly used to determine the thickness of nanolayers which play an important role, e.g., in nanotechnology, in the semiconductor industry, and in the optical industry for the manufacture of mirrors and optical coatings. Thereby, the function of the layer often decisively depends on its thickness. X-ray reflectometry (XRR) is an established non-destructive procedure for layer thickness determination [10]. In a layer-substrate system, reflection occurs both at the surface of the layer and at the layer-substrate interface (as shown in Figure 1). According to Bragg's equation, constructive interference occurs for X-rays – which, in most cases, hit the surface under a grazing angle of incidence – if the path of the radiation in the layer with the thickness d is an integer multiple of the wavelength λ : $m \cdot \lambda = 2 \cdot n \cdot d \cdot \sin \Theta_2$. Here, n is the refractive index of the layer, and Θ_2 is the angle in the layer which differs from the external angle of incidence Θ , by the refraction. The influence is, however, insignificant because – although n is smaller than 1 in the X-ray region – it mostly differs from 1 only by values $< 10^{-4}$. For certain optical constants, a phase shift may also occur at the interface by which the conditions for minima and maxima are reversed.

Table 2:
Summary of typical measurement uncertainties for the determination of the reflectance.

Beamline	NIM	EUVR	SX700	FCM
Storage ring	MLS	MLS	BESSY II	BESSY II
Typical wavelength/ nm	300	13.5	13.5	0.2
Contribution	Contribution to relative standard uncertainty u / %			
Stability of the radiant power	0.14	0.01	0.03	0.01
Angle adjustment and beam divergence	0.01	0.01	0.01	0.20
Homogeneity of the detector	0.06	0.06	0.06	0.20
False light (higher harmonic of the monochromator and stray light)	0.12	0.12	0.12	< 0.01
Relative measurement uncertainty for the reflectance	0.20	0.14	0.14	0.30

In each case, the reflectance shows – at a fixed wavelength as a function of the angle of incidence – characteristic oscillations whose period is used to determine the layer thickness. The traceability of the layer thickness determination – i.e. of a length measurement – is obtained from the wavelength calibration of the monochromator, which can, in turn, be traced back via Bragg's back reflection on a silicon single crystal to the lattice constant of this crystal [11], and from the calibration of the goniometer in the reflectometer by a calibrated optical polygon, using an electronic autocollimator.

Figure 2 shows the experimental realization in the X-ray reflectometer with a very specific sample: a sphere of isotopically pure silicon, 95 mm in diameter, which – via the determination of the Avogadro constant – is intended to serve to redefine the unit "kilogram" [12]. XRR is used to determine the thickness of the unavoidable silicon oxide layer on the sphere surface. On the oxide there is, in addition, also an unavoidable, carbon-containing contamination layer. To separate the two layer thicknesses from each other, the measurements are carried out with focused undulator radiation on the PGM beamline at BESSY II at different energies around the oxygen absorption edge in the range from 480 eV to 560 eV [13]. In this range, the optical properties of the oxide change very strongly, whereas they are largely constant for silicon and for the contamination layer. For these energies, angles of incidence up to 40° can be used. This makes it possible to carry out the measurements on the strongly curved surface. The measured reflectance is shown in Figure 3. The oscillations are very pronounced, in particular close to the absorption edge (529 eV). Although the photon energy changes by only approx. 20 %, the curves are quite varied. From the simultaneous fit, which is also shown [11], a thickness of 7.1 nm is obtained for the oxide, and a thickness of 0.3 nm for the contamination layer. The layers can be distinguished only if measurements are performed at several photon energies (at one single energy, only the total layer thickness can be determined).

The selection of the photon energy offers similar advantages, for example, for Cu- and Ni-double layers on a Si-substrate. Whereas Cu-K α radiation, which is usually used for laboratory X-ray sources, only allows the total thickness to be determined from the angular dependence of the reflectance (Figure 4, top), a measurement at 8400 eV, i.e. at a photon energy between the K absorption edges of Ni (8333 eV) and Cu (8980 eV), exhibits the double structure which is characteristic of double layers (Figure 4, bottom) and from which the single layer thicknesses can be obtained [14].

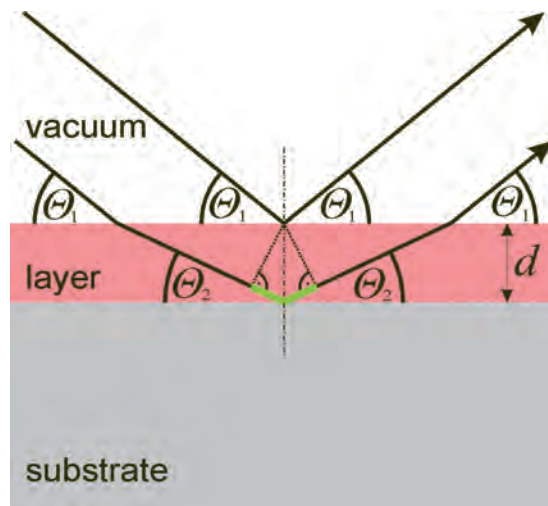


Figure 1: Principle of X-ray reflectometry for layer thickness determination: The path difference of the radiation reflected on the surface and on the interface causes interferences (Figure 3).

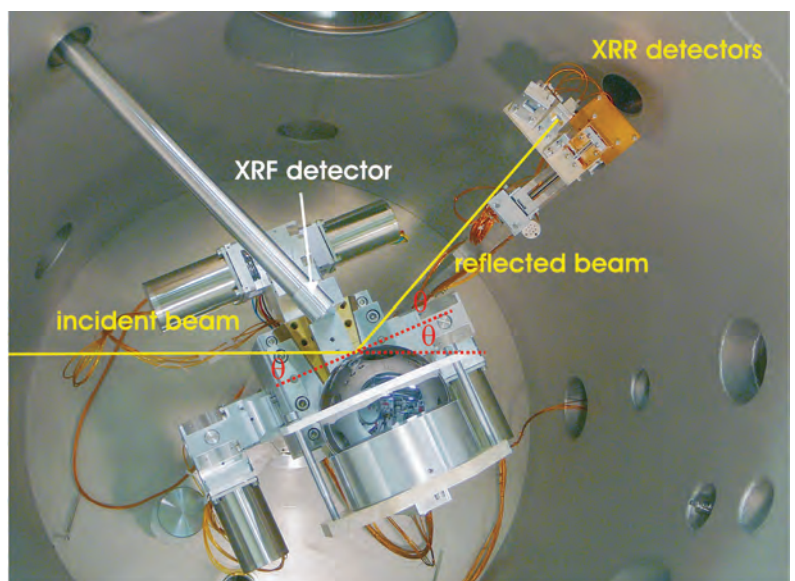


Figure 2: View into the X-ray reflectometer with a sphere used for the determination of the Avogadro constant. If the sample surface is rotated by the angle Θ to the incident beam, the detector arm must be rotated by the angle 2Θ to detect the reflected beam. On the detector arm, the different detectors (photodiodes with and without an entrance slit and a silicon drift detector for photon counting) can be seen.

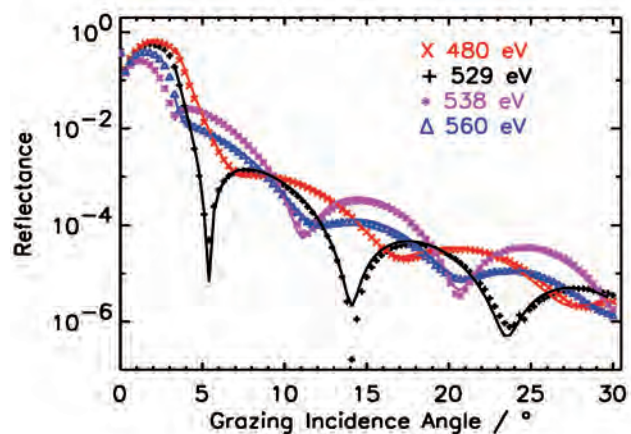


Figure 3: Measured reflectance of a thermally oxidized Avogadro sphere at different photon energies around the oxygen absorption edge, and result of the simultaneous fit.

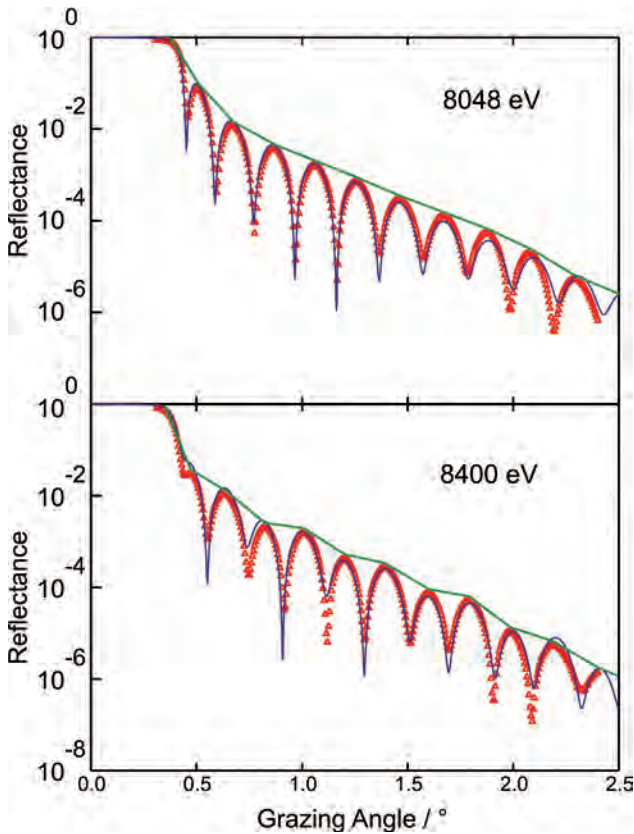


Figure 4: Measured and fitted reflectance of a Cu-Ni double layer on Si. At 8048 eV (top), the optical constants of the two elements hardly differ. The characteristic double structure of a double layer can be seen only at 8400 eV (bottom).

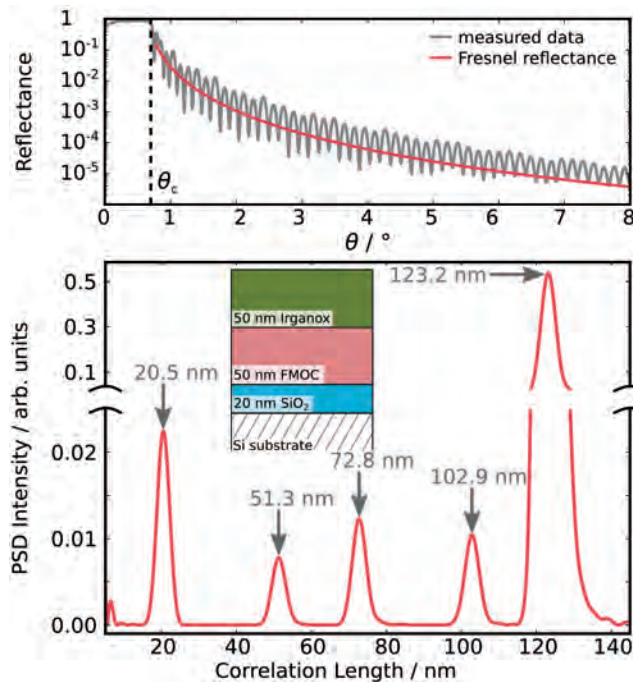


Figure 5: Si wafer with SiO_2 layer and organic double layer: Measured reflectance (top) and Fourier transformation of the oscillatory fraction (bottom). The peaks correspond to the single layers and layer groups; 20.5 nm (SiO_2), 52.3 nm (FMOC) and 50.5 nm (Irganox 1010) are obtained as single thicknesses.

For the layer thickness determination of organic layers on oxidized silicon wafers – as well as for SiO_2 layers on plane surfaces – a photon energy of 1841 eV (i.e. directly above the Si-K absorption edge) is suitable, as the contrast of the optical constants of Si and SiO_2 is particularly high here due to the shift of the edge in the oxide [15, 16]. For complex systems, the evaluation can also be performed via a Fourier transformation of the oscillatory fraction of the measured reflectance clearly above the critical angle for the total reflection (Figure 5, top). The visible peaks in Figure 5 (bottom) correspond to the thickness of single layers or layer groups. The peak at the largest correlation length corresponds to the total layer thickness. The combination of the maxima allows the individual layer thicknesses to be determined [17].

All in all, X-ray reflectometry offers the possibility to determine layer thicknesses in the nanometer range with relative uncertainties down to approx. 1 %. By the use of monochromatized synchrotron radiation, this is also possible for layer combinations for which a sufficient contrast cannot be observed with conventional X-ray sources.

EUV range

For many years, the main field of work in the EUV range at PTB has been the characterization of optical components and detectors for EUV lithography. These activities are shown in a separate article in this publication [18]. Quite generally, short-wave radiation, however, also offers manifold application possibilities for the characterization of micro- and nanostructures. This application, too, will be presented in more detail in another article of this publication [19]. In principle, the measurements which can be performed in the EUV spectral range are the same as those which can be performed with hard X-rays. The critical angles for the reflection are, however, larger and it is, thus, possible to carry out measurements at steeper angles of incidence. This is, for example, of advantage for curved surfaces – as in the case of the above-mentioned silicon sphere – or smaller samples. A further particularity of the spectral range of EUV and soft X-ray is that – although the reflectance is practically negligibly small for all materials under normal incidence – the reflectance in the maximum of the resonance can, due to the structure of multi-layer Bragg reflectors, amount to clearly more than 50 %. This allows mirror-optical systems with a large numerical aperture and a large field of view to be established, similar to the UV or VUV range. The most important application is EUV lithography for the semiconductor industry at a wavelength of 13.5 nm [18]. There are, however, also multi-layer systems which have

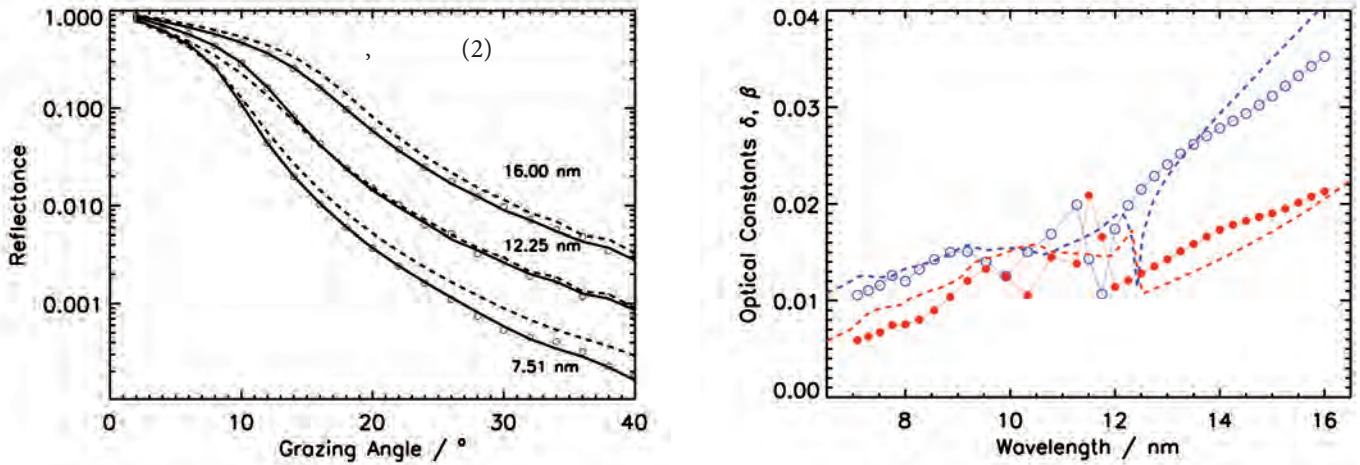


Figure 6: The optical constants δ and β of SiO_2 (refractive index $n = 1 - \delta + i\beta$) in the spectral range from 7 nm to 16 nm determined from the reflectance R_s as a function of the angle of incidence θ_1 to the surface. On the left, some measurement curves are shown which have been obtained at different wavelengths and from which the values shown on the right for δ (blue circles) and β (red points) have been determined for each single wavelength. For comparison, tabulated data from literature [19] are shown. The dashed and the solid lines in the left figure represent adaptations of the measurement points with the old and new optical constants.

been optimized for reflection at shorter wavelengths, for example at 3 nm in the so-called “water window” between the absorption edges of carbon and oxygen. In this spectral range, organic substances can very well be investigated in an aqueous environment and can, for example, be imaged microscopically with high resolution. For optimization of the respective optics based on layer systems, their optical material properties must be investigated. This can be done by measuring the angle-dependent reflectance, making use of the Fresnel equations. The refractive index in its complex form $n = 1 - \delta + i\beta$ allows the formulas to be uniformly represented also for absorbing media – by recursive application also for multi-layers. For S- or P-polarized radiation, which occurs from the vacuum under the angle θ_1 to the surface (for angles which are defined in a complex manner), the reflectance R of a thick layer can be calculated according to:

$$R_s = \left| \frac{\sin\theta_1 - (1 - \delta + i\beta)\sin\theta_2}{\sin\theta_1 + (1 - \delta + i\beta)\sin\theta_2} \right|^2 \quad (1)$$

$$R_p = \left| \frac{(1 - \delta + i\beta)\sin\theta_1 - \sin\theta_2}{\sin\theta_1 + (1 - \delta + i\beta)\sin\theta_2} \right|^2, \quad (2)$$

with θ_2 being the angle of the layer which can be calculated in its complex form using the law of refraction according to [20]:

$$\cos\theta_2 = \frac{\cos\theta_1}{1 - \delta + i\beta} \quad (3)$$

Figure 6 shows an example of the determination of the optical constants from angle-dependent reflection measurements for a thick SiO_2 layer (see the clear deviations of the measured optical constants in the spectral range from 7 nm to 16 nm from the generally used tabulated values [21]).

Another application of reflectometry in the EUV range is shown in Figure 7. Here, the specular reflection was measured on a grating structure with a rectangular line profile [22]. The interference of the partial waves reflected on the surfaces of the lines and on the bases of the grooves leads, as described above for the reflection of a homogeneous layer, to an interference effect which, in this case, allows the line height to be determined.

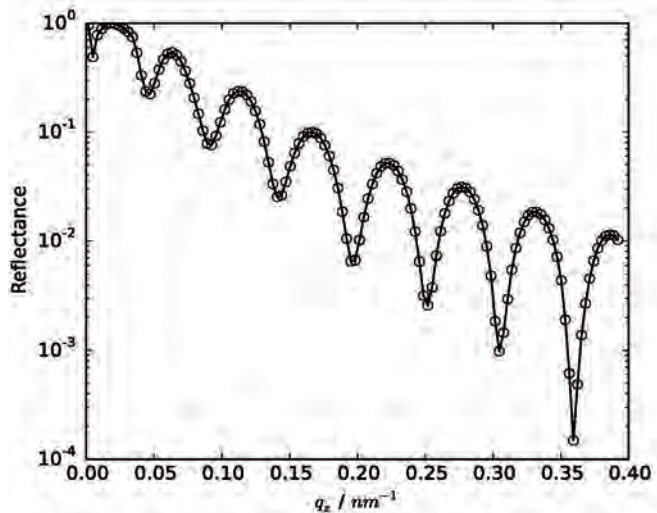


Figure 7: Reflectance of an etched silicon grating as a function of the angle of incidence at 13.5 nm. From the oscillations, a line height of 114 nm can be determined.

UV/VUV range

In the range of UV and vacuum-UV (VUV) radiation, i.e. in the wavelength interval between 40 nm and 400 nm, optical components (e.g. mirrors, filters, dispersion lattices) are also investigated routinely with reflection and transmission measurements at the normal incidence monochromator (NIM) set-up for detector calibration [2, 3]. The reflecting layer is, in most cases, metallic. Metal carbides or dielectric layers for wavelength-selective reflection or anti-reflection coatings (AR coatings) are, however, also used.

In particular in the VUV spectral range, i.e. for wavelengths below 200 nm, the depth of penetration of the radiation is very small (only a few 10 nanometers or less, depending on the wavelength and on the material) so that the optical properties are predominantly determined by the quality of the immediate surface. Depth profiles and multi-layer systems are, however, of subordinate importance (unlike in the regions of shorter wavelengths). In addition to the direct determination of the reflectance for applications or for reference mirrors, the curve of the spectral reflectance or transmittance also provides data for the determination of the optical constants of solids or thin layers [23]. Fundamental investigations of the electronic states (band gaps) of a solid can also be performed, whereby the variation of the temperature during the measurement provides, for example, information about the origin of the different absorption and reflection processes [24, 25]. The possibility of measuring the polarization-dependent reflectance as a function of the angle of incidence allows polarizing optical elements to be

investigated and developed in a dedicated way. An example are polarization mirrors for the hydrogen-Lyman- α -wavelength at 121.6 nm, which are of outstanding importance in stellar astrophysics (Figure 8) [26].

The polarization P is calculated as follows:

$$P = \frac{R_s - R_p}{R_s + R_p} \quad (4).$$

The measurement requires a previous determination of the polarization degree of the monochromatized synchrotron radiation. These techniques also provide the basis for VUV ellipsometry [27, 28], in which case the change in the polarization during reflection is measured in order to determine layer thicknesses and material properties.

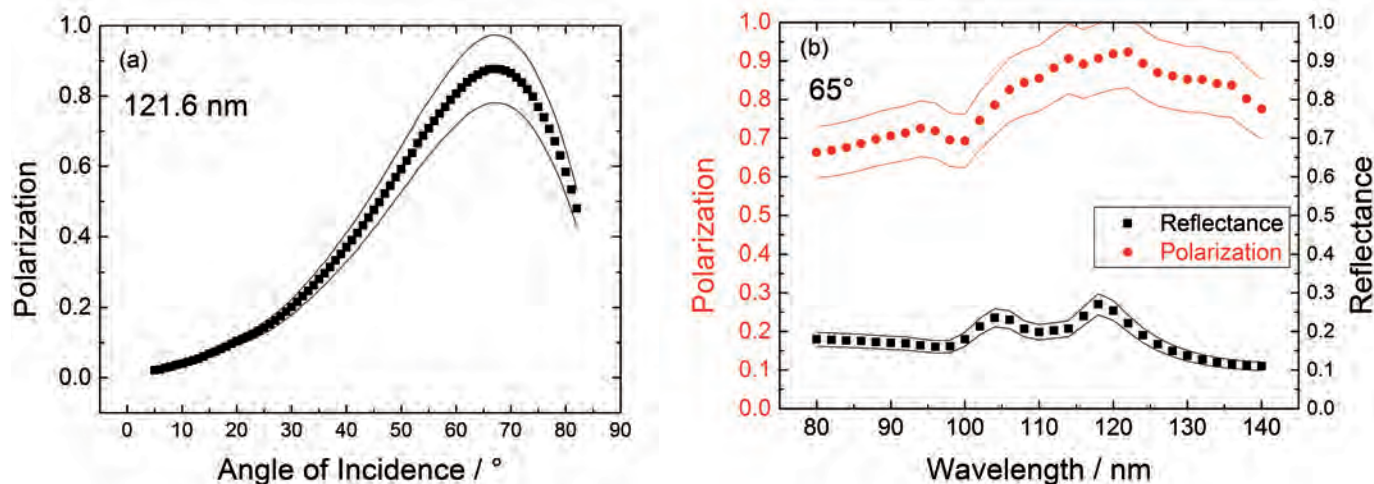


Figure 8:

Measured properties of an MgF_2 reflection polarizer.

a) Polarization for the hydrogen-Lyman- α -wavelength of 121.6 nm as a function of the angle of incidence.

b) Reflectance and polarization in the wavelength range between 80 nm and 140 nm. The lines indicate the range of the standard uncertainty.

References

- [1] M. Kühne, K. Danzmann, P. Müller, B. Wende: Proc. SPIE **688**, 76 (1986)
- [2] M. Richter, G. Ulm: in this publication on p. 3
- [3] B. Beckhoff, A. Gottwald, R. Klein, M. Krumrey, R. Müller, M. Richter, F. Scholze, R. Thornagel, G. Ulm: Phys. Status Solidi B **246**, 1415 (2009)
- [4] J. Tümmler, F. Scholze, G. Brandt, B. Meyer, F. Scholz, K. Vogel, G. Ulm, M. Poier, U. Klein, W. Diete: Proc. SPIE **4688**, 338 (2002)
- [5] D. Fuchs, M. Krumrey, P. Müller, F. Scholze, G. Ulm: Rev. Sci. Instrum. **66**, 2248 (1995)
- [6] M. Krumrey, M. Kühne, P. Müller, F. Scholze: Proc. SPIE **1547**, 136 (1991)
- [7] D. H. Lumb, F. E. Christensen, C. P. Jensen, M. Krumrey: Opt. Commun. **279**, 101 (2007)
- [8] P. Troussel, B. Villette, B. Emprin, G. Oudot, F. Bridou, F. Delmotte, M. Krumrey: Rev. Sci. Instrum. **85**, 013503 (2014)
- [9] F. Choueikani, B. Lagarde, F. Delmotte, M. Krumrey, F. Bridou, M. Thomasset, E. Meltchakov, F. Polack: Opt. Lett. **39**, 2141 (2014)
- [10] P. Colombi et al.: J. Appl. Cryst. **41**, 143 (2008)
- [11] M. Krumrey, G. Gleber, F. Scholze, J. Wernecke: Meas. Sci. Technol. **22**, 094032 (2011)
- [12] B. Andreas et al.: Phys. Rev. Lett. **106**, 030801 (2011)
- [13] I. Busch, Y. Azuma, H. Bettin, L. Cibik, P. Fuchs, K. Fujii, M. Krumrey, U. Kuetgens, N. Kuramoto, S. Mizushima: Metrologia **48**, S62 (2011)
- [14] M. Kolbe, B. Beckhoff, M. Krumrey, G. Ulm: Spectrochim. Acta B. **60**, 505 (2005)
- [15] M. Krumrey, M. Hoffmann, G. Ulm, K. Hasche, P. Thomsen-Schmidt: Thin Solid Films **459**, 241 (2004)
- [16] M. P. Seah et al.: Surf. Interface Anal. **36**, 1269 (2004)
- [17] J. Wernecke, A. G. Shard, M. Krumrey: Surf. Interface Anal. **46**, 911 (2014)
- [18] F. Scholze, C. Laubis, A. Barboutis, C. Buchholz, A. Fischer, J. Puls, C. Stadelhoff: in this publication on p. 43
- [19] F. Scholze, A. Haase, M. Krumrey, V. Soltwisch, J. Wernecke: in this publication on p. 48
- [20] E. D. Palik (Eds): Handbook of Optical Constants of Solids, Academic Press, Orlando (1985)
- [21] B. L. Henke, E. M. Gullikson, J. C. Davis: Atomic Data and Nuclear Data Tables **54**, 181 (1993)
- [22] V. Soltwisch, J. Wernecke, A. Haase, J. Probst, M. Schoengen, M. Krumrey, F. Scholze: Proc. SPIE **9050**, 905012 (2014)
- [23] F. Bridou, M. Cuniot-Ponsard, J.-M. Desvignes, A. Gottwald, U. Kroth, M. Richter: Appl. Phys. A **102**, 641 (2011)
- [24] M. Letz, A. Gottwald, M. Richter, V. Libermann, L. Parthier: Phys. Rev. B **81**, 155109 (2010)
- [25] M. Letz, A. Gottwald, M. Richter, L. Parthier: Phys. Rev. B **79**, 195112 (2009)
- [26] F. Bridou, M. Cuniot-Ponsard, J.-M. Desvignes, M. Richter, U. Kroth, A. Gottwald: Opt. Commun. **283**, 1351 (2010)
- [27] M. Kolbe, E. Darlatt, A. Gottwald, H. Kaser, M. Richter: in this publication on p. 69
- [28] M. D. Neumann, C. Cobet, H. Kaser, M. Kolbe, A. Gottwald, M. Richter, N. Esser: Rev. Sci. Instrum. **85**, 055117 (2014)

Radiometry for EUV Lithography

Frank Scholze*, Christian Laubis, Annett Barboutis,
Christian Buchholz, Andreas Fischer, Jana Puls, Christian Stadelhoff

An essential step in the production of integrated circuits is the structuring of semiconductor wafers for the tracks of the printed circuit boards and transistors. For this purpose, photolithography is applied whose resolution is limited by the optical wavelength. The – currently used – wavelength of an ArF laser of 193 nm is too long to manufacture the small structures which will, in future, be required in a single exposure process. According to the roadmap of the semiconductor manufacturers, extreme ultraviolet (EUV) radiation at a wavelength of 13.5 nm is to be used in future for lithography in chip production with linewidths smaller than 10 nm [1, 2]. The main components of an EUV lithography machine are a powerful EUV plasma radiation source, an illumination system, the reflection mask, and a projection optics which projects a demagnified image of the mask onto the wafer. All these components have specifications which are deemed a technological challenge and which require comprehensive new and further developments. At the same time, the measurement technologies used have to keep pace with developments, especially at the working wavelength around 13 nm (the so-called "at wavelength"). Since there were no suitable EUV radiation sources available for the development of high-accuracy measurement techniques, this "at-wavelength metrology" was, at first, performed worldwide with synchrotron radiation at electron storage rings – in the USA, in particular at the *Center for X-Ray Optics (CXRO)* at the *Advanced Light Source (ALS)* in Berkeley [3] and at NIST in Gaithersburg at the storage ring SURF III [4, 5], and in Europe at PTB in Berlin with its EUV beamlines at the storage rings BESSY I (formerly), BESSY II (currently) and, since October 2013, also at the *Metrology Light Source (MLS)* [6].

EUV Reflectometry

Reflectometry [7] is the main method used at PTB for the "at-wavelength investigation" of components for EUV lithography. In addition to developing powerful EUV radiation sources, the manufacturing of suitable optical components is a great challenge. There are no materials which are transparent for EUV radiation. Therefore, only mirrors can be used as optical components. By using periodic multilayer coatings as Bragg reflectors, a sufficient reflectivity can hereby be attained. The properties of these Mo/Si multilayer coatings must, however, be determined at the working wavelength since – due to the conversion to the working wavelength which would, otherwise, be required – unacceptable uncertainties would arise as a result of the numerical models and material parameters used.

* Dr. Frank Scholze,
Working Group "EUV
Radiometry", e-mail:
frank.scholze@ptb.
de

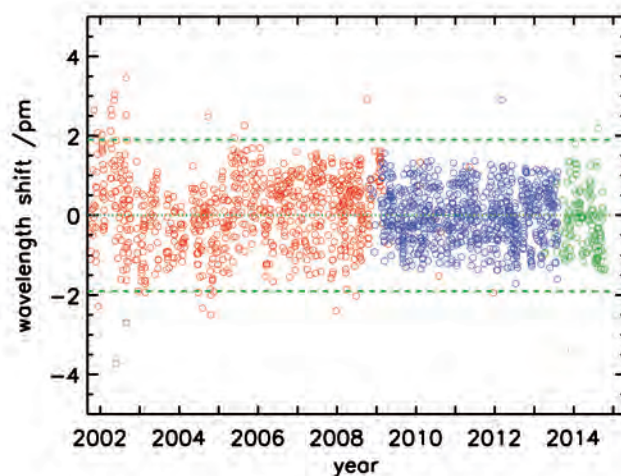


Figure 1:
Results of the daily check of the wavelength by measurement of the Be-K-(red) or the Si-L-(blue) absorption edge at the SX700 beamline. Due to its better stability, Si has been used since 2009 as the reference edge; since September 2013, at the EUVR beamline of the MLS (green).

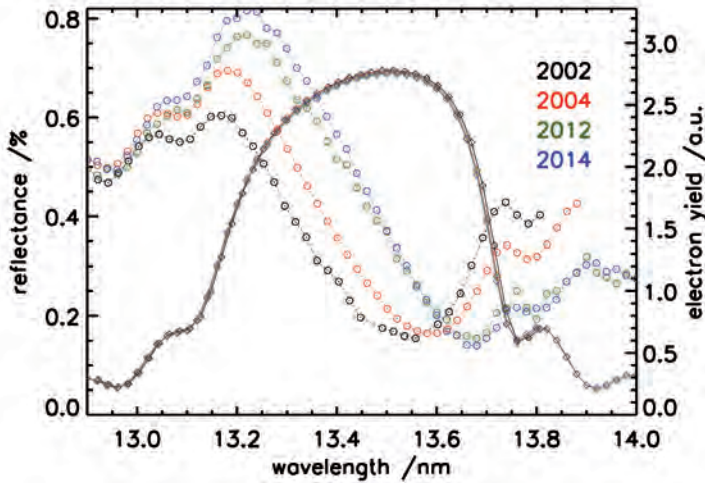


Figure 2: Repeated measurement of the reflectivity of a mirror with 60 Mo/B₄C/Si/C layers (diamonds, left-hand scale). The photoelectric current of the mirror surface (circles, right-hand scale) was also measured. The phase shift of the signal corresponds to an increase in thickness of the surface layer due to carbon contamination of approx. 1.0 nm.

What is particularly important for technological development is the reproducibility of the measurements over long periods of time to be able to safely demonstrate, on the one hand, the asymptotically increasingly smaller progress achieved by the technology and, on the other hand, the long-term stability of the components. The measurement reproducibility of the reflectivity and of the wavelength is therefore continuously checked. Figure 1 shows the wavelength of the absorption edge of a spectral filter [8] which has been measured on a daily basis over a period of more than 10 years for checking purposes in the EUV reflectometer [7] at the SX700 beamline at BESSY II [6, 9] and, from September 2013, at the EUVR beamline at the MLS [6]. The dispersion of the values over longer periods of time results from minimum adjustment losses of the optical beamline components due to, e.g., thermal effects and the settling of the building. For the reproducibility, a tolerance range of 2 pm was defined for the wavelength [10] (green dashed line in Figure 1). When the tolerance is exceeded, the monochromator is re-adjusted.

The reproducibility of the measurements is also checked on a regular basis by means of a group of reference mirrors, whose reflectivity and central wavelength are measured. This allows not only changes in the beamline, but also, for example, possible adjustment deviations or influences due to ageing of the photodetector to be detected in the reflectometer. In order to comply with the Bragg condition for 13.5 nm, the thickness of a double layer of Mo and Si must be approx. 7 nm. These very thin layers are thermodynamically unstable and can lead, for example, to molybdenum silicide formation. This causes the mean density to increase, and the thickness of the double layers to decrease, which is considerably accelerated at increased temperatures. For this reason, further intermediate layers are added as diffusion barriers for thermal stabilization. Figure 2 shows measurements of the reflectivity of a mirror with a diffusion-stabilized Mo/Si multilayer system (60 × Mo/B₄C/Si/C) over a period of time of more than 10 years. The changes in the reflectivity and wavelength lie at the detection limit. The photoelectric current of the mirror surface, however, exhibits a clear change. It is correlated with the electric field intensity at the surface of the mirror. Presuming a fixed spatial correlation between the reflected wave train and the multilayer system, this change can only have been caused by a special shift of the surface in relation to the stationary wave field. In this case, this is due to the growth of a carbon contamination layer of approx. 1.0 nm thickness. This shows that the slight change in the reflectivity is clearly due to a slight modification of the sample, and not to measurement errors. This simultaneous measurement of both the reflectivity and the photoelectric current,

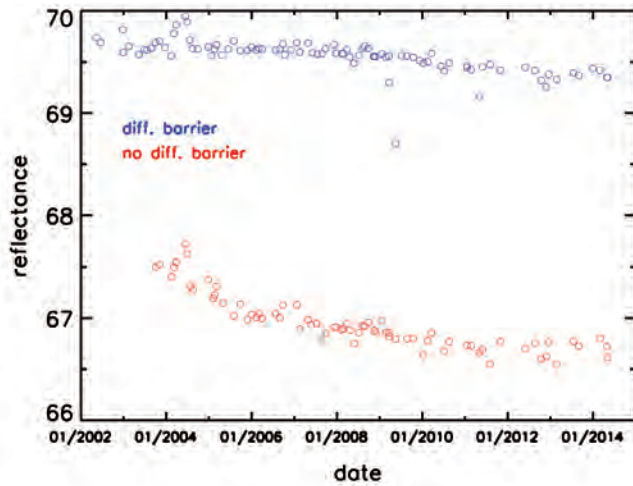


Figure 3: Reflectance measured on two EUV mirrors over a period of 12 years (blue: mirror with diffusion barriers; red: mirror without diffusion barrier).

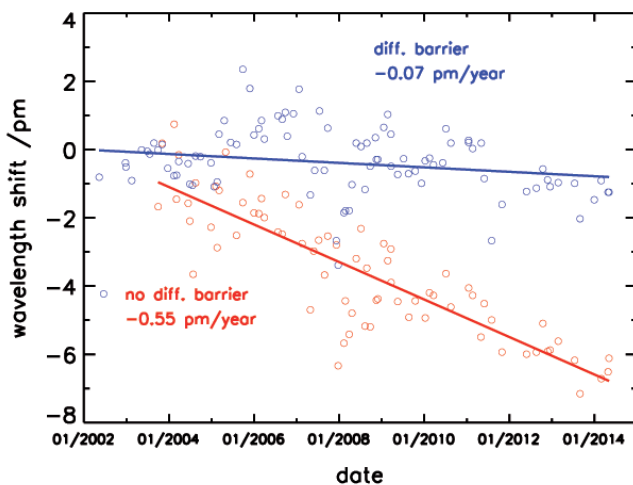


Figure 4: Measured shift of the central wavelength measured on two EUV mirrors over a period of 12 years (blue: mirror with diffusion barriers; red: mirror without diffusion barrier).

which was developed at PTB, provides particularly detailed data on minimum changes in the surface state of mirrors which would not be detectable using other methods [11]. In August 2013, the EUV reflectometer [7] moved from the SX700 beamline at BESSY II to the EUVR beamline at the MLS [6]. The good agreement between the measurement from 2014 shown in Figure 2 and the previous ones confirms the good reproducibility, even after the move.

The results obtained with two typical EUV mirrors over a period of time of more than 10 years are shown in Figures 3 and 4. Although the changes measured lie at the detection limit, clear trends become visible. The two mirrors differ from each other by the lack/presence of a diffusion barrier between the Si- and the Mo-layers. In both cases, the reflectivity exhibits a clearly visible downward trend which is, here too, explained by the slow growth of a surface contamination layer. The mirror without a diffusion barrier, however, exhibits – especially at the beginning – a clearly stronger decrease, which suggests a reduction in the optical contrast at the layer interfaces due to the diffusion processes.

The reproducible setting of the wavelength (Figure 1) allows the behavior of EUV mirrors to be checked over long periods of time. Figure 4 shows the shift of the central wavelength for the two above-mentioned EUV mirrors. In the case of the mirror with the diffusion-stabilized multilayer, the central wavelength remains constant over the total period, whereas it – slightly, but clearly – decreases in the case of the mirror without a diffusion barrier. Besides measurement stability over long periods of time, these results simultaneously prove that PTB's measurement uncertainties are sufficient to detect even very small changes over long periods of time. This is an important precondition for lifetime tests as are carried out on the basis of measurements performed by PTB [12].

By commissioning the EUVR beamline at the MLS, PTB has now two beamlines for the EUV spectral range at its disposal [6]. The measuring instruments – the EUV reflectometer at the EUVR beamline of the MLS, and the EUV ellipso-scatterometer at the SX700 beamline at BESSY II [7] – are depicted in Figure 5. Figure 6 shows, as a typical sample for EUV lithography (EUVL), a collector mirror for an EUV laser plasma source with a diameter of 670 mm, mounted in the EUV reflectometer. Figure 7 shows the results of a measurement of the reflectivity of such a mirror across the total optical surface.

An important parameter for the characterization of the collectors for the plasma sources is the polarization state of the incident radiation. The plasma radiation sources emit unpolarized radiation, whereas measurements at PTB are carried out with highly polarized radiation. With the new

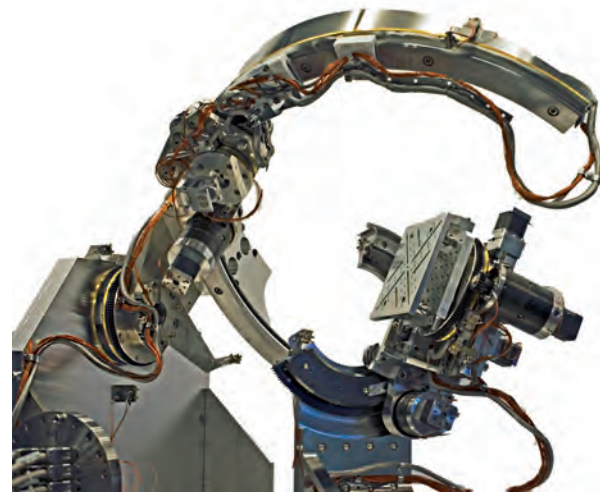


Figure 5: Measuring instruments for EUV reflectometry: EUV reflectometer with cleanroom environment at the EUVR beamline of the MLS (top), mechanism for sample manipulation and detector displacement of the new EUV ellipso-scatterometer at the SX700 beamline at BESSY II (bottom).

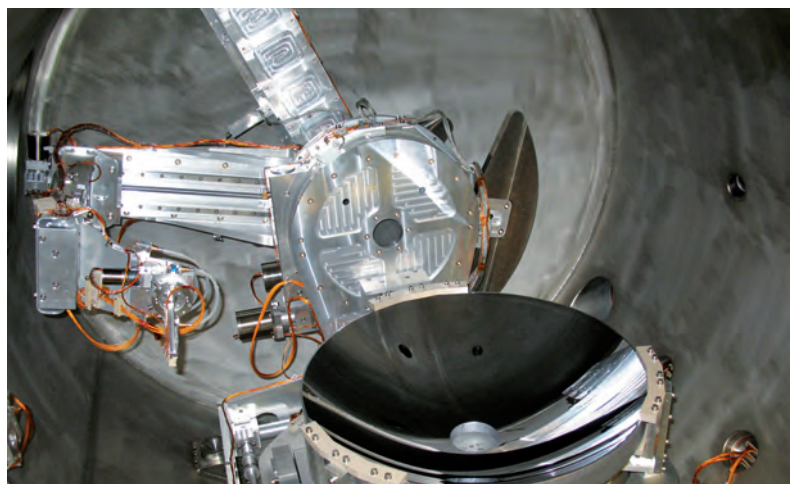


Figure 6: Collector mirror for an EUV plasma source, mounted on the sample goniometer inside the EUV reflectometer (with the kind permission of Fraunhofer IOF and CYMER).

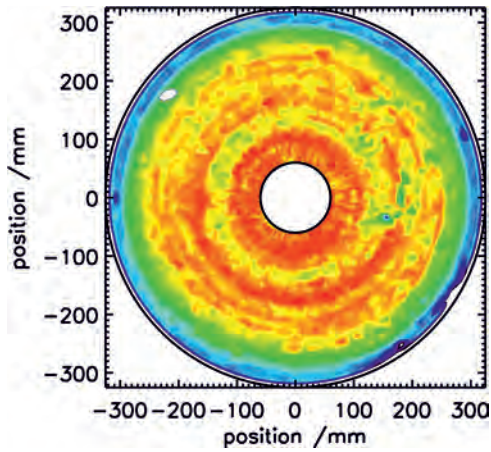


Figure 7: Example of the measurement result at 13.5 nm for a collector surface with a color scale for the reflectivity from 50 % (dark blue) in steps of 0.1 % up to 55.5 % (red).

ellipso-scatterometer, it is possible to take this into account and to carry out the measurement with high resolution for polarization, similar to the VUV range [7]. Especially the range of the so-called "Brewster's angle", on which the reflection for P polarization is suppressed, is now accessible. The detector used for this purpose is a linear Brewster polarization analyzer [13]. With this set-up, a suppression ratio of 10^4 was measured for the P-oriented component at the Brewster angle of a Mo/Si multilayer mirror (Figure 8). This kind of investigation also makes the optical constants of buried layers accessible.

EUV Detectors

Another important working area to support EUV technologies is the characterization of radiation detectors [14]. When using detectors, it is, in particular, important to know their stability under irradiation and under storage conditions, as well as their sensitivity. PTB has been carrying out numerous investigations in this field for a long time [15]. A major problem is that there are only very few commercially available EUV-stable photodetectors. In a joint project realized together with partners from industry and research, the commercially available detectors were therefore systematically investigated and new variants were developed. PTB participated in these activities through measurements of the spectral responsivity in the VUV and in the EUV ranges as well as through exhaustive investigations of the detector stability [16]. Figure 9 shows typical responsivities of corresponding photodiodes. The new "PureB diodes" [17], developed at TU Delft, are very close to the ideal responsivity and are also stable under irradiation [18].

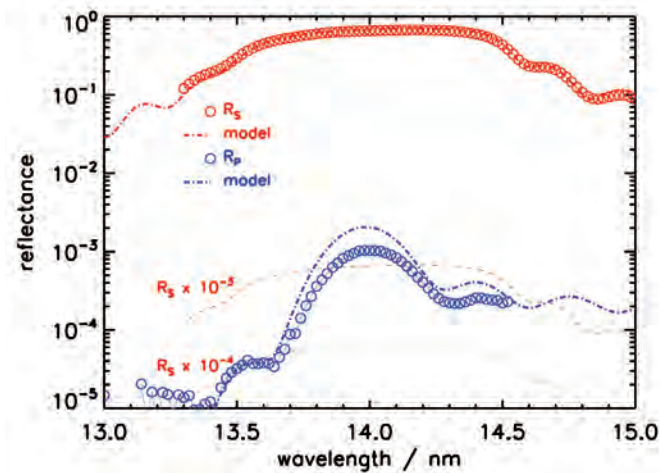


Figure 8: S and P reflectivity of an EUV mirror around Brewster's angle. For comparison purposes, computed values are shown. The structure parameters were adjusted to the reflectivity measured for S polarization.

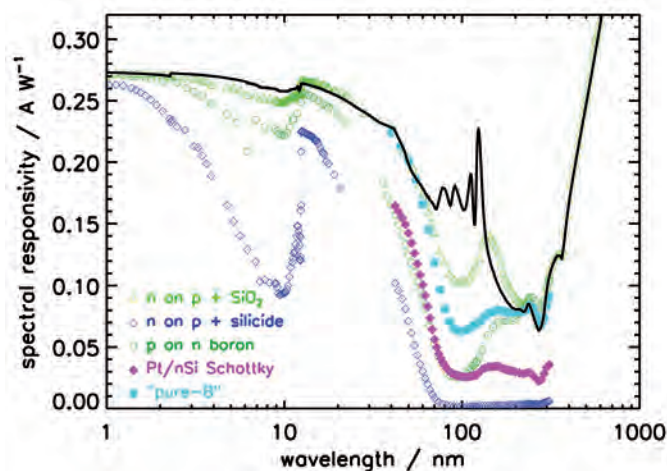


Figure 9: Spectral responsivity of various photodiodes in the range of soft X-ray radiation as well as in the EUV and the VUV ranges. The black curve shows a model computation for an ideal diode.

References

- [1] *P. Gargini*: Proc. SPIE **4688**, 25 (2002)
- [2] https://en.wikipedia.org/wiki/International_Technology_Roadmap_for_Semiconductors (retrieved: 2016-07-01)
- [3] *E. M. Gullikson, S. Mrowka, B. B. Kaufmann*: Proc. SPIE **4343**, 363 (2001)
- [4] *C. Tarrío, R. E. Vest, S. Grantham*: Proc. SPIE **4450**, 94 (2001)
- [5] *S. Grantham, C. Tarrío, M. B. Squires, T. B. Lucatorto*: Proc. SPIE **4688**, 348 (2001)
- [6] *M. Richter, G. Ulm*: in this publication on p. 3
- [7] *M. Krumrey, L. Cibik, A. Fischer, A. Gottwald, U. Kroth, F. Scholze*: in this publication on p. 35
- [8] *F. Scholze, J. Tümmler, G. Ulm*: Metrologia **40**, S224 (2003)
- [9] *F. Scholze et al.*: Proc. SPIE **4344**, 402 (2001)
- [10] *C. Laubis, A. Kampe, C. Buchholz, A. Fischer, J. Puls, C. Stadelhoff, F. Scholze*: Proc. SPIE **7636**, 76362R (2010)
- [11] *M. Wedowski, F. Scholze, J. Tuemmler*: Method For Manufacturing Reflective Optical Element, Reflective Optical Elements, Euv-Lithography Apparatus And Methods For Operating Optical Elements And Euv-Lithography Apparatus, Methods For Determining The Phase Shift, Methods For Determining The Layer Thickness, And Apparatuses For Carrying Out The Methods, Patent US20070285643 (2007)
- [12] *R.-M. Klein, A. Gottwald, F. Scholze, R. Thornagel, J. Tümmler, G. Ulm, M. Wedowski, F. Stietz, B. Mertens, N. B. Koster*: Proc. SPIE **4506**, 105 (2001)
- [13] http://www.ipfdd.de/fileadmin/user_upload/ax/OEA/8th_Workshop_Ellipsometry/Scholze.pdf (retrieved: 2016-06-22)
- [14] *A. Gottwald, U. Kroth, M. Krumrey, P. Müller, F. Scholze*: in this publication on p. 21
- [15] *F. Scholze, R. Klein, T. Bock*: Appl. Opt. **42**, 5621 (2003)
- [16] *L. Shi, S. Nihtianov, S. Xia, L. K. Nanver, A. Gottwald, F. Scholze*: IEEE Trans. Instrum. Meas. **61**, 1268 (2012)
- [17] *F. Sarubbi, L. K. Nanver, T. L. M. Scholtes, S. N. Nihtianov, F. Scholze*: Proc. of 38th European Solid-State Device Research Conference (ESSDERC 2008), Edinburgh, Scotland, UK, p. 278 (2008)
- [18] *L. Shi, S. N. Nihtianov, F. Scholze, L.K. Nanver*: Proc. 38th Annual Conference on IEEE Industrial Electronics Society (IEEE IECON12), Montreal, Canada, p. 3952 (2012)

Investigation of Nanostructured Surfaces by Scattering Procedures

Frank Scholze*, Anton Haase, Michael Krumrey, Victor Soltwisch, Jan Wernecke

* Dr. Frank Scholze,
Working Group
"EUV Radiometry",
e-mail:
frank.scholze@
ptb.de

Introduction

Due to their short wavelength (a few nanometers to approx. 0.1 nm), EUV radiation and X-rays are well suited to investigate structures with dimensions in the nanometer range. In many fields of technology, in particular in semiconductor industry, these structures are gaining in importance. Modern computer chips are very complex 3D structures, with typical dimensions of the electronic single components in the range of a few 10 nm. Nanostructured surfaces are also increasingly used for many other applications such as, for example, anti-reflective layers for solar cells or for biologically and chemically active surfaces. Due to its resolution, which is limited by the wavelength of the light used, optical microscopy is no longer sufficient to characterize these surfaces. Although scanning microscopy techniques such as *Atomic Force Microscopy* (AFM) and *Scanning Electron Microscopy* (SEM) reach the required resolution,

they are very slow and only able to investigate small areas. An alternative is the measurement via the scattering of short-wavelength radiation which allows – as in the case of *Small-Angle X-ray Scattering* (SAXS) on nanoparticles [1] – information on the ensemble characteristics of the scattering objects to be retrieved. The essential difference is that for the investigation of surfaces, the beam cannot be used in forward direction, as it is absorbed in the substrate. Instead, the reflected beam is observed. Due to the fact that in the X-ray region, the radiation is reflected only under *Grazing Incidence* (GI), this procedure is referred to as *GISAXS*. In the EUV range, the radiation on suitable structures is, however, also reflected at almost vertical incidence, a fact which is exploited in the so-called *EUV scatterometry*.

Measuring set-ups

GISAXS measurements can be carried out on the FCM beamline in PTB's laboratory at BESSY II, whereas the SX700 beamline is suited for EUV scatterometry [2]. These two beamlines provide radiation with a very small divergence on the sample. For the positioning of the sample, reflectometers are used [3]. At the FCM beamline, the scattered radiation is measured with a CCD-based detector or, meanwhile, mostly with the large-area, vacuum-compatible hybrid-pixel detector PILATUS 1M [1]. At the EUV beamline, either a CCD sensor is used for the region of very small scattering angles or very low scattering intensities, or the photodiode of the reflectometer [3].

Measurement method

The measurement geometry is shown in Figure 1. Here, the coordinates for the scattering vector q are related to the surface of the sample which is oriented under grazing incidence. Thus, the fol-

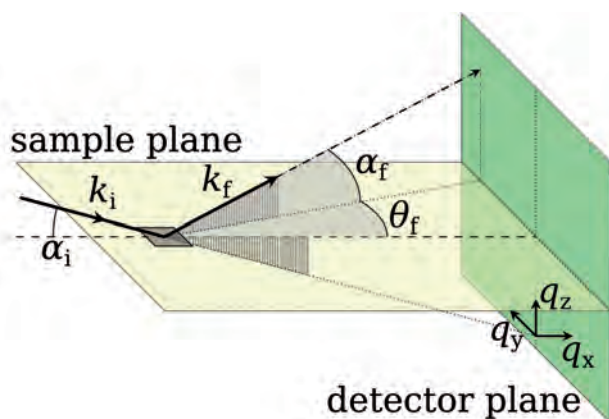


Figure 1: Geometrical scheme of a GISAXS measurement. The radiation hits the surface under grazing incidence and the scattered radiation is measured with an area detector vertical to the sample surface.

lowing relations are obtained:

$$q_x = k_0 (\cos\theta_f \cos\alpha_f - \cos\alpha)$$

$$q_y = k_0 \sin\theta_f \cos\alpha_f$$

$$q_z = k_0 (\sin\alpha_i + \sin\alpha_f) \text{ with: } k_0 = \frac{2\pi}{\lambda} = |\mathbf{k}_i| = |\mathbf{k}_f|$$

with λ being the wavelength and \mathbf{k}_i and \mathbf{k}_f the wave vectors for the incident and scattered radiation, respectively. As shown in the article which deals with the size determination of nanoparticles with small-angle X-ray scattering [1], the measurements performed as a function of the scattering angle and, thus, of the momentum transfer – i.e. in the so-called *reciprocal space* – can be used to draw conclusions as to dimensional quantities from real space. In the case of a sufficiently small wavelength or of sufficiently large periodic structures, one obtains a great number of diffraction orders, from which the dimensions of the structures in real space can be directly determined with the aid of Fourier transformation. This is, however, only possible if the surface can be described with an effective two-dimensional model. For more complicated 3D structures, model calculations (for example: solving of the Maxwell equations for the geometry to be determined, and iterative adaptation of the calculated diffraction intensities to the measured diffraction intensities) are required for the determination of the structure parameters.

Applications

Investigation of lamellar diffraction gratings

The procedure can be well presented by the example of grating structures. The geometry

preferred for the characterization of gratings with GISAXS is the parallel orientation of incident radiation and grating lines. The periodicity of the grating then entails that the wave vector of the scattered radiation \mathbf{k}_f ends on one of the planes at a periodic distance parallel to the grating lines. For elastic scattering, the additional condition is to be met that the absolute value of the wave vector must be preserved, i.e. the endpoint must also lie on the so-called Ewald sphere. Furthermore, from the boundary condition that no momentum transfer

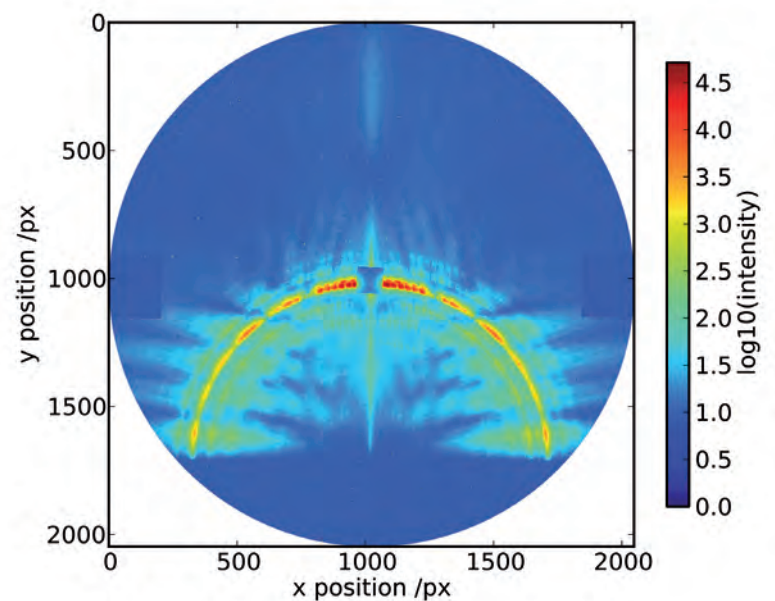


Figure 2: Diffraction orders of a line grating in GISAXS geometry, measured with a CCD-based detector. Due to the logarithmic intensity scale, also weak satellite orders, which are generated by periodic fluctuations in the line width or line position, can be seen in addition to the orders on the main circle.

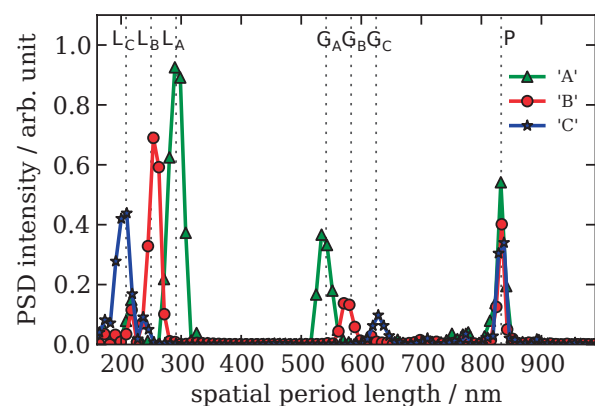
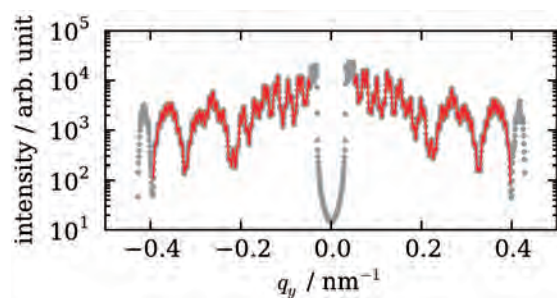


Figure 3: Left: Intensity distribution of the diffraction orders of the grating on the main circle, determined from the scatter diagram (Figure 2). Right: Correlation lengths (determined by Fourier transformation of the intensity distribution of the diffraction orders) for three different gratings (A, B, C) with the same period P , but with different line widths G_A , G_B , G_C .

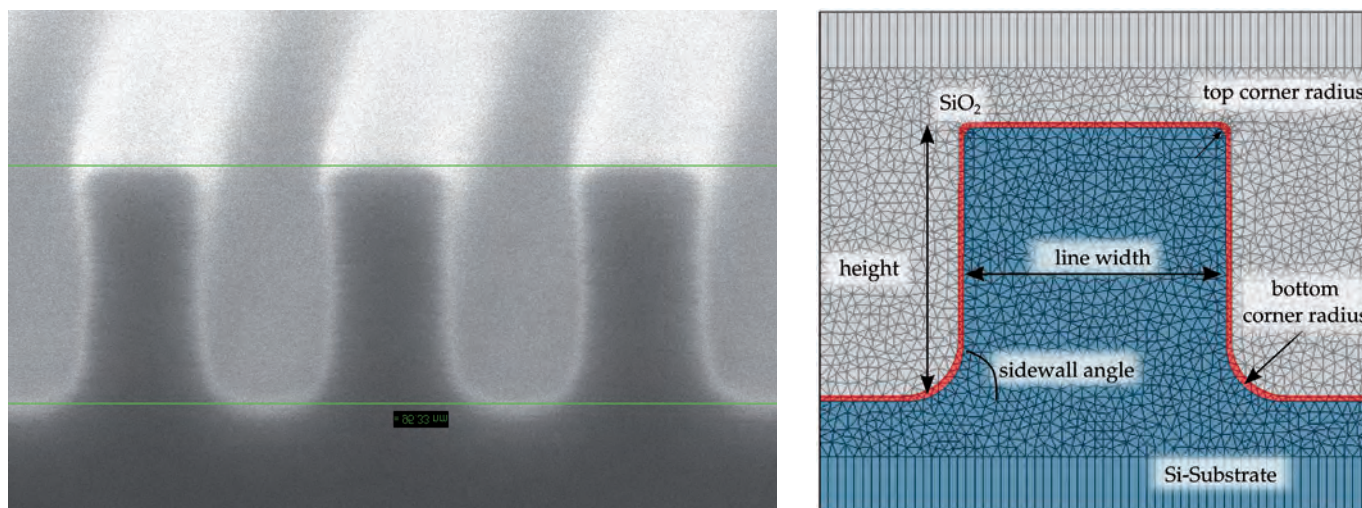


Figure 4: Parameterization of the line structure of a Si grating with a SiO₂ layer on the surface. Left: SEM image of a cleavage edge through a grating. One sees a largely flat upper surface of the lines, whereas the bottom of the etched channel between the lines is strongly rounded. Right: Discretization of the structure for the numerical solution of the Maxwell equations.

takes place in *x*-direction, it follows that the wave vector lies on a cone whose opening angle is twice the angle of incidence α_i of the radiation to the surface. From these conditions it follows that the diffraction orders of a grating in this geometry lie on a circle in the plane of the detector (as shown

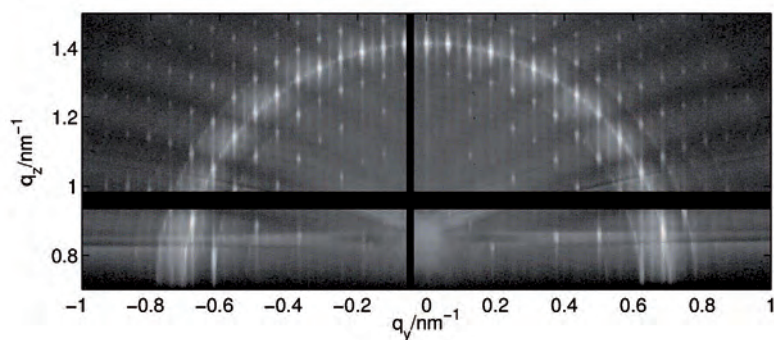


Figure 5: Diffraction orders of a line grating with a period of 100 nm and a nominal line width of 50 nm in GISAXS geometry.

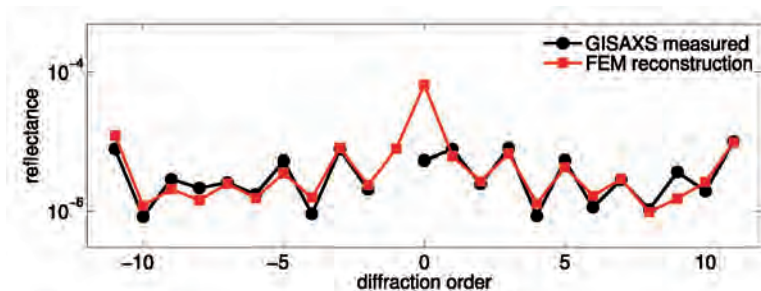


Figure 6: Comparison of the measured and of the reconstructed diffraction intensities of a line grating with the geometrical parameters from Table 1.

in Figure 2). After the three-dimensional parameters have been neglected, only the distances and the widths of the lines remain as parameters to be determined for an evaluation according to the simplified method of the Fourier transformation. Here, this procedure is shown on the basis of the data of three gratings (A, B, C) with a period of $P = 833$ nm and nominal widths of the lines of $G_A = 541$ nm, $G_B = 583$ nm and $G_C = 625$ nm. Figure 3 (left) shows an exemplary intensity distribution of the numerous diffraction orders, and Figure 3 (right) shows the correlation lengths which have been obtained by Fourier transformation and which reflect the nominal structure widths very well (i.e. in addition to the period and to the line widths, also their differences L_A , L_B and L_C). This strongly simplified procedure which allows only a few parameters to be determined, has, however, the advantage that – in addition to the quantities which are directly accessible to the measurement – no further assumptions regarding a model are included. This makes this type of measurement directly traceable [4].

For the determination of additional parameters such as, for example, corner radii, numerical models are required to determine the diffraction intensities. For this purpose, complex program packages such as, for example, JCMSuite from JCMsuite from JCMwave [5, 6] are needed. Figure 4 shows the cross section measured on a cleavage of a prototype and the discretized mesh model of JCMSuite for a grating with a period of 100 nm and a line width of 50 nm. This model was used for the evaluation of the corresponding GISAXS data (Figure 5) [7]. As, due to the smaller period, clearly less diffraction orders are visible than for

the grating shown in Figure 2, the Fourier method is applicable here only to a limited extent. Furthermore, the edge angle, the line height and the rounding of the upper and lower edges are to be determined in addition to the line width. Figure 6 shows the good agreement of the measured diffraction intensities with the values calculated for the optimized geometrical model. The geometrical parameters determined in this way are summarized in Table 1.

Investigation of EUV photomasks

Another technologically very important class of samples are line structures on Bragg-reflecting multi-layer systems (Figure 7). They are used in the manufacture of lithographic photomasks for EUV lithography, which are currently being introduced in production in the semiconductor industry for the manufacture of future structure widths of 16 nm and smaller [8, 9]. The investigation of these structures is particularly challenging, as they are used in reflection at a wavelength of 13.5 nm. For the inspection with optical systems, the contrast is very low, and the reflection in Mo/Si-Bragg multi-layer systems cannot be determined by measurements with SEM or AFM. An investigation at the working wavelength is, therefore, indispensable. The use of scattering procedures allows a fast measurement to be performed and does not require a sophisticated EUV imaging system. The measurement geometry differs from the GISAXS examples shown above, in particular by the almost normal incidence on the sample (Figure 8). Mathematical handling is, however, equivalent. For many years, this measurement procedure [10] has been investigated in detail at PTB. This includes, in particular, investigations of disturbances of the ideal structure (for example, by edge roughnesses [10, 11]) and investigations to determine the measurement uncertainties [12].

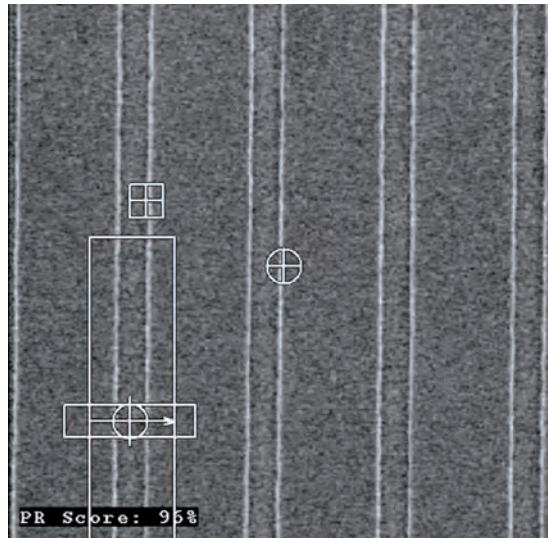


Figure 7: Image of a grating structure on an EUV photomask.

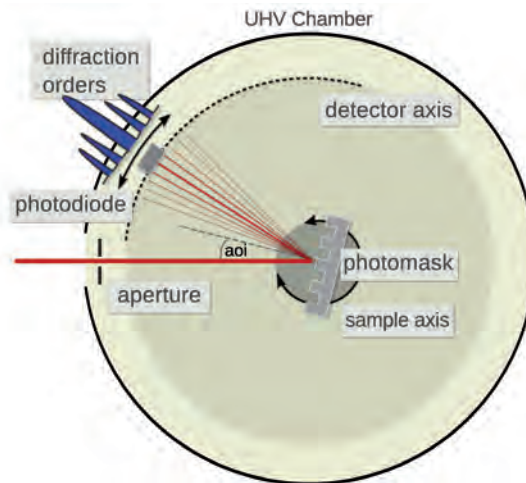


Figure 8: Scheme of EUV scatterometry. Here, the radiation hits the sample at normal instead of grazing incidence. The grating lines are oriented vertically to the reflection plane, and the diffraction orders are measured on a detector circle with a photodiode.

	Nominal value	Measurement
Period / nm	100	-
Line height / nm	50	49.6
Line width / nm	50	49.7
Edge angle / nm	90	89.8
Radius of the upper edges / nm	-	1.8
Radius of the lower edges / nm	-	23
Thickness of the oxide layer / nm	-	4.8
Roughness (rms) / nm	-	2.4

Table 1: Geometrical parameters for the reconstruction of the line profile from the GISAXS data in Figure 5 and Figure 6 with the JCMSuite software. The nominal values served as starting values for the fitting procedure. During modeling, the period is, however, fixed.

A comparison with measurements on a metrologically traceable AFM shows fair agreement within the scope of the combined uncertainties [13]. As an example, Figure 9 shows the comparison of the line width measurement (CD) with EUV scatterometry and AFM.

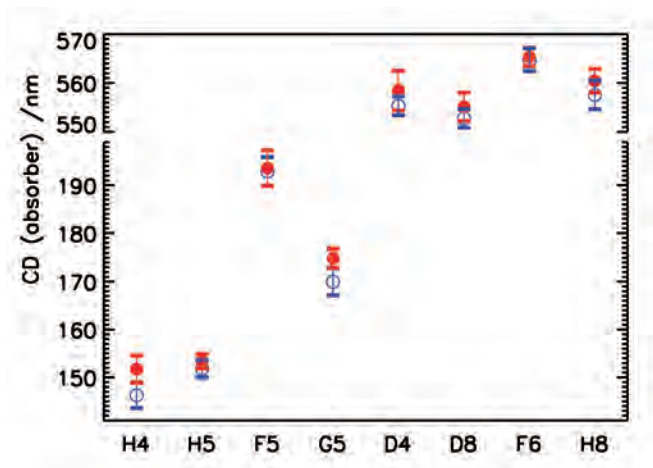


Figure 9: Determination of the width (CD) of different absorber lines in a test mask (the designations on the X-axis stand for the measurement fields named in chessboard fashion). The blue data points are the results of EUV scatterometry, the red points were measured with a metrologically calibrated AFM. The error bars show the 95 % confidence interval.

References

- [1] M. Krumrey, R. Garcia-Diez, C. Gollwitzer, S. Langner: in this publication on p. 53
- [2] M. Richter, G. Ulm: in this publication on p. 3
- [3] M. Krumrey, L. Cibik, A. Fischer, A. Gottwald, U. Kroth, F. Scholze: in this publication on p. 35
- [4] J. Wernecke, F. Scholze, M. Krumrey: *Rev. Sci. Instrum.* **83**, 103906 (2012)
- [5] J. Pomplun, S. Burger, L. Zschiedrich, F. Schmidt: *Phys. Status Solidi B* **244**, 3419 (2007)
- [6] S. Burger, L. Zschiedrich, J. Pomplun, F. Schmidt: *Proc. SPIE* **8083**, 80831B (2011)
- [7] V. Soltwisch, J. Wernecke, A. Haase, J. Probst, M. Schoengen, M. Krumrey, F. Scholze: *Proc. SPIE* **9050**, 905012 (2014)
- [8] https://en.wikipedia.org/wiki/International_Technology_Roadmap_for_Semiconductors (retrieved: 2016-07-01)
- [9] F. Scholze, C. Laubis, A. Barboutis, C. Buchholz, A. Fischer, J. Puls, C. Stadelhoff: in this publication on p. 43
- [10] A. Kato, S. Burger, F. Scholze: *Appl. Opt.* **51**, 6457 (2012)
- [11] A. Kato, F. Scholze: *Appl. Opt.* **49**, 6102 (2010)
- [12] M.-A. Henn, H. Gross, S. Heidenreich, F. Scholze, C. Elster, M. Bär: *Meas. Sci. Technol.* **25**, 044003 (2014)
- [13] F. Scholze, V. Soltwisch, G. Dai, M.-A. Henn, H. Gross: *Proc. SPIE* **8880**, 88800O (2013)

Size Determination of Nanoparticles with Small-angle X-ray Scattering

Michael Krumrey*, Raul Garcia-Diez, Christian Gollwitzer, Stefanie Langner

Small-angle X-ray scattering (SAXS) is an established method for the dimensional characterization of objects in the nanometer range [1]. It allows, for example, the size determination of micro- and nanoparticles with mean diameters in the range between a few nanometers and approx. 300 nm. Metrological traceability to the International System of Units (SI) has been achieved at PTB's laboratory at BESSY II in the past few years for sufficiently monodisperse nanoparticles; this is highly relevant to numerous applications in dimensional nanometrology. But dimensional investigations can also be carried out on nanoparticles with a broader size distribution. This article provides an overview of the method, of the experimental set-up used at PTB, and of the analysis of SAXS measurements; it shows examples of the traceable size determination of reference materials and the investigation of biological nano-objects.

In this measurement procedure, an almost parallel and monochromatic X-ray beam hits a sample which is present in a liquid, for example in the form of a suspension of nanoparticles, and is located within a thin-walled glass capillary tube. It is also possible to examine solid samples, for example to determine the pore size. In both cases, the X-rays are scattered forward due to discontinuities in the electron density, i.e. under small angles in relation to the direction of the radiation, and are then registered by an area detector (Figure 1). Hereby, the scattered radiation is less intensive than the transmitted beam by several orders of magnitude and it decreases further from the paraxial to the edge region, again by several orders of magnitude. The direct beam must therefore be shielded by means of a beamstop in order not to overload the detector. The scattering pattern is analyzed by comparison with mathematical models; contrary to microscopic techniques such as electron or scanning force microscopy, one measurement suffices to immediately obtain

the mean size of a large number of particles which interests the most. Furthermore, sample preparation is not particularly tedious. SAXS is thus the ensemble method used at PTB when it comes to determining the size of nanoparticles [2].

SAXS measurements require intensive, monochromatic X-rays of low divergence. Synchrotron radiation is therefore best suited. At PTB's laboratory, the four-crystal monochromator (FCM) beamline is used; it covers the photon energy range from 1.75 keV to 10 keV [3, 4]. Up to 15 filled capillary tubes can be introduced simultaneously into the X-ray reflectometer [5, 6] which serves as the sample container. A large-area, spatially resolving detector is used to record the scattering pattern. To be able to measure across the full energy range of the beamline, a specially developed, vacuum-compatible hybrid pixel detector (Dectris PILATUS 1M) with a total surface of 179 mm × 169 mm and a pixel size of 172 μm is used [7]. The distance between the sample and the detector can be varied continuously between 2.2 m and 4.3 m using the SAXS facility of the *Helmholtz-Zentrum Berlin* (HZB) which is operated several times a year at the FCM beamline [8].

* Dr. Michael Krumrey, Working Group "X-ray Radiometry", e-mail: michael.krumrey@ptb.de

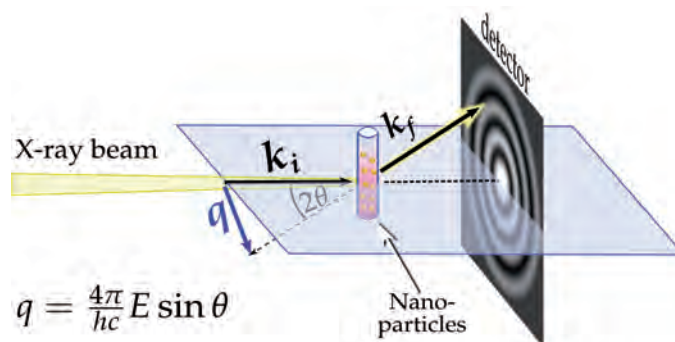


Figure 1: Principle of SAXS measurements.



Figure 2: SAXS instrument of the *Helmholtz-Zentrum Berlin* (HZB) at the FCM (four-crystal monochromator) beamline at PTB's laboratory at BESSY II. The directly connected vacuum-compatible PILATUS detector is visible at the bottom right.

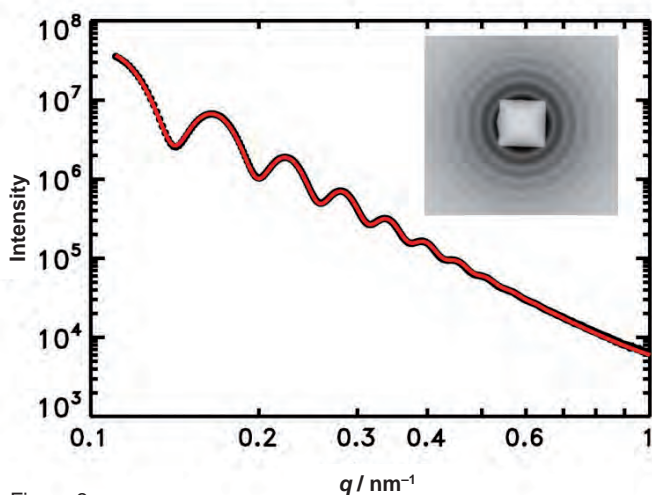


Figure 3: Scattering curve for almost monodisperse PMMA particles with a nominal diameter of 108 nm. The fit yields a mean diameter of (109.0 ± 0.8) nm.

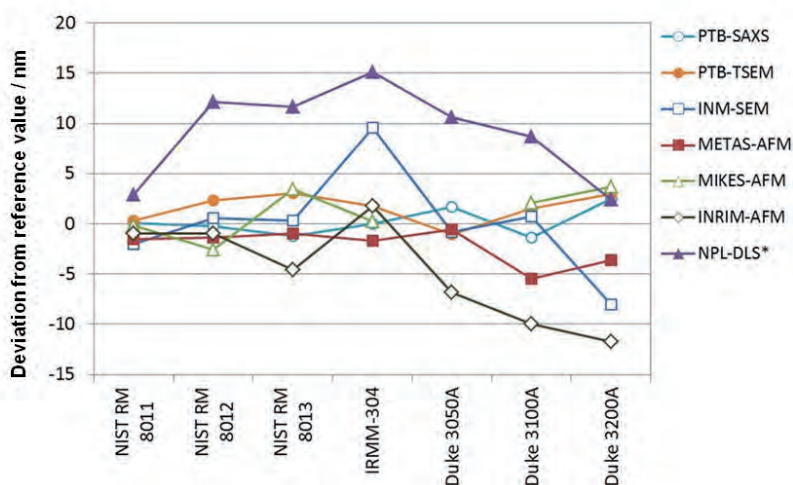


Figure 4: Result of a European project on the traceability of the determination of the size of nanoparticles with 5 different measurement methods at 6 national metrology institutes. The particles in the 7 samples investigated had mean diameters from 10 nm to 200 nm.

To investigate nanostructured surfaces in reflection geometry at grazing incidence (GI)-SAXS (which is described in another article of this publication [9]), the whole facility can also be tilted by up to 3°. Also nanoparticles located on surfaces can be investigated using GISAXS [10].

In a normal SAXS geometry, the scattering pattern of monodisperse particles (i.e. particles with a narrow size distribution) consists, as shown in Figure 3, of concentric circles. By averaging, the radially symmetric scattering pattern can be reduced to one-dimensional scattering curves which then only depend on the scattering angle. For further computation, the amount q of the scattering vector is introduced; it is defined by the following relation:

$$q = \frac{4\pi}{\lambda} \sin\theta = \frac{4\pi E}{hc} \sin\theta \quad .$$

Hereby, λ is the wavelength and E is the energy of the X-rays, and θ is half the scattering angle. A scattering curve obtained in this way for monodisperse PMMA nanoparticles with a nominal diameter of 108 nm is shown in Figure 3, together with the original scattering pattern [8]. The square in the center is the shadow of the beamstop which blocks off the direct beam transmitted through the sample. In the calculation of the scattering curve, the transmission of the sample has been taken into account, and the scattering of a water-filled capillary tube has been subtracted.

The scattering curve can be fitted using an analytical model. Similar to the determination of the layer thickness by means of X-ray reflectometry [6], here too, the periodicity of the observed oscillations serves size determination, and here too, exact knowledge of the wavelength is exploited which, contrary to light scattering in the visible range, is considerably smaller than the objects under investigation. Whereas the period of the oscillations only depends on the mean particle diameter in the case of compact, spherical objects, besides the distribution width, also the parameters of the background enter into the amplitude, which results in higher uncertainties in this case. For monodisperse particles which can be described as homogeneous spheres, SAXS, however, meanwhile provides results that can be traced to the SI system for the mean diameter with very low uncertainties, as shown in Figure 4, where the results of a method comparison of European metrology institutes is depicted [11]. For the nanoparticles of a size in the range from 10 nm to 200 nm which were investigated using different methods, the values obtained with SAXS at PTB's laboratory exhibited the smallest deviation from the corresponding reference value. The determination

of the sample/detector distance, the pixel size of the detector and the adjustment of the model are the main contributions to the uncertainty. With suitable particles, relative uncertainties of 1 % can be achieved.

Figure 5 shows the more complex case of a bidisperse size distribution which is due to the mixing of two monodisperse fractions. For this mixture, the mean diameter and the distribution widths of the two components were determined in agreement with the results obtained separately with each of the two components [8].

Particularly interesting applications of small-angle X-ray scattering are encountered in the field of biological nano-objects and in nanoparticles in biological media. For particles made of materials with relatively low density (e.g. polystyrene), the adsorption of proteins can be detected by an increase in diameter. As shown in Figure 6, the protein shell becomes thicker when the concentration of, e.g., immunoglobulin G (IgG) increases in the surrounding solution [12]. In contrast, in the case of heavy particles, the influence of the shell is very small so that, as opposed to other procedures, the diameter of the actual particles can always be determined.

Biologically relevant nano-objects mostly exhibit a relatively wide diameter and shape distribution; equidistant circles are therefore seldom. But here too, there can be distinct structures, as shown in Figure 7 in the scattering curve for synthetic phospholipid vesicles which serve as a model system for biological membranes [13]. The size of the vesicles can be determined at small q values, whereas the thickness of the double layer is obtained from scattering curves at high q values.

Natural extracellular vesicles are present in all body fluids. Within the scope of a European metrology project, SAXS is used also here in combination with other technologies for size determination. Besides the large distribution width, also the low concentration of the vesicles and the existence of other particles in a similar size range are a challenge. With samples prepared with the greatest care, it was, however, possible to achieve first results. The scattering curve for erythrocyte vesicles shown in Figure 8 can be described by a vesicle distribution with a mean diameter of 125 nm and a full width at half maximum of the size distribution of 90 nm, as well as by a contribution of clearly smaller free proteins [14].

Also other biological issues such as, e.g., the influence of DNA and of heparin on the mechanical stability of blood clots were investigated at PTB's laboratory at BESSY II using SAXS [15]. For deeper investigations, also interesting is the so-called *anomalous small-angle X-ray scattering* (ASAXS), which exploits the change in the scattering intensity in the vicinity of an absorption

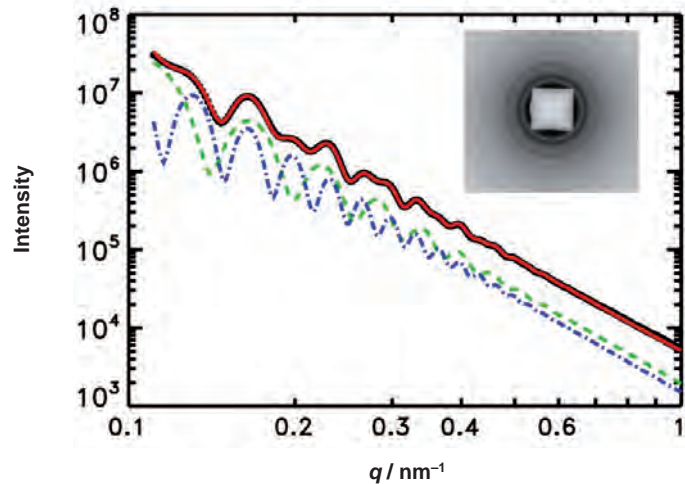


Figure 5: Scattering curve for a mixture of PMMA particles with nominal diameters of 108 nm and 192 nm. The fit provides both size distributions with mean values of 109.2 nm and 188.2 nm.

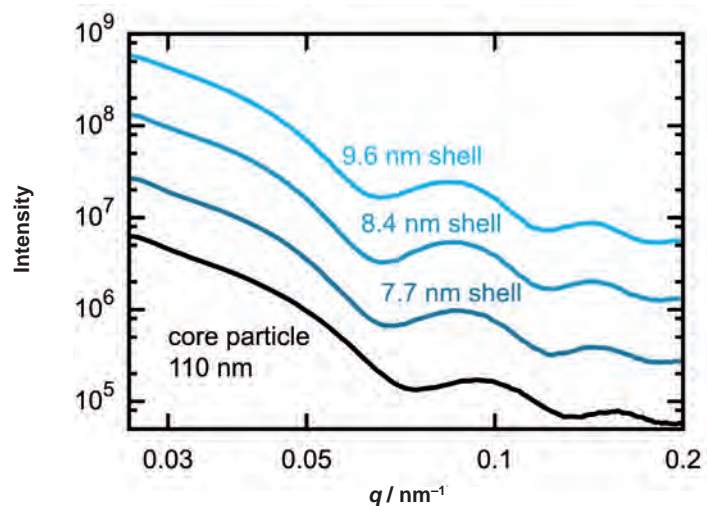


Figure 6: Size increase of polystyrene nanoparticles by adsorption of proteins at increasing concentrations of immunoglobulin G (IgG).

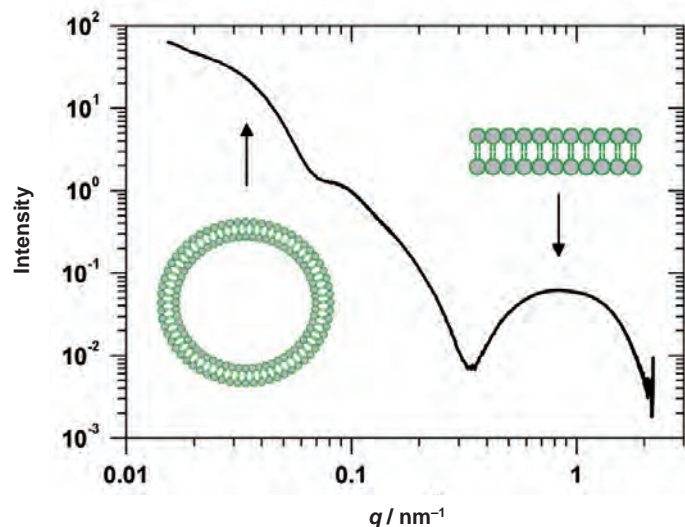


Figure 7: Scattering curve for phospholipid vesicles from which a mean diameter of 75 nm can be determined at small q values and a thickness of the double layer of 4 nm at high q values [13].

edge. It allows statements, for example, on the distribution of chemical elements in core/shell systems. With the vacuum-compatible hybrid pixel detector at the FCM beamline, unlike most other SAXS facilities worldwide, also the adsorption edges of the biologically relevant elements calcium, potassium, chlorine, sulphur and phosphor are accessible. ASAXS investigations on the Ca edge have already been successfully completed [16].

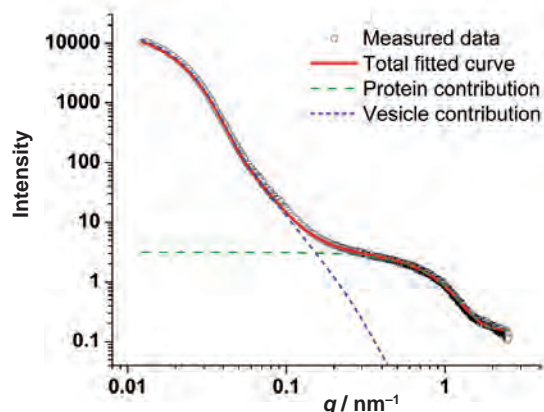


Figure 8: Scattering curve for erythrocyte vesicles which can be described by a vesicle distribution with a mean diameter of 125 nm and a full width at half maximum of the size distribution of 90 nm as well as by a contribution of clearly smaller free proteins.

References

- [1] O. Glatter, O. Kratky (Eds.): Small-angle X-ray Scattering, Academic Press, London (1982)
- [2] A. Jordan-Gerkens, E. Buhr, T. Klein, C. G. Frase, M. Krumrey, T. Dziomba, A. Nowak, V. Ebert: PTB-Mitteilungen **121**, No. 2, 5 (2011)
- [3] M. Krumrey, G. Ulm: Nucl. Instr. and Meth. A **467–468**, 1175 (2001)
- [4] M. Richter, G. Ulm: in this publication on p. 3
- [5] D. Fuchs, M. Krumrey, P. Müller, F. Scholze, G. Ulm: Rev. Sci. Instrum. **66**, 2248 (1995)
- [6] M. Krumrey, L. Cibik, A. Fischer, A. Gottwald, U. Kroth, F. Scholze: in this publication on p. 35
- [7] J. Wernecke, C. Gollwitzer, P. Müller, M. Krumrey: J. Synchrotron Rad. **21**, 529 (2014)
- [8] G. Gleber, L. Cibik, S. Haas, A. Hoell, P. Müller, M. Krumrey: J. Phys. Conf. Ser. **247**, 012027 (2010)
- [9] F. Scholze, A. Haase, M. Krumrey, V. Soltwisch, J. Wernecke: in this publication on p. 48
- [10] M. Krumrey, G. Gleber, F. Scholze, J. Wernecke: Meas. Sci. Technol. **22**, 094032 (2011)
- [11] F. Meli et al.: Meas. Sci. Technol. **23**, 125005 (2012)
- [12] C. Minelli, R. Garcia-Diez, A. Sikora, C. Gollwitzer, M. Krumrey, A. G. Shard: Surf. Interface Anal. **46**, 663 (2014)
- [13] E. van der Pol, F. Coumans, Z. Varga, M. Krumrey, R. Nieuwland: J. Thromb. Haemost. **11** (Suppl. 1), 36 (2013)
- [14] Z. Varga, Y. Yuana, A. E. Grootemaat, E. van der Pol, C. Gollwitzer, M. Krumrey, R. Nieuwland: J. Extracell. Vesicles **3**, 23298 (2014)
- [15] C. Longstaff, I. Varjú, P. Sótónyi, L. Szabó, M. Krumrey, A. Hoell, A. Bóta, Z. Varga, E. Komorowicz, K. Kolev: J. Biol. Chem. **288**, 6946 (2013)
- [16] A. Hoell, Z. Varga, V. S. Raghuvanshi, M. Krumrey, C. Bocker, C. Rüssel: J. Appl. Cryst. **47**, 60 (2014)

X-ray Spectrometry with Synchrotron Radiation

Matthias Müller*, Martin Gerlach, Ina Holfelder, Philipp Hönicke, Janin Lubeck, Andreas Nutsch, Beatrix Pollakowski, Cornelia Streeck, Rainer Unterumsberger, Jan Weser, Burkhard Beckhoff

Introduction

X-ray spectrometry based on radiometrically calibrated instruments, which ensures the physical traceability of quantification to the SI units, is a unique feature of PTB. For X-ray spectrometry, various beamlines are available at PTB's laboratory at BESSY II in the spectral ranges of soft and hard X-rays (78 eV to 10.5 keV), as well as the "BAMline" for photon energies up to 60 keV [1–4]. With X-ray spectrometry, surfaces, solids, liquids, nanolayers and nanostructures can be characterized with regard to their physical and chemical properties – such as chemical composition, elemental depth profiles, layer thicknesses, and species and coordination fractions. The functionality of nano-scaled materials with designed physical and chemical properties can provide new functionalities for applications in areas such as health, energy, transport, and climate protection. Such materials have to be developed increasingly fast; this requires reliable analytical characterization methods for a timely correlation of the functionalities with the underlying material properties. Only few reference materials are available in the different categories with nano-scale structures or nanolayers, whereas several dozens of new materials are created every month. This is becoming too much to guarantee a reliable chemical traceability of numerous characterization technologies. This circumstance – which limits materials research and development – can be counteracted by reference measurement procedures such as, for example, X-ray spectrometry.

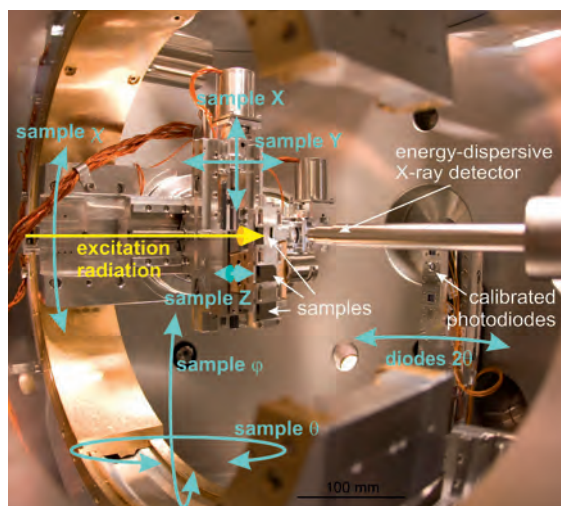
Based on radiometry with synchrotron radiation [5], PTB uses calibrated detectors for X-rays to develop and apply X-ray-spectrometric measurement procedures and quantification algorithms for a characterization of materials that is physically traceable to the SI units [6]. The methodology developed by PTB, i.e. *reference-free*

X-ray fluorescence analysis (XRF), is in the focus of the constant instrumental and scientific development of X-ray spectrometry for application in the aforementioned subject areas [7]. Especially the extension of reference-free XRF for the geometry of grazing incidence (GIXRF) and the utilization (thus made possible) of the information depth (which can be tuned via the angle of incidence) and of the increased detection sensitivity for nanostructured materials are some of the goals of these activities. X-ray absorption spectrometry was further developed for the depth-sensitive identification and quantification of chemical valence states in nanostructured materials, and the information depth, which depends on the angle of incidence and on the photon energy, was investigated. Besides XRF, synchrotron radiation is used in the PTB laboratory at BESSY II also for research and development in the field of high-resolution X-ray emission spectrometry (XES). So far, the activities in the field of high-resolution XES have been focused on investigating the interaction of electromagnetic radiation with matter, and on the determination of relevant atomic fundamental parameters (FPs) such as ionization cross sections, transition probabilities and fluorescence yields. For a traceable quantification with small uncertainties, the FPs have to be known with good accuracy.

New developments in X-ray-spectrometric instruments are aimed at improved mechanical precision and a flexible beam geometry, as well as at wavelength-dispersive spectrometers with the highest possible detection sensitivity in an extended spectral range and with the capability of radiometric calibration. Furthermore, vacuum-compatible thin-window cells have been developed to investigate liquids and carry out in-situ measurements on battery materials. Research and development on new XRF instruments and atomic FPs are performed in close

* Dr. Matthias Müller,
Working Group
"X-ray Spectrometry",
e-mail: matthias.mueller@ptb.de

Figure 1: Measuring arrangement for X-ray spectrometry with the 9-axle manipulator in a GIXRF beam geometry.



cooperation with various manufacturers of X-ray-analytical devices as well as with several research institutes. In the following sections, we will present new developments of instruments as well as topical examples of applications of X-ray spectrometry with synchrotron radiation.

Development of instruments for X-ray spectrometry

For quantitative analysis, by means of synchrotron radiation, on samples having a size of up to 100 mm × 100 mm, a new measuring station has been developed for X-ray spectrometry and reflectometry measurements [8]. The core piece is an ultra-high vacuum (UHV) chamber equipped with a 9-axis manipulator. This special manipulator (Figure 1) allows a flexible beam geometry and a precise adjustment of the samples in all translatory and rotatory degrees of freedom. Furthermore, the chamber is equipped with several photodiodes mounted on a 2-theta arm to measure the incident or the reflected photon flux, an aperture system to define the solid angle of detection, and a load-lock system to enable fast sample change. The measuring station is optimized for use at the plane-grating and at the four-crystal monochromator beamlines of PTB at BESSY II [4]. The flexible beam geometry – from total reflection (TXRF) to

grazing incidence (GIXRF) and to the conventional 45° geometry – and the fact that X-ray reflectometry can be performed simultaneously, allow the characterization of complex sample systems such as nanolayers, nanoparticles and interface layers with regard to mass deposition, layer thickness, depth-dependent elemental composition, and chemical species. At the same time, it is also possible to investigate the molecular orientation of organic bonds by means of polarization-dependent experiments. The design of the measuring station is the basis for successfully completed technology transfer projects carried out with the *Berlin Laboratory for innovative X-ray Technologies* (BLiX), which is accommodated at Berlin Technical University, for use with a plasma source, as well as with the *International Atomic Energy Agency* (IAEA) of the United Nations and the *Laboratoire National Henri Becquerel* (LNE LNHB) for use at the storage rings ELETTRA in Trieste, Italy, and SOLEIL in Saclay, France.

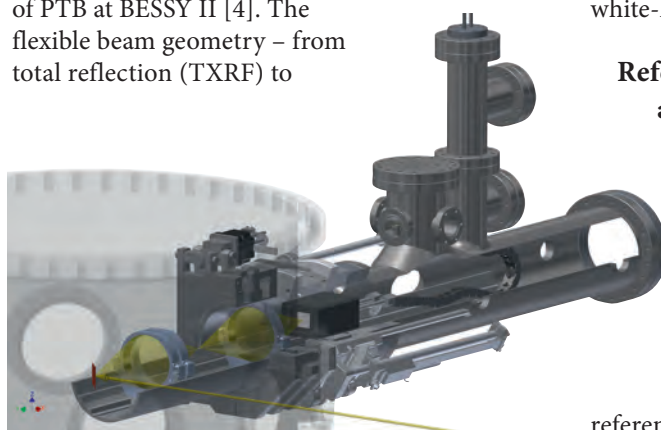
A further example of the development of instruments for X-ray spectrometry at PTB is the extension of calibratable wavelength-dispersive spectrometers to detect X-rays with photon energies higher than 2.4 keV. To this end, a crystal spectrometer is currently being constructed and will be set up in 2016 (see Figure 2). This new spectrometer will be optimized to be calibratable and to have the highest possible sensitivity as well as a broad spectral range utilizable for XES experiments. High sensitivity is to be attained by designing the dispersive crystals as full cylinders in *von Hamos* geometry, and by using mosaic crystals made of highly annealed pyrolytic graphite (HAPG) with high reflectivity and very small mosaic spread. For characterization, various HAPG crystals were investigated (within the scope of a joint project with TU Berlin and the *Optigraph* company) with regard to relevant characteristics (reflectivity and homogeneity) at the *BAMline* [4] using diffractometry. In addition, the crystals were characterized with regard to their energetic resolving power within the scope of spectroscopic tests at PTB's white-light dipole beamline.

Reference-free X-ray fluorescence (XRF) analysis

XRF is a widely used method for the non-destructive characterization of materials for determination of the elemental composition, layer thicknesses, mass distributions and minimum contaminations [9].

Quantification is normally traced to certified calibration standards and reference materials with the most similar matrix

Figure 2: Concept of the new calibratable *von Hamos* spectrometer for high-resolution X-ray emission spectrometry in the range of hard X-rays (2.4 keV to 20 keV).



elemental composition (chemical traceability) possible. The decisive advantage of XRF without reference samples – as developed by PTB – is that it is absolutely independent of suitable calibration standards and reference materials, as these are often not available or would have to be developed and certified with great effort [7]. Especially when characterizing new materials in the field of nanotechnologies with very short and dynamic development cycles, reference-free XRF can be used very flexibly and without any limitation due to a lack of calibration standards.

Thanks to the development and validation of the concept of "effective solid angle of detection", reference-free XRF can also be used for beam geometries of grazing incidence [10]. This has allowed the scope of application of this method to be considerably extended. In the area of TXRF, for example, extremely small amounts of substance were determined on various substrate materials (e.g. semiconducting substrates such as Si, SiO₂, Ge, GaAs, InGaAs, InP, etc.) [11]. In the transition range between TXRF and conventional 45° geometry, GIXRF allows the composition and thickness of thin layers and multilayer systems to be determined down into the sub-nanometer range [12]. In addition, the adjustable information depth can be used for the quantitative characterization of element depth profiles such as, for example, ultra-shallow implantations or diffusion profiles [13].

Determining atomic fundamental parameters (FPs)

Quantitative XRF is based on the precise knowledge of the atomic fundamental parameters (FPs) involved, which allows physical modeling of the characteristic X-ray fluorescence radiation emitted by a sample. The FPs consist of mass absorption coefficients, ionization cross sections, fluorescence yields, Coster-Kronig factors, and transition probabilities. The different databases available for these fundamental parameters are based on – partly – rather old experimental and theoretical data with estimated uncertainties amounting to up to 50 % [14]. Using radiometrically calibrated instruments of PTB [8], different atomic FPs can be newly determined with traceable and reduced uncertainties [15–17]. For this purpose, dedicated experiments are carried out with – usually – thin, self-supporting foils of the elements to be investigated. For example, the photon-energy-dependent mass attenuation coefficients can be obtained from transmission measurements, whereas determining fluorescence yields or Coster-Kronig factors requires experiments with energy- or wavelength-dispersive X-ray detectors [18].

Grazing incidence X-ray fluorescence analysis (GIXRF)

Reference-free GIXRF can be used to obtain quantitative and non-destructive access to elemental depth gradients in thin layers at the nanometer and at the micrometer scale, for example the determination of elemental depth profiles of ion implantations [13]. This procedure is used in the semiconductor industry to generate ultra-shallow doping profiles with depths in the range of a few nanometers. The optical properties of the substrate material are in part – depending on the implanted dose and on the material combination – considerably modified in the implanted depth range. If these modifications are not taken into account when computing the wave field (XSW) created at the surface and at the interface of very flat materials, this leads to considerable deviations in the calculated elemental depth profile [19, 20]. The simultaneous measurement of the intensity of the radiation reflected by the sample, however, provides access to the optical constants of the implanted sample, so that simultaneous modeling of the measured reflectivity allows a significantly improved XSW computation and – thus – reliable depth profiling of the implantation. This is illustrated by the graphs shown in Figure 3 with the example of an aluminum implantation in silicon [21].

Hereby, the aluminum profile represented in green has been computed with an XSW field using tabulated optical constants of silicon, thus neglecting the influence of the implantation. Compared to the simulated element profile (TRIM [22]) and to the results of complementary measurement procedures such as secondary-ion mass spectrometry (SIMS), clear deviations are obvious. The results are clearly in better agreement with each other when reflectometry data obtained from measurements is used simultaneously to compute the wave field (purple curve).

Taking self-absorption and secondary excitation effects into account, also matrix elemental gradients can be determined of rough layers with thicknesses of a few micrometers. An example of such an application is the determination of the elemental depth distribution in Cu(In,Ga)Se₂ absorbers of high-efficiency thin-film solar cells (Figure 4) whose efficiency depends on the optimum adjustment of the band gap within the absorber layer by varying the depth of the elemental composition [23, 24]. These approx. 2 μm thick layers exhibit a double gradient in the Ga concentration. Whereas the average Ga concentration lies between 8 at% and 9 at%, at the same time, a clear gradient of the Ga concentration becomes visible, with a maximum at the surface and on the reverse side of the absorber

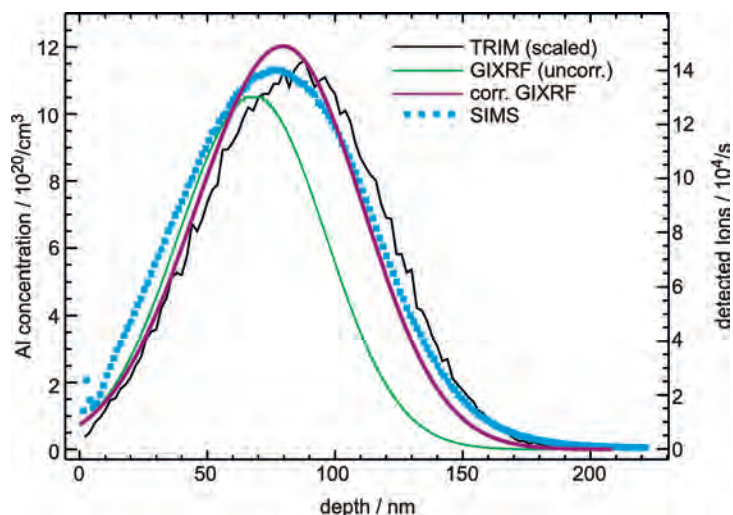


Figure 3: Comparison of the elemental depth profiles determined by means of GIXRF for Al implantations in silicon with a dose of 10^{16} atoms per cm^2 and an implantation energy of 50 keV. If not taken into account, the changed optical constants of the ion-implanted silicon lead to a significant deviation of the determined elemental depth profile.

Figure 4: Layer model of a $\text{Cu}(\text{In,Ga})\text{Se}_2$ thin-film solar cell. For the GIXRF investigations, the $\text{Cu}(\text{In,Ga})\text{Se}_2$ absorber is measured on the Mo back contact and on the glass substrate without a CdS buffer layer nor a ZnO window layer.

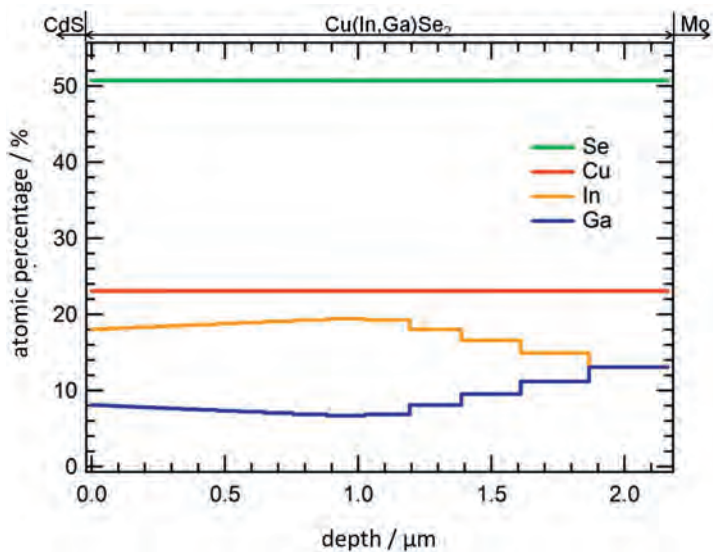
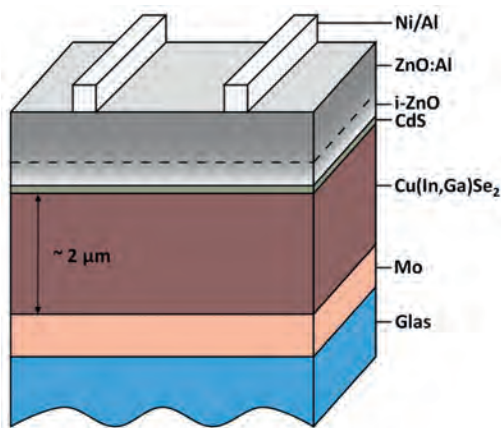


Figure 5: Elemental depth distribution of Cu, Ga, In and Se quantified without a reference sample in a $\text{Cu}(\text{In,Ga})\text{Se}_2$ absorber (Figure 4) [25].

layer (Figure 5). Since In and Ga occupy the same lattice sites, the In gradient runs in the opposite direction to the Ga gradient. The concentrations of Cu and Se run nearly constantly. Hereby, the Ga-to-In gradient may, depending on the process parameters used for manufacturing, vary from a few at% to up to 10 at%. In and Ga determine, among other things, the band gap of the absorber layer. For maximum efficiency of the solar cell, the elemental depth gradient must be adjusted optimally, taking the available process methodologies into account. Within the scope of a cooperation project between PTB, *Helmholtz-Zentrum Berlin für Materialien und Energie* (HZB) and TU Berlin, a quantification algorithm based on reference-free GIXRF measurements was developed to allow quantitative access to the elemental depth gradient in thin-film solar cells [25]. Hereby, the angular regime between 0° and 3° exhibits high sensitivity for the Ga-to-In gradients [26].

Using a reference-free GIXRF methodology can, thus, contribute to developing new manufacturing procedures for thin-film solar cell absorbers, for example by qualifying suitable calibration samples for complementary inline and offline procedures. Furthermore, this methodology can be applied not only to $\text{Cu}(\text{In,Ga})\text{Se}_2$ thin films, but also to the characterization of the most various micro- and nano-scaled layers made from various fields of materials science.

High-resolution X-ray absorption spectrometry

The combination of near-edge X-ray absorption fine structure spectroscopy (NEXAFS) and GIXRF enables the depth-sensitive and non-preparative determination of the chemical properties of buried structures and interfacial layers – i.e. without unintentionally modifying the object under investigation. The angle of incidence and the photon energy hereby define the penetration depth of the excitation radiation as well as the XSW created at the surface and at the interface of flat materials, which allows the mean information depth to be varied. Furthermore, the XSW depends on the energy-dependent complex refractive index of the material. With the NEXAFS method, the fine structure of the X-ray absorption edges is investigated by varying the photon energy of the incident X-rays. If the photon energy is varied in the range of the absorption edge of a matrix element, then the penetration depth – and thus the information depth – clearly changes. To obtain a constant mean information depth within a NEXAFS measurement, the angle of incidence must therefore be adapted in such a way that the energy dependence is constant. To determine the chemical species at an interface, NEXAFS measurements must be

carried out at different information depths (upper layer, interface and bottom layer) to be able to apply comparison and differential methodologies. The respective angle of incidence must have been determined in advance; this can be done experimentally or by modeling [20]. This strategy is implemented and validated by means of the thin-film model system depicted in Figure 6, which consists of the transition metal nickel and of a boron carbonitride [27]. The NEXAFS spectra of nickel at the interfacial layer represented in Figure 7 show that, depending on the synthesis temperature, nickel forms a different bond at the interface towards lighter elements. At lower temperatures (200 °C), besides the metallic Ni, also a Ni-C bond forms at the interface. At higher temperatures (from 400 °C to 500 °C), the nickel atoms are distributed over the full layer system with a thin metallic layer at the surface as well as Ni-Si and Ni-O compounds in the substrate. The results shown here confirm the potential of this non-destructive and non-preparative methodology for interface speciation. Especially the combination of NEXAFS and calibrated instruments makes it possible to consider the mass deposition of the species in absolute values with known uncertainties.

X-ray emission spectrometry

The measurement of the X-ray emission of a sample with high spectral resolution – as made possible by wavelength-dispersive spectrometers – allows the separation of the spectral fractions of the different fluorescence processes involved with regard to their transition energy and to their line intensity. With this method, a quantitative determination of the transition rate is possible, as well as the determination of the chemical shifts of the transition energy. The measurement of transition rates in the soft X-ray range (< 2 keV) with a calibrated grating spectrometer developed by PTB can be used for the traceable determination of FPs for XRF quantification with reduced uncertainties [16]. The observation of the chemical shifts and of the bond-dependent satellite transitions in the emission spectrum of a sample allows the chemical speciation of the compound or the determination of the oxidation state of the respective elements [28].

For the chemical speciation of low mass deposition and of buried nanolayers, the grating spectrometer was extended by X-ray focusing optics in the excitation channel in the form of a single-bounce elliptic monochromator which enhances the sensitivity of the spectrometer by up to a factor of 5. This allows the re-focusing of the undulator radiation below 15 μm on the sample, so that the entrance slit can be dispensed with while maintaining resolving power, which otherwise consid-

erably reduces the intensity of the fluorescence radiation that can be detected by the spectrometer. Figure 8 shows the emission spectra of a metallic Ti layer and of a TiO_2 layer which were recorded with the grating spectrometer and the monochromator. Both layers are 100 nm thick and were deposited onto a Si_3N_4 membrane of 200 nm thickness. Besides the satellite lines, which are characteristic of covalent bonds, one can see a modified intensity ratio of the two L3 diagram lines Ti-L α and Ti-L β for TiO_2 [28]. This is due to the formation of the molecular orbitals whose energetic position and distribution differ from the M4,5 shells (3d) of the metallic titanium. The different intensity ratios of the L fluorescence lines of Ti and TiO_2 confirm that the fundamental parameters may depend on the chemical bond.

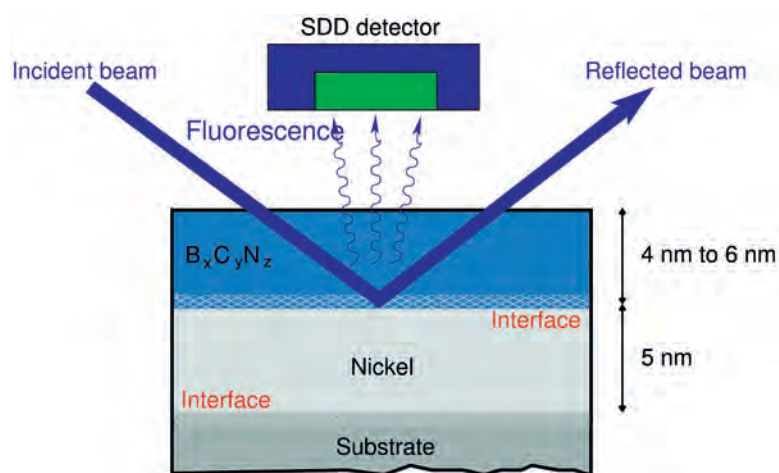


Figure 6: Schematic representation of a GIXRF-NEXAFS experiment on a buried Ni/ $\text{B}_x\text{C}_y\text{N}_z$ interface.

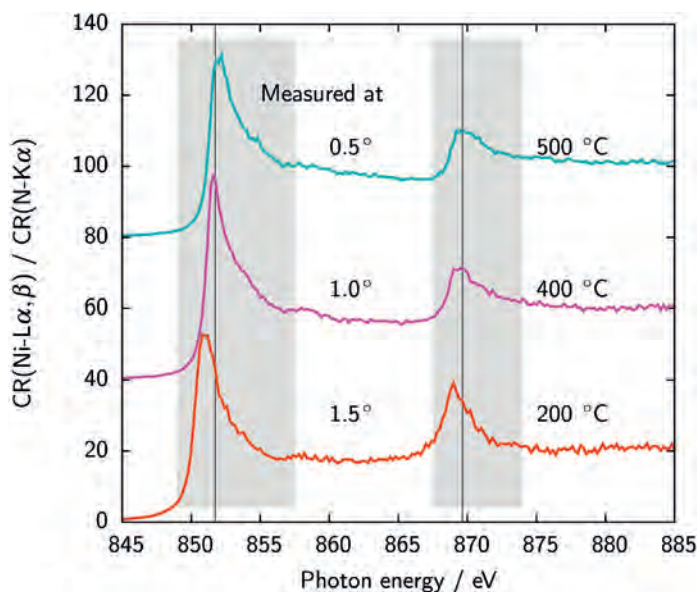


Figure 7: NEXAFS spectra of nickel at the interface (Figure 6) for three samples with different depositing temperatures. The NEXAFS spectrum of the interface was determined from several NEXAFS measurements with different information depths by comparison and difference methodologies.

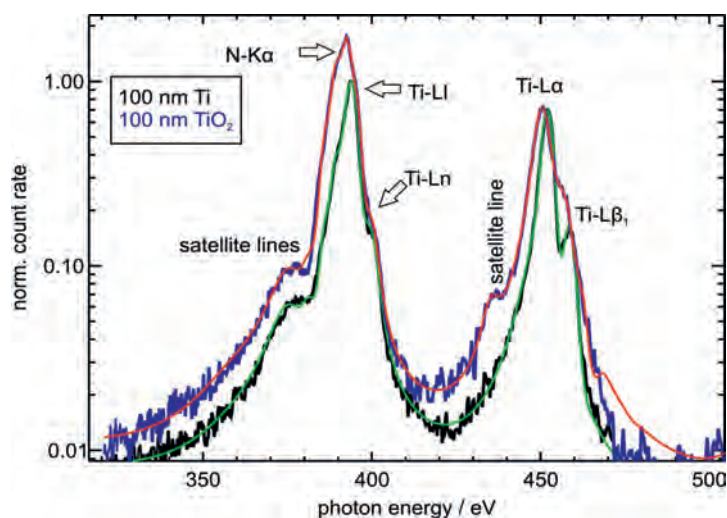


Figure 8: X-ray emission spectra of a metallic Ti layer (black) and of a TiO_2 layer (blue). Both spectra exhibit a different line ratio for L α and L β . The model spectra that were adjusted with the aid of the response function of the grating spectrometer for spectrum deconvolution are shown in green (Ti) and in red (TiO_2).

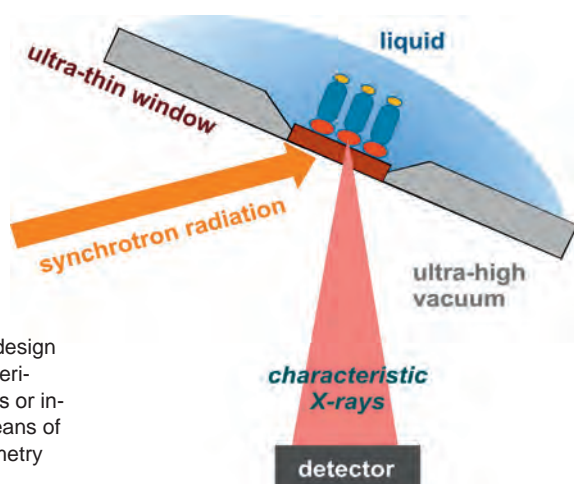


Figure 9: Experimental design for the characterization of liquids or interfaces by means of X-ray spectrometry under vacuum.

Liquid cells and in-situ metrology

The in-situ characterization of solid liquid interfaces is an important field for bio-analytics, medical diagnostics, the characterization of battery materials as well as the fundamental understanding of chemical and electro-chemical processes on surfaces. In soft X-ray spectrometry, special requirements are placed on the test set-up, since the experiments have to be performed under UHV conditions. For this purpose, vacuum-compatible measuring cells are used which have thin windows and are transparent or weakly absorbing for radiation. The liquid or the solid liquid interface located at the inner side of the window can be measured through the ultra-thin windows. Figure 9 shows the typical experimental design for the characterization of such interfaces and liquids under ultra-high vacuum conditions. The material used for these windows is, for example, 150-nm-thin Si_3N_4 and SiC layers.

The chemical characterization of the solid liquid interface is performed by NEXAFS measurements. Organic substances, for example, are investigated as a function of the material selected for the window by means of NEXAFS analysis at the K edges of carbon and nitrogen. Figure 10 shows how concanavalin A, a protein from the jack bean which consists of 237 amino acids, is detected by means of a comparative NEXAFS measurement at the nitrogen K edge. The characteristic of this protein is the resonance of the amide bond at 401.2 eV.

A similar measuring cell is to be developed for the in-situ characterization of Li-S battery materials for a spectrometric investigation of sulphur in porous cathodic layers. At this stage of devel-

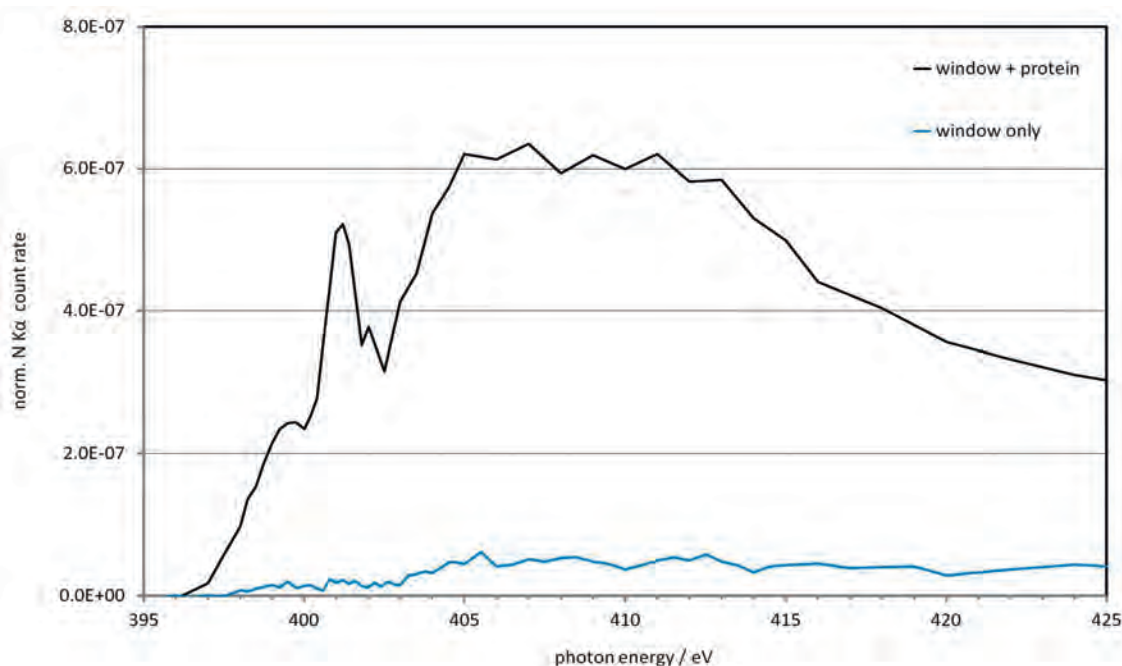


Figure 10: NEXAFS spectrum in the photon energy range from 395 eV to 425 eV of a SiC window as a reference and, for comparison, with a window whose reverse side has been coated with the protein from the jack bean, concanavalin A.

opment, the ex-situ measuring cells can be used to carry out NEXAFS measurements on cathodic material under controlled atmosphere (argon) without exposing the material (which is very reactive to air) to the ambient air after the electro-chemical cyclization [29]. The aim of developing this ex-situ cell further is to allow Li-ion batteries to be characterized *in operando* by means of X-ray spectrometry in order to observe degradation processes in real-time during the charging and discharging cycles.

References

- [1] F. Senf, U. Flechsig, F. Eggenstein, W. Gudat, R. Klein, H. Rabus, G. Ulm: *J. Synchrotron Rad.* **5**, 780 (1998).
- [2] M. Krumrey, G. Ulm: *Nucl. Instrum. Meth. A* **467–468**, 1175 (2001)
- [3] W. Görner, M. P. Hentschel, B. R. Müller, H. Riesemeier, M. Krumrey, G. Ulm, W. Diete, U. Klein, R. Frahm: *Nucl. Instrum. Meth. A* **467–468**, 703 (2001)
- [4] M. Richter, G. Ulm: in this publication on p. 3
- [5] R. Klein, R. Fliegau, S. Kroth, W. Paustian, M. Richter, R. Thornagel: in this publication on p. 16
- [6] F. Scholze, M. Procop: *X-ray Spectrom.* **30**, 69 (2001)
- [7] B. Beckhoff: *J. Anal. At. Spectrom.* **23**, 845 (2008)
- [8] J. Lubeck, B. Beckhoff, R. Fliegau, I. Holfelder, P. Hönicke, M. Müller, B. Pollakowski, F. Reinhardt, J. Weser: *Rev. Sci. Instrum.* **84**, 045106 (2013)
- [9] B. Beckhoff, B. Kanngießer, N. Langhoff, R. Wedell, H. Wolf (Eds.): *Handbook of Practical X-Ray Fluorescence Analysis*, Springer, Berlin, 1st Edition (2006)
- [10] B. Beckhoff, R. Fliegau, M. Kolbe, M. Müller, Jan Weser, G. Ulm: *Anal. Chem.* **79**, 7873 (2007)
- [11] M. Müller, A. Nutsch, R. Altmann, G. Borionetti, T. Holz, C. Mantler, P. Hönicke, M. Kolbe, B. Beckhoff: *Sol. State Phenom.* **187**, 291 (2012)
- [12] M. Müller, P. Hönicke, B. Detlefs, C. Fleischmann: *Materials* **7**, 3147 (2014)
- [13] P. Hönicke, B. Beckhoff, M. Kolbe, D. Giubertoni, J. A. van den Berg, G. Pepponi: *Anal. Bioanal. Chem.* **396**, 2825 (2010)
- [14] G. Zschornack: *Handbook of X-Ray Data*, Springer, Berlin (2007)
- [15] P. Hönicke, M. Kolbe, M. Müller, M. Mantler, M. Krämer, B. Beckhoff: *Phys. Rev. Lett.* **113**, 163001 (2014)
- [16] M. Müller, B. Beckhoff, R. Fliegau, B. Kanngießer: *Phys. Rev. A* **79**, 032503 (2009)
- [17] D. Sokaras, A. G. Kochur, M. Müller, M. Kolbe, B. Beckhoff, M. Mantler, Ch. Zarkadas, M. Andrianis, A. Lagoyannis, A. G. Karydas: *Phys. Rev. A* **83**, 052511 (2011)
- [18] M. Kolbe, P. Hönicke, M. Müller, B. Beckhoff: *Phys. Rev. A* **86**, 042512 (2012)
- [19] D. Windt: *Comput. Phys.* **12**, 360 (1998)
- [20] B. Pollakowski, B. Beckhoff, F. Reinhardt, S. Braun, P. Gawlitza: *Phys. Rev. B* **77**, 235408 (2008)
- [21] P. Hönicke, Y. Kayser, B. Beckhoff, M. Müller, J.-Cl. Dousse, J. Hoszowska, S. H. Nowak: *J. Anal. At. Spectrom.* **27**, 1432 (2012)
- [22] J. F. Ziegler, M. D. Ziegler, J. P. Biersack: *Nucl. Instrum. Methods Phys. Res. B* **268**, 1818 (2010)
- [23] A. M. Gabor, J. R. Tuttle, A. Schwartzlander, A. L. Tennant, M. A. Contreras, R. Noufi: *Sol. Energy Mater. Sol. Cells* **41-2**, 247 (1996)
- [24] T. Dullweber, O. Lundberg, J. Malmström, M. Bodegård, L. Stolt, U. Rau, H. W. Schock, J. H. Werner: *Thin Solid Films* **387**, 11 (2001)
- [25] C. Streeck et al: *Appl. Phys. Lett.* **103**, 113904 (2013)
- [26] C. Streeck, B. Beckhoff, F. Reinhardt, M. Kolbe, B. Kanngießer, C. A. Kaufmann, H. W. Schock: *Nucl. Instrum. Meth. B* **268**, 277 (2010)
- [27] B. Pollakowski, P. Hoffmann, M. Kosinova, O. Baake, V. Trunova, R. Unterumsberger, W. Ensinger, B. Beckhoff: *Anal. Chem.* **85**, 193 (2013)
- [28] F. Reinhardt, B. Beckhoff, H. Eba, B. Kanngießer, M. Kolbe, M. Mizusawa, M. Müller, B. Pollakowski, K. Sakurai, G. Ulm: *Anal. Chem.* **81**, 1770 (2009)
- [29] M. Müller, S. Choudhury, K. Gruber, V. Cruz, B. Fuchsichler, T. Jacob, S. Koller, M. Stamm, L. Ionov, B. Beckhoff: *Spectrochim. Acta B* **94–95**, 22 (2014)

Micro- and Nanospectroscopy and Detector Characterization in the IR and THz Range at the Metrology Light Source

Peter Hermann*, Arne Hoehl, Andrea Hornemann, Bernd Kästner, Ralph Müller, Burkhard Beckhoff, Gerhard Ulm

* Peter Hermann,
Working Group
"IR spectrometry",
e-mail:
peter.hermann@
ptb.de

Introduction

Electron storage rings as synchrotron radiation sources had first been used for the generation of highly brilliant radiation from the vacuum UV to the X-ray spectral range. Due to this high brilliance (or spectral radiance) – which even in the infrared (IR) range is higher by two to three orders of magnitude than that of thermal sources – and the broadband of the synchrotron radiation spectrum, storage rings have, since the beginning of the 1980s, also been used as IR radiation sources [1]. In addition to the high brilliance, the high degree of polarization and the time structure of the synchrotron radiation (SR) with pulse durations in the ps range are also of advantage in the IR range. Today, SR in the IR range is being used at approximately 30 storage rings worldwide [2]. Based on the high brilliance, particularly microspectroscopy with a spatial resolution up to the diffraction limit is performed in the mid infrared (MIR) and in the far infrared (FIR). Many of the applications lie in the field of material sciences, biology or medicine [2–4].

In the course of more than 30 years, PTB has gained experience in the use of SR for metrology at the storage rings BESSY I and II (not, however, in the IR range) [5, 6]. The IR range has been made accessible to PTB only at the *Metrology Light Source* (MLS), where two dedicated beamlines have been installed for the IR and the terahertz (THz) range [6, 7]. Already in the planning phase, the MLS itself has – as the first storage ring worldwide – been optimized to generate coherent radiation in the THz range with radiant powers of up to 60 mW in the special operation mode with particularly short stored electron bunches [8–10].

In the following, selected fields of work at these beamlines will be presented.

FTIR microspectroscopy and secondary structure analysis on biomolecules

In Fourier Transformed Infrared (FTIR) Spectroscopy, a measured interferogram is converted into a spectrum by means of Fourier transformation [11]. At the MLS, bioanalytical investigations with a vacuum FTIR spectrometer (BRUKER Vertex80v), among other things, are performed. The spectral resolution of the Vertex80v amounts to 0.07 cm^{-1} . The attached HYPERION 3000 microscope has been optimized for the MIR range and is equipped with a 128^2 -Pixel-Focal-Plane-Array detector for spatially resolved spectroscopy. With a 15x-Cassegrain objective, a resolution of approx. $3\text{ }\mu\text{m}$ is achieved. The MIR range is particularly well suited to excite valence and deformation vibrations of the molecule groups contained in proteins [12, 13]. These MIR signatures, which are also called molecular fingerprints, allow a distinct identification of biomolecules. In addition, IR radiation is not ionizing and allows a non-destructive chemical analysis of biological samples.

At the MLS, FTIR-spectroscopic investigations can also be carried out in the FIR and in the THz range. Here, molecular information, such as rotational bands of the carbon skeleton and hydrogen bonds which occur, for example, in biomolecules, become accessible, in addition [14]. Although the bands occurring there are less complex compared to the modes in the MIR range and, in addition, thermally broadened, they, too, provide information about the structure of biomolecules.

In the MIR range, the group frequencies which are characteristic of proteins (e.g. specific amide bands) are of particular interest for the secondary structure analysis of biomolecules. Thereby, a distinction can be made between different structure types: the α -helix, whose best-known representative is the deoxyribonucleic acid (DNA), and the β -sheet or the β -loops. If all forms occur

with approximately the same frequency, or if the protein has no recognizable secondary structures, one speaks of a random-coil structure [15]. The cause of these different secondary structure motifs inside a protein is hydrogen bonds and characteristic bond angles between the peptide bonds via which the amino acid sub-units of the primary structure are interlinked.

The amide-I-band, which results from C=O stretching vibrations of the peptide skeleton inside a protein, is particularly suited for secondary structure analyses [16]. Changes to the external parameters (pH value, temperature) and interactions with other biomolecules thus allow investigations of conformational changes⁽¹⁾ that can be detected with high sensitivity with the help of IR spectroscopy [17, 18]. As an example, Figure 1 (a) shows the measured IR signature of a protein – in this case of the bovine serum albumin (BSA) – which exhibits α -helical secondary structure elements. Characteristic of this secondary structure motif is the amide-I-band at 1654 cm^{-1} .

For the structure analysis, different mathematical procedures such as, for example, 2D correlation analysis, are used [19]. This analysis serves to simplify complex data sets of a mostly hyperspectral nature, to unfold overlapping bands, and to increase the spectral resolution by plotting the bands against each other over the second dimension. As an example, Figure 1 (b) shows the 2D correlogram Φ^2 associated with the data in Figure 1 (a).

In the 2D correlation plots, so-called auto-peaks can be seen along a virtual diagonal which illustrate the spectral range of the highest absorption changes caused by temperature influence on the sample system. In contrast to this, values close to zero indicate a low spectral temperature dependence. Peaks outside the diagonal represent simultaneous changes in the absorption which are observed at two different wavenumbers ν_1 and ν_2 and, thus, suggest the same origin of the change.

At the MLS, SR-based FTIR spectroscopy is used for the fundamental structure analysis on peptides within the scope of a project⁽³⁾ of the European Metrology Research Programme (EMRP) from the MIR up to the THz spectral range. Amino acids, and the peptides based on them, open up new diagnostic possibilities, for example in cancer research. Furthermore, if the properties of the active substances of peptides, which are based on molecular interaction mechanisms, are exactly known, drugs can be developed which allow illnesses to be treated more effectively. The project deals with the investigation of secondary structure motifs of model peptides which may exert different interaction mechanisms with artificial membrane systems (here: liposomes). It is the main objective of this research project to intro-

duce all results obtained from diverse bioanalytical methods for molecular-dynamic simulations in order to validate the properties of the active substances of peptides.

Another EMRP project is aimed at characterizing biomedical products (stent systems, implants) under process-analytical aspects. The determination of the elementary composition of implant materials as well as the detection of surface contaminations are further aspects of the project. In addition, a method validation based on investigations on model systems and on real-material systems is being aimed at.

Infrared near-field microscopy and nano-FTIR-spectroscopy

The achievable spatial resolution of conventional optical methods is limited by diffraction so that structures smaller than half the wavelength of the incident light can no longer be resolved. In the case of near-field microscopy, the resolution limit given by the wave nature of light is avoided by also using the so-called evanescent waves – and not only the propagating waves – close to the sample surface. These waves also contain information about surface structures which may be clearly smaller than the wavelength of the incident radiation. This makes optical investigations with a spatial resolution at the nanoscale possible.

Scattering-near-field optical microscopes [20, 21] are mostly based on the functional principle of scanning force microscopy, by which spatially resolved optical information is

1 This relates to the change in the spatial structure of a protein.

2 The amplitude Φ is calculated via

$$\Phi(\nu_1, \nu_2) = \frac{1}{m-1} \sum_{j=1}^m A_j(\nu_1) A_j(\nu_2),$$

with $A_j(\nu_k)$ being the spectral absorption related to the absorption averaged over the temperature, for m spectra in a specific temperature interval.

3 <http://projects.npl.co.uk/HLT10-BiOrigin/> (retrieved: 2015-07-07)

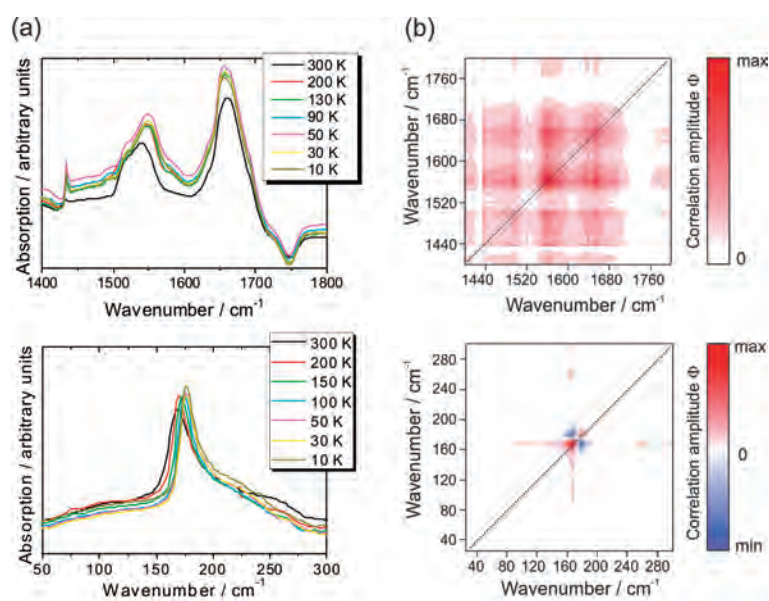


Figure 1: (a) Signatures of BSA in the MIR (top) and FIR (bottom). (b) 2D correlation diagrams $\Phi(\nu_1, \nu_2)$, showing the temperature dependence of the bands in the amide I (top) and amide VII ranges (bottom).

gained due to the interaction of the probe with the electromagnetic near field of the sample. For this purpose, a near-field probe is brought into a focused light beam, and the light scattered on it is detected. The achievable spatial resolution is determined mainly by the tip radius of the near-field probe used which is typically below 50 nm and, thus, clearly below the optical diffraction limit. In addition to the spatial resolution, the detection sensitivity can be increased so that both weakly absorbing materials and samples with a tiny scattering volume can still be investigated [21]. By lateral probing of the sample one now obtains – in addition to the topographic image – also informa-

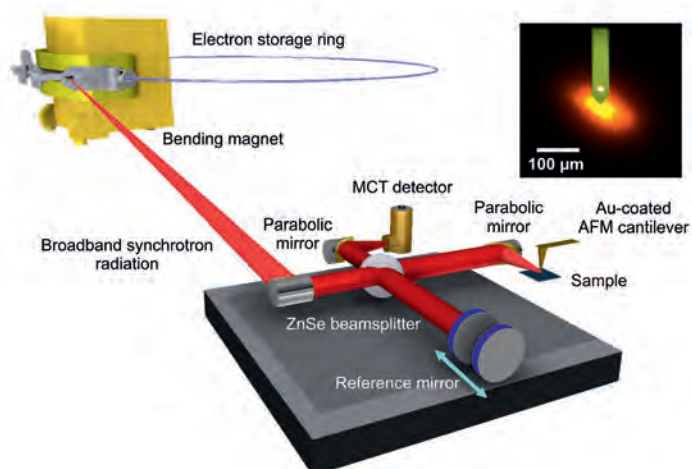


Figure 2: Schematic representation of the scattered light near-field microscope at the MLS using broadband SR of a bending magnet of the MLS. The radiation is directed via several mirrors (not shown here) to the near-field microscope and focused onto the AFM cantilever. The focused IR beam has a diameter of approx. 80 μm (see microscope image top right). The signal scattered on the tip is detected by an IR-sensitive detector (MCT = mercury cadmium telluride).

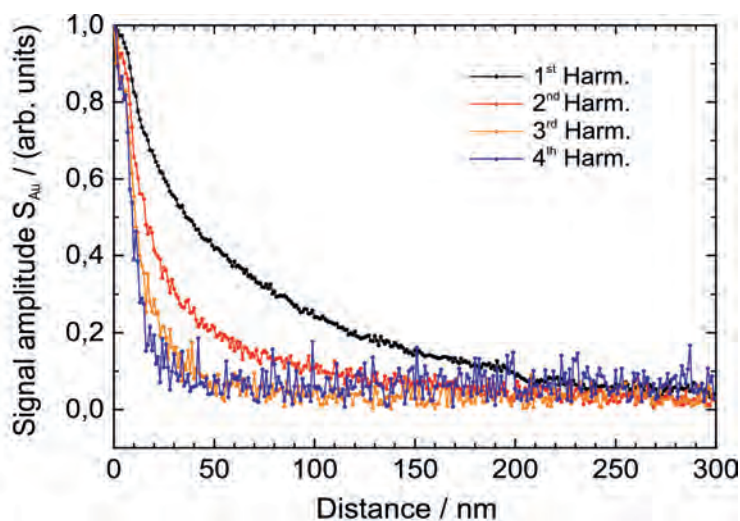


Figure 3: Decrease in the signal amplitude as a function of the distance between the tip and the sample surface. The scattered signal is demodulated at the higher harmonics of the oscillation frequency of the cantilever to separate the intensive far-field signal from the weak near-field contribution. In the case of a high near-field fraction, the signal decays within less than 50 nm.

tion about the optical properties of the surface with precisely this improved spatial resolution in the nanometer range.

As a rule, monochromatic IR light sources – in most cases lasers (e.g. tunable CO or CO₂ gas lasers) – are used for near-field microscopy in order to image the optical properties of a sample surface at a fixed wavelength. In most cases, commercially available Au- or Pt-coated Si cantilevers are used as near-field probes which are excited to oscillations in the frequency range of a few hundred kHz vertically to the sample surface. To separate the intensive far-field signal from the relatively weak near-field contribution, the near-field signal is detected by demodulation of the signal in the higher harmonics of the cantilever's oscillation frequency. Thereby, the strongly exponential decay of the near-field signal, compared to the comparatively constant far-field signal, is exploited.

In 2012, PTB started to establish, in cooperation with the *Freie Universität Berlin* (Working Group of Prof. E. Rühl), a commercially available scattering-type scanning near-field optical microscope at the IR beamline of the MLS (Figure 2). The fundamental aim was to utilize the high brilliance and the defined polarization of the broadband IR SR for performing nano-FTIR spectroscopy in an extended spectral range.

As early as in September 2012 it could be clearly demonstrated worldwide for the first time that a spatial resolution below 100 nm can also be achieved with broadband SR and that nano-FTIR spectroscopy is possible. Figure 3 shows the exponential decrease in the signal amplitude at the higher harmonics of the cantilever's oscillation frequency which is typical of the near-field signal detection. Whereas in the case of the 1st harmonic, the signal decays to the noise level only at a distance of about 200 nm between the tip and the sample surface, the signal amplitude of the 2nd, 3rd and 4th harmonic strongly decreases already after approx. 50 nm.

As a first step towards nano-FTIR spectroscopy, several near-field scans were carried out on an Au layer or across an Au/SiC edge (as summarized in Figure 4). Slight contaminations on the Au surface (diameter: less than 100 nm) can be clearly seen in both the topography image and in the simultaneously recorded optical image. During the scanning across the Au/SiC edge, the optical signal changes within less than 100 nm [22]. By a further optimization of the set-up, a spatial resolution of less than 40 nm has meanwhile been achieved [23].

In a second step, the device was equipped with the Michelson interferometer shown in Figure 2 for the recording of near-field spectra. The reference arm contains a movable mirror to detect the intensity change as a function of the optical path

length difference. The second arm of the interferometer contains the near-field probe and the sample. In the resulting nano-FTIR-spectrum – recorded, for example, of a SiC surface – the characteristic phonon resonance appears at approx. 920 cm^{-1} (Figure 5). As this pronounced phonon resonance can be seen only in near-field spectra, the observation is regarded as a clear demonstration of successful nano-FTIR- spectroscopy. Figure 5 shows the interferograms (5a) and the corresponding nano-FTIR spectra (5b) recorded from differently thin layers [23].

In principle, the use of broadband SR allows the characterization of thin layers and nanostructures in a broad wavenumber range from 700 cm^{-1} to 3400 cm^{-1} by near-field spectroscopy. Possible applications of near-field microscopy and nano-FTIR-spectroscopy are currently investigated within the scope of EMRP projects. For example, within the scope of the EMRP Nanostrain project, SR-based nano-FTIR spectroscopy is evaluated for the characterization of the intrinsic strain in semiconductor and piezoelectric nanostructures⁽⁴⁾.

Characterization of radiation detectors by ultra-short pulses of coherent synchrotron radiation

In a special operation mode, the MLS can be used to generate coherent SR (CSR) in the range of THz radiation, whereby the pulse lengths of the radiation pulses lie in the range from 10 ps to the sub-picosecond range. In the case of this special operation mode, the THz spectrum covers a useful wavenumber range from 1.4 cm^{-1} to 50 cm^{-1} (corresponding to a wavelength of 7 mm to $200\text{ }\mu\text{m}$). The ratio of the intensities from coherent to incoherent SR amounts to 10^5 at maximum, while the stability amounts to up to 0.3 % [7]. The CSR can be optimally used on the dedicated THz beamline which has been designed for the wavelength range from $100\text{ }\mu\text{m}$ to 7 mm.

CSR is used in the following projects: Transmission spectroscopy of peptide films on an FTIR spectrometer, lifetime measurement of excitations of different dopant atoms on a THz pump-probe arrangement of the *Deutsches Zentrum für Luft- und Raumfahrt* (DLR, German Aerospace Center) [24], as well as characterization of the spectral sensitivity and temporal resolution of radiation detectors on a detector testing set-up. The latter allows us to perform investigations such as linearity measurements, determination of the polarization dependence as well as measurements of the time-dependent response of novel THz detectors [25]. As possible detectors for the time-dependent characterization of CSR-THz pulses, superconducting bolometers or Schottky diodes come into consideration. With an YBCO-

based bolometer, CSR-THz pulses with a temporal resolution of better than 20 ps could be demonstrated on this set-up [25]. YBCO detectors have, however, the disadvantage that they must

4 <http://www.piezoinstitute.com/resources/emrp-nanostrain/> (retrieved: 2015-07-07)

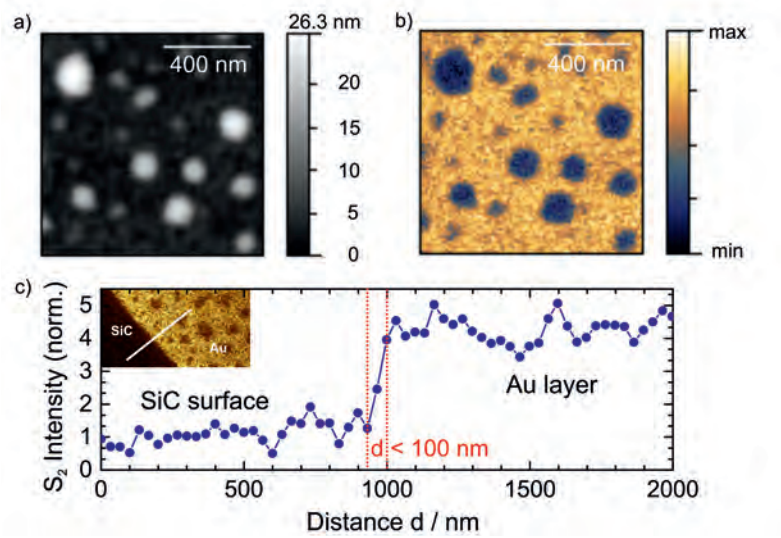


Figure 4:

Topography (a) and simultaneously recorded optical image (b) of an Au surface. Due to the different optical properties, the contaminations appear on the Au surface as dark areas. A scan performed across a SiC/Au edge shows that a spatial resolution d of clearly below 100 nm can be achieved (c).

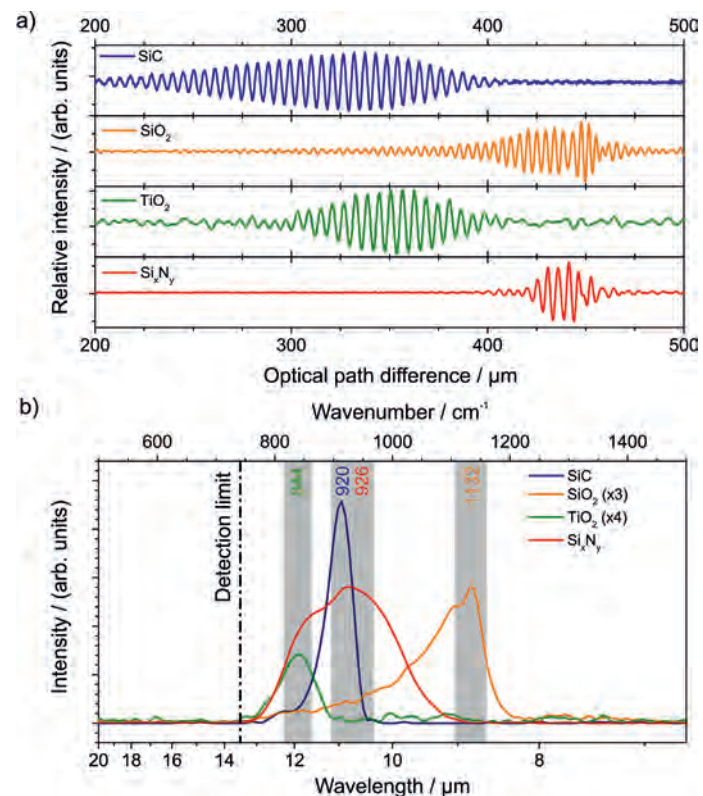


Figure 5:

Interferograms, recorded from different layers: "solid" 6H-SiC, SiO_2 (30 nm in thickness), 10 nm TiO_2 (anatase) and 50 nm Si_3N_4 . The associated nano-FTIR- spectra are obtained by subsequent Fourier transformation (b). For better comparability, the spectra of SiO_2 and TiO_2 have been scaled. The numbers in the color of the respective curve indicate the wavenumbers (in cm^{-1}) of the respective peak intensities [23].

5 ZIM (*Zentrales Innovationsprogramm Mittelstand*) is a promotion program of the Federal Ministry of Economics and Energy for SMEs.

be cooled with liquid nitrogen and are, therefore, usually installed in a larger dewar. Here, Schottky diodes offer a possible alternative, as they work under room temperature conditions and are characterized by a compact design [26]. Within the scope of a ZIM project⁽⁵⁾ for the *development of an ultra-broadband compact detector for the characterization of THz synchrotron radiation*, these Schottky detectors are currently being investigated. The objective is to improve the response time and to increase the spectral bandwidth. The Schottky diode detector is intended to combine the advantages of planar diode technology with the broadband coupling efficiency of planar antennas. This allows the dimensions of the interface surface between the diode and the antenna to be reduced and, thus, the upper frequency limit of the detection band to be extended. It is expected that these detectors will cover a frequency range from 0.01 THz to 5 THz and have a response time of less than 25 ps [26]. In addition to the THz storage ring diagnostics, further possible applications lie in the field of ultrafast spectroscopy.

References

- [1] G. P. Williams: Nucl. Instruments Methods Phys. Res. **195**, 383 (1982)
- [2] M. C. Martin, U. Schade, P. Lerch, P. Dumas: Trends Anal. Chem. **29**, 453 (2010)
- [3] M. C. Martin, P. Dumas: Spectrosc. Prop. Inorg. Organomet. Compd. **43**, 141 (2012)
- [4] P. Dumas, L. M. Miller, M. J. Tobin: Acta Phys. Pol. A **115**, 446 (2009)
- [5] B. Beckhoff, A. Gottwald, R. Klein, M. Krumrey, R. Müller, M. Richter, F. Scholze, R. Thornagel, G. Ulm: Phys. Status Solidi B **246**, 1415 (2009)
- [6] M. Richter, G. Ulm: in this publication on p. 3
- [7] R. Müller, A. Hoehl, A. Matschulat, A. Serdyukov, G. Ulm, J. Feikes, M. Ries, G. Wüstefeld: J. Phys. Conf. Ser. **359**, 012004 (2012)
- [8] R. Müller, A. Hoehl, R. Klein, A. Serdyukov, G. Ulm, J. Feikes, M. von Hartrott, G. Wüstefeld: PTB-Mitteilungen **120**, 229 (2010)
- [9] R. Müller, A. Hoehl, A. Serdyukov, G. Ulm, J. Feikes, M. Ries, G. Wüstefeld: J. Infrared Milli. Terahz. Waves **32**, 742 (2011)
- [10] J. Feikes, M. von Hartrott, M. Ries, P. Schmid, G. Wüstefeld, A. Hoehl, R. Klein, R. Müller, G. Ulm: Phys. Rev. ST Accel. Beams **14**, 030705 (2011)
- [11] P. R. Griffiths, J. A. de Haseth: Fourier Transform Infrared Spectrometry, Wiley, New York (2007)
- [12] E. B. Wilson, J. C. Decius, P. C. Cross: Molecular Vibrations: The Theory of Infrared and Raman Vibrational Spectra, vol. 102, Dover Publications, New York (1955)
- [13] N. B. Colthup, L. H. Daly, S. E. Wiberley: Introduction to Infrared and Raman Spectroscopy, Academic Press, New York (1990)
- [14] Y. Marechal: J. Mol. Struct. **880**, 38 (2008)
- [15] M. Levitt: Biochemistry **17**, 4277 (1978)
- [16] H. Fabian, C. Schultz, J. Backmann, U. Hahn, W. Saenger, H. M. Mantsch, D. Naumann: Biochemistry **33**, 10725 (1994)
- [17] K. Kato, T. Matsui, S. Tanaka: Appl. Spectrosc. **41**, 861 (1987)
- [18] B. Yuan, K. Murayama, Y. Wu, R. Tsenkova, X. Dou, S. Era, Y. Ozaki: Appl. Spectrosc. **57**, 1223 (2003)
- [19] I. Noda and Y. Ozaki: Two-dimensional Correlation Spectroscopy – Application in Vibrational and Optical Spectroscopy, John Wiley & Sons, Chichester, West Sussex (2004)
- [20] A. Zayats, D. Richards (Eds.): Nano-Optics and Near-Field Optical Microscopy. Artech House, Boston (2008)
- [21] L. Novotny, B. Hecht: Principles of Nano-Optics, Cambridge University Press, Cambridge (2006)
- [22] P. Hermann, A. Hoehl, P. Patoka, F. Huth, E. Rühl, G. Ulm: Opt. Express **21**, 2913 (2013)
- [23] P. Hermann, A. Hoehl, G. Ulrich, C. Fleischmann, A. Hermelink, B. Kästner, P. Patoka, A. Hornemann, B. Beckhoff, E. Rühl, G. Ulm: Opt. Express **22**, 17948 (2014)
- [24] A. Pohl, A. Hoehl, R. Müller, G. Ulm, M. Ries, G. Wüstefeld, S. G. Pavlov, H.-W. Hübers: Terahertz pump-probe experiment at the synchrotron light source MLS, Extended Abstracts of IRMMW-THz 2013, TU5-4, Mainz, 1–6 (2013)
- [25] P. Probst, A. Scheuring, M. Hofherr, D. Rall, S. Wünsch, K. Il'in, M. Siegel, A. Semenov, A. Pohl, H.-W. Hübers, V. Judin, A.-S. Müller, A. Hoehl, R. Müller, G. Ulm: Appl. Phys. Lett. **98**, 043504 (2011)
- [26] N. Sobornyt'skyy, A. Lisauskas, C. Weickmann, R. Jakobi, A. Semenov, H. Hübers, R. Müller, A. Hoehl, O. Cojocari: Quasi optical Schottky diode detectors for fast ultra-wideband detection, Extended Abstracts of IRMMW-THz 2013, TU8-5, Mainz, 1–6 (2013)

Surface Characterization with Vacuum UV Radiation

Michael Kolbe*, Erik Darlatt, Rolf Fliegauf, Hendrik Kaser,
Alexander Gottwald, Mathias Richter

Introduction

In numerous areas, new materials are the key to technological developments. Hereby, the quantification of relevant material parameters – such as the electronic, chemical and morphologic structure and elementary composition – plays a central role. In this context, the lack of suitable reference samples for quantitative analytical procedures often makes metrological traceability indispensable. Therefore, with the commissioning of PTB's laboratory at BESSY II in 1999 and of the MLS in 2008, various areas of materials metrology with synchrotron radiation were taken up apart from radiometry but based on radiometry [1–5]; these topics have allowed PTB to contribute considerably to activities within the scope of the European Metrology Research Programme (EMRP). This applies to X-ray spectrometry and reference-free X-ray fluorescence analysis [6], nanometrology (i.e. the traceable determination of particle sizes [7]), surface texture [8] and layer thickness [5] in the nanometer range by means of small-angle X-ray scattering and X-ray reflectometry, micro- and nanospectroscopy in the infrared and the THz range [9] as well as surface investigations with synchrotron radiation in the spectral range of vacuum UV (VUV). To this end, the first results obtained with ellipsometry in this spectral range will be presented in the following; these were obtained within the scope of a contractual cooperation project with the *Leibniz Institute for Analytical Sciences* (ISAS, Group of Prof. N. Esser). Furthermore, results in photoelectron spectroscopy will be presented.

Ellipsometry

Spectroscopic ellipsometry is an extension of reflectometry [5] and represents a widespread optical method to analyze surfaces. It is based on the change in the polarization state of the radiation in the case of reflection on surfaces and enables the traceable determination of optical constants and of the linear dielectric response function of the material investigated as well as of further parameters such as, e.g., the layer thickness or the elemental composition of structured samples [10, 11]. Ellipsometry is a non-destructive method and is suitable both for fundamental and for application-oriented issues. Combined with conventional laboratory light sources in commercial devices, spectroscopic ellipsometry is used over a broad spectral range – from the far infrared up to ultraviolet radiation – for example in process monitoring and process control. In the VUV spectral range, ellipsometry can be used for more advanced issues, since materials can, in principle, also be excited in the energy range of the band gap and above. This, however, requires more effort. Firstly, sufficiently intense and polarized VUV radiation is necessary. Secondly, all components must be placed in an ultra-high vacuum (UHV) environment, both to prevent undesired absorption of the VUV radiation under ambient conditions and to keep the sample surfaces, which are in some cases specially prepared, free of contamination as ellipsometry is a surface-sensitive method.

The first ellipsometer for synchrotron radiation was developed in the late 1980s [12]. It could be used in the photon energy range above 6 eV, which is not covered by laboratory devices. Based on this, the ISAS developed a new ellipsometer in the past few years, which has been operated within the scope of a research cooperation with PTB at the insertion device beamline (IDB) of the MLS

* Dr. Michael Kolbe,
Working Group "UV
and VUV Radiome-
try", e-mail: michael.
kolbe@ptb.de

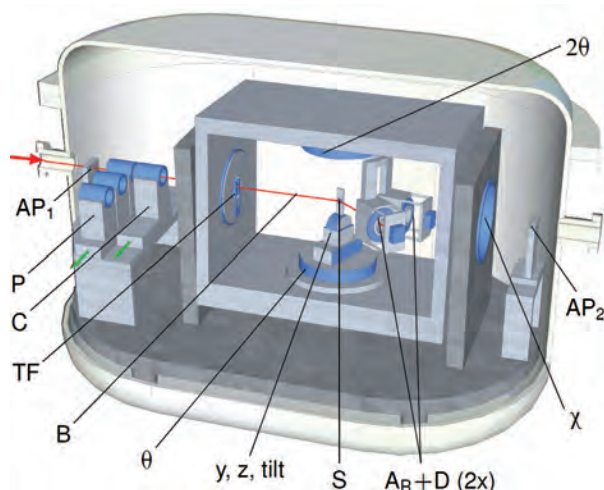


Figure 1:
Scheme of the UHV-compatible ellipsometer at the undulator beamline (IDB) of the MLS [1, 13] (AP_{1,2}: aperture at radiation entry/exit; P: polarizer; C: compensator; TF: chopper; B: beam path; Φ : angle of incidence onto the sample surface; y, z, tilt: goniometer axes for sample adjustment; S: sample; A_R+D: rotating analyzer and detector; χ : rotation axis around the incident beam).

since 2012 [1, 13]. This unique device allows the change in the polarization degree at the reflection on a sample to be determined not only in a fixed geometry, but also at variable incidence and detection angles. Figure 1 shows a scheme of ISAS' new ellipsometer.

At the IDB of the MLS, in the storage ring's plane, highly linear polarized undulator radiation is available for VUV ellipsometry; due to scattering, its polarization degree is, however, attenuated at the optical components. In a first investigation, the polarization degree was therefore determined

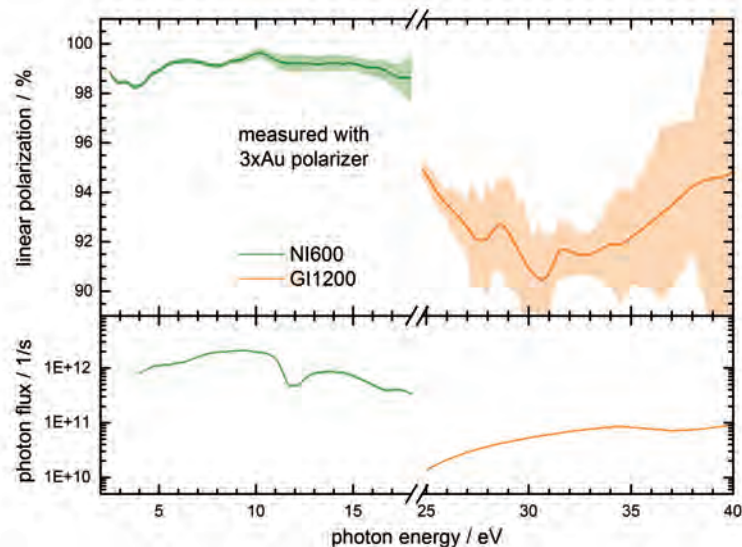


Figure 2:
Linear polarization degree and photon flux at the undulator beamline (IDB) of the MLS for typical measurement conditions and two monochromator grating configurations (NI600 and GI1200).

by means of the VUV ellipsometer [13]. Figure 2 shows the result obtained for the photon energy range between 3 eV and 40 eV. Between 18 eV and 20 eV, the optical configuration of the monochromator is changed from a grating with 600 lines per millimeter working in normal incidence (NI) configuration to a grating with 1200 lines per millimeter in grazing incidence (GI) configuration. Whereas in the NI range, the linear polarization degree is higher than 98 %, it decreases by a few percent in the GI range, e.g. due to depolarized scattering at the grating's surface. All in all, the linear polarization degree of the beamline is, however, very high and ideal for ellipsometry.

First examples for the utilization of the ellipsometer refer to the characterization of epitaxially grown ZnO [13] and of thin-film energy materials within the scope of a European Metrology Research Project carried out together with the BAM Federal Institute for Materials Research and Testing [14]. Hereby, transparent and electrically conductive oxides (TCOs) as well as organic thin-film samples are investigated. The spectral range available at the IDB ranges from the VUV up to visible light and even to the near infrared; it therefore allows spectral overlap to results from measurements performed with commercially available devices under atmospheric pressure. Traceable measurements of dielectric functions and optical constants are envisaged for a series of technologically relevant optical standard materials and layer systems such as, e.g., SiC or SiO₂/Si for which experiments have shown that the corresponding values provided by literature [15] are inconsistent.

Photoelectron spectroscopy

Photoelectron spectroscopy (PES) is a widespread method in the field of materials research with synchrotron radiation, especially to characterize the surface of solids. It allows both the electronic structure of a sample to be investigated and analytical issues to be solved. PES is based on the photoelectric effect where the absorption of a photon with an energy $h\nu$ leads to the emission of an electron whose kinetic energy KE is yielded from the Einstein relation [16]:

$$KE = h\nu - (BE + \Phi).$$

If the work function Φ is known, then the binding energy BE of the electron can be determined.

Depending on the energy of the exciting photons, two main branches of PES can be distinguished which supply diversified information: in the case of ultraviolet photoelectron spectroscopy (UPS), photons in the spectral range from approx. 5 eV up to approx. 70 eV are used for excitation to eject electrons from the outer, energetically lowest (valence) states. This method therefore provides

information on the distribution of the binding energy of the valence electrons. When additionally measuring the angular distribution of the photoelectrons emitted, the valence states as well as the band structure can be determined [17].

Contrary to that, in the case of X-ray photoelectron spectroscopy (XPS), electrons are ejected from the inner shells of the atoms by means of higher-energy photons. The energy of these core levels is characteristic of each type of atom, so that it is possible to determine the elemental composition of a sample. Since core levels slightly shift due to the chemical structure of the sample, XPS additionally provides information about chemical properties of probed atoms.

The apparatus used at the IDB is a SCIENTA electron analyzer R4000 with complex electron pre-optics and a spatially resolving detector. In various operating modes, this spectrometer allows the simultaneous acceptance of both a large solid angle at a fixed electron energy and of an energy band at a fixed emission angle.

Figure 3 shows XPS spectra of an oxidized silicon surface in the spectral range of the Si-2*p* shell level which were recorded at the MLS, exciting with two different photon energies (280 eV, 130 eV). By setting the photon energy appropriately, the escape depth of the photoelectrons can be modified and, thus, a variation of the information depth of an XPS measurement is possible. The structures at a binding energy in the range of 100 eV result from the silicon substrate in the bulk of the sample and can, at approx. 104 eV, be easily distinguished from those of the outer SiO₂ layer. In the intermediate spectral range, Si-2*p* photoemissions of further suboxides at the interface layer can be seen. Traceable quantification of these different fractions plays a role, for example, in the characterization of the surface of silicon spheres which are to serve to redefine the unit *kilogram* by determining the Avogadro constant [5, 18, 19].

Figure 4 shows the result of UPS measurements on three organic thin films consisting of different transition metal/phthalocyanine complexes which were deposited under vacuum onto a titanium substrate. Such material systems are relevant for applications in organic solar cells (OSCs) and in organic light-emitting diodes (OLEDs). The spectra allow the determination of the energetic position of occupied valence states as well as conclusions about light-converting and light-emitting processes in OSCs and OLEDs, respectively, to be drawn [20]. On similar systems, already the influence of C₆₀ doping on the electronic structure and on the electro-optical properties has been investigated [21] as well as ageing effects due to quantitative UV irradiations [22].

By continuing these activities which have begun only recently, the objective is to establish photo-

electron spectroscopy as a complementary method to ellipsometry and X-ray spectrometry with synchrotron radiation [6] as a traceable method for the investigation of technologically relevant surface and layer systems and to implement it in cooperation with external partners within the scope of third-party-funded projects such as the EMRP project *ThinErgy* [14].

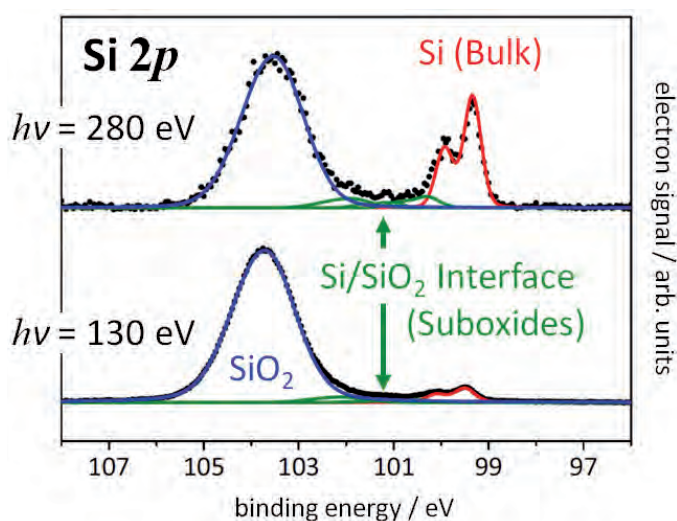


Figure 3: XPS spectra of a silicon oxide layer on silicon, recorded at different photon energies of the exciting radiation (280 eV, 130 eV) [18].

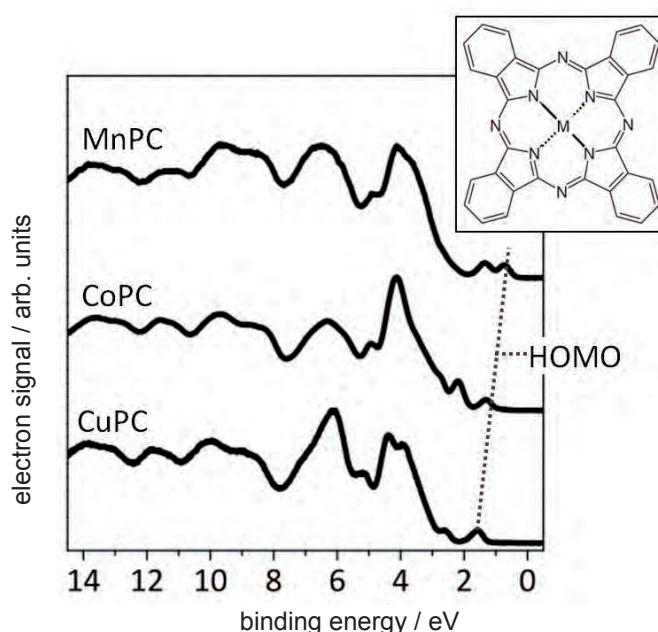


Figure 4: UPS spectra of 7 nm thick Mn(II), Co(II) and Cu(II) phthalocyanine thin films on Ti ($h\nu = 60$ eV).

References

- [1] *M. Richter, G. Ulm*: in this publication on p. 3
- [2] *R. Klein, R. Thornagel, G. Ulm*: in this publication on p. 7
- [3] *R. Klein, R. Fliegau, S. Kroth, W. Paustian, M. Richter, R. Thornagel*: in this publication on p. 16
- [4] *A. Gottwald, U. Kroth, M. Krumrey, P. Müller, F. Scholze*: in this publication on p. 21
- [5] *M. Krumrey, L. Cibik, A. Fischer, A. Gottwald, U. Kroth, F. Scholze*: in this publication on p. 35
- [6] *M. Müller et al.*: in this publication on p. 57
- [7] *M. Krumrey, R. Garcia-Diez, C. Gollwitzer, S. Langner*: in this publication on p. 53
- [8] *F. Scholze, A. Haase, M. Krumrey, V. Soltwisch, J. Wernecke*: in this publication on p. 48
- [9] *P. Hermann, A. Hoehl, A. Hornemann, B. Kästner, R. Müller, B. Beckhoff, G. Ulm*: in this publication on p. 64
- [10] *D. E. Aspnes*: Spectroscopic ellipsometry, in: *Optical Properties of Solids: New Developments*, B. O. Seraphin, (Eds.), North-Holland Publishing, Amsterdam (1976), pp. 799–846
- [11] *M. Schubert*: *Annalen der Physik* **518**, 480 (2006)
- [12] *R. L. Johnson, J. Barth, M. Cardona, D. Fuchs, A. M. Bradshaw*: *Rev. Sci. Instrum.* **60**, 2209 (1989)
- [13] *M. D. Neumann, C. Cobet, H. Kaser, M. Kolbe, A. Gottwald, M. Richter, N. Esser*: *Rev. Sci. Instrum.* **85**, 055117 (2014)
- [14] <http://www.ptb.de/emrp/thinergy.html> (retrieved: 2016-06-30)
- [15] *E. D. Palik* (Eds.): *Handbook of Optical Constants of Solids*, Academic Press, Orlando (1985)
- [16] *A. Einstein*: *Annalen der Physik* **322**, 132 (1905)
- [17] *S. Weiß et al.*: *Nat. Commun.* **6**, 8287 (2015)
- [18] *E. Darlatt, M. Kolbe, R. Fliegau, P. Hönicke, I. Holfelder*: EMRS-Spring Meeting, Lille (France), May 26 to 30 (2014)
- [19] *B. Andreas et al.*: *Phys. Rev. Lett.* **106**, 030801 (2011)
- [20] *N. R. Armstrong, W. Wang, D. M. Alloway, D. Placencia, E. Ratcliff, M. Brumbach*: *Macromol. Rapid Commun.* **30**, 717 (2009)
- [21] *F. Roth, C. Lupulescu, T. Arion, E. Darlatt, A. Gottwald, W. Eberhardt*: *J. Appl. Phys.* **115**, 033705 (2014)
- [22] *E. Darlatt et al.*: *Nanotechnology* **27**, 324005 (2016)

Imprint

The PTB-Mitteilungen are the metrological specialist journal and the official information bulletin of the Physikalisch-Technische Bundesanstalt. As a specialist journal the PTB-Mitteilungen publish original scientific contributions and general articles on metrological subjects from the areas of activities of the PTB. The individual volumes are focused on one subject. The Mitteilungen have a long tradition dating back to the beginnings of the Physikalisch-Technische Reichsanstalt (founded in 1887).

Editor

Physikalisch-Technische Bundesanstalt (PTB),
Braunschweig and Berlin
Postal address:
Postfach 33 45,
38023 Braunschweig
Delivery address:
Bundesallee 100,
38116 Braunschweig

Editorial Staff/Layout

Press and Information Office, PTB
Sabine Siems
Dr. Dr. Jens Simon
(Editor in Chief)
Dr. Mathias Richter
(Scientific Editor)
Phone: +49 531 592-82 02
Fax: +49 531 592-30 08
E-mail: sabine.siems@ptb.de

Translation

PTB-Sprachendienst (PTB Translation Office):
Undine Baier-Blott,
Cécile Charvieux,
Gabriele Froetel,
Alice Graumann,
Ella Jones,
Kathleen Spalinger

All rights reserved. No part of this journal may be reproduced or distributed without the written permission of the publisher. Under this prohibition, in particular, comes the commercial reproduction by copying, the entering into electronic databases and the reproduction on CD-ROM and all other electronic media.

Printed in Germany ISSN 0030-834X

The technical articles from this issue of the PTB-Mitteilungen are also available online at:

**doi: 10.7795/310.20140399en and
doi: 10.7795/310.20140499en**



Bundesministerium
für Wirtschaft
und Energie

The Physikalisch-Technische Bundesanstalt, Germany's national metrology institute, is a scientific and technical higher federal authority falling within the competence of the Federal Ministry for Economic Affairs and Energy.



The Physikalisch-Technische Bundesanstalt, Germany's national metrology institute, is a scientific and technical higher federal authority falling within the competence of the Federal Ministry for Economic Affairs and Energy.



**Physikalisch-Technische Bundesanstalt
Braunschweig and Berlin**
National Metrology Institute

Bundesallee 100
38116 Braunschweig, Germany

Press and Information Office

Phone: +49 531 592-3006

Fax: +49 531 592-3008

E-mail: press@ptb.de

www.ptb.de